Multi-Scale Traction Dynamics in Obliquely Impacted Polymer-Metal Targets

Peter Anthony Sable
Marquette University

MULTI-SCALE TRACTION DYNAMICS IN OBLIQUELY IMPACTED POLYMER-METAL TARGETS

by

Peter Anthony Sable, M.S., E.I.T.

A Dissertation submitted to the Faculty of the Graduate School,
Marquette University,
in Partial Fulfillment of the Requirements for
the Degree of Doctor of Philosophy

Milwaukee, Wisconsin

May 2019

ABSTRACT
MULTI-SCALE TRACTION DYNAMICS
IN OBLIQUELY IMPACTED POLYMER-METAL TARGETS

Peter Anthony Sable, M.S., E.I.T.

Marquette University, 2019

The characterization of polymer behavior at high strain-rates is a critical area of research driven by their use as adhesives, structural components, or even as binders for energetic systems. Current experimentation has been limited to either low strain-rate mechanical testing or plane strain (uniaxial) impact testing. As such, more complicated loading conditions at high strain-rate have remained unexplored. Particularly of interest include the rate dependencies of polymer strength as well as interface traction behaviors like adhesion and dynamic friction phenomena. To investigate these characteristics, fully dense, high durometer, polyurethane (PUR) and epoxy were subjected to combined pressure-shear loading via oblique impact experiments. Two distinct configurations of oblique impact experiments were used to investigate both shear strength and friction behaviors.

Oblique impact resulted in high strain-rate ($10^5 s^{-1}$) combined normal (pressure) and shear stress loading of polymers with magnitudes of approximately 800 (pressure) and 120 MPa (shear) respectively, depending on impact velocity and angle. Material response was inferred from free-surface particle velocities measured using transverse photon Doppler velocimetry techniques. The impact of a 7075-T6 aluminum projectile onto a target consisting of a thin polymer specimen confined between two anvils of the same aluminum allowed for the measurement of polymer shear strengths. Strength was found to increase with higher confining normal stress, increasing strength by almost an order of magnitude. This normal stress (or pressure) dependence was observed to have a greater effect on strengthening than that of strain-rate alone. The oblique impact of a polymer projectile against a 7075-T6 aluminum target provided both a quantification for coefficient of friction, μ and additional material strength information. Polyurethane and epoxy were found to have μ values of approximately 0.11 and 0.26 respectively, though with viscoelastic effects distorting the latter. Results are in agreement with previous experimentation. The role of adhesion is discussed and, in agreement with literature, it is speculated that the strength of adhesion is greater than or equal to that of the bulk polymer.

ACKNOWLEDGMENTS

Peter Anthony Sable, M.S., E.I.T.

There are many individuals without which none of this would have been possible, and I would be remiss if they weren't given their due. It must be disclaimed, of course, that this list is not exhaustive and I happily quote Newton in saying I have been "standing upon the shoulders of giants", giants in friendship, camaraderie, and mentorship, as well as that of intellect.

First, I am profoundly grateful for the support of my adviser Dr. John Borg. He has gifted me with countless hours of thoughtful guidance and encouragement throughout my time at Marquette, and I very much owe him any semblance of success I may be blessed with as my career moves forward.

In the same vein, working for Dr. Borg has given me the opportunity to work alongside some of the best minds and indeed people I will ever meet. While the endearingly termed "Borg Collective" has grown quite a bit over the years I wish to particularly thank Dr. Jeff Lajeunesse, Mr. Merit Schumaker, and to-be-Dr. Chris Johnson. Working and learning alongside them has been an honor and privilege.

I am (of course) deeply indebted to my dissertation committee for coming along with me on this graduate school journey. The wealth of knowledge and experience made available by Drs. Kit Neel, John Moore, Dinc Erdeniz, and Casey Allen goes beyond words and without their insights I would still be lost trying making sense of my own data. Kit's mentorship was particularly crucial - the time he invested in my internships at AFRL taught me the precise and thoughtful technical acumen necessary to be successful in shock physics.

Dave Newman, the Director of Operations for the MU College of Engineering and head of the Structural and Mechanical Testing labs at Marquette, was (and is) both a profoundly good teacher and a steadfast friend and mentor. His lessons both with regard to my experimental process and life in general were invaluable. His staff, particularly Mr. Tom Silman and Geno Johnson at the Machine Shop and Discovery Learning Lab, performed the amazing task of teaching me to use a lathe and mill and further made the theory in my head a reality.

One of the greatest favors Dr. Borg imparted me was introductions into the Shock Physics community. In doing so, I have gotten the chance to work and interact with some incredible people such as Arne Gullerud, Eric Harstad, and Gene Hertel at Sandia National Labs, the brilliant Dr. Mike Rauls who taught me how to build a PDV while he was at CalTech, as well as Dr. David Lacina, Jason Hipp, Rick Davis, Adam White, Josh McKean, and Tony Cuneo out at the AFRL's HP3 facility.

I would like to gratefully acknowledge my funding for this work through the Science, Mathematics, and Research for Transformation (SMART) scholarship

part of the National Defense Education Program sponsored by the Department of Defense. Particular thanks goes to my facility sponsor at AFRL/RW, Angela Diggs, who has been an excellent ambassador between the worlds of DOD and academia and has been kind enough to answer all of my many questions about the program.

As I said, this unfortunately can't be an exhaustive list, but I will end with a final thank you to my family and friends outside of graduate school. I couldn't have done any of this without their patience and support. Thank you all.

DEDICATION

The author would like to dedicate this endeavor to the family, friends, teachers, and mentors, without which none of it would have been possible.

Verba volant scripta manent.

TABLE OF CONTENTS

LIST OF TABLES

LIST OF FIGURES

CHAPTER 1

INTRODUCTION

1.1 Motivation

The characterization of dynamic polymer behavior is a critical area of research driven by the use of polymers as adhesives, structural components, or even as binders for energetic systems. In many of these applications, polymer components or constituents are often subjected to high magnitude stresses and multi-dimensional loading conditions. To facilitate effective engineering design and predictive modeling, the response of polymer materials must be experimentally observed and quantified over a robust range of loading conditions only a limited few of which have been investigated thus far.

Significant effort has been devoted to performing characterizations such as tensile, compressive, and flexural strength measurements along with more derivative or relative metrics such as hardness, and durometer testing [13][14][15]. These data sets are extensive and incorporate a wide range of potential dependencies such as temperature (the glassy transition), loading history, and polymer chemistry (molecular weight and chain length). The overall mechanical response is highly nonlinear, which has lead to the development of unique *viscoelastic* models to capture the various time, pressure, temperature, and strain-rate dependencies [16] [17]. The majority of mechanical testing done was conducted over strain-rates ranging from 10^{-2} to $10^{3}s^{-1}$, limiting any resulting models to applicability only in this regime. To understand behavior at more extreme loading conditions light gas-gun tests, specifically uniaxial flyer-plate impact experiments ($> 10^{5}s^{-1}$), has been used to establish reference equations-of-state called (*Hugoniots*) for a variety of relevant polymers. Flyer-plate impact tests induce near-ideal one-dimensional

longitudinal stress waves within a target of interest, ranging in magnitude from <1 to 20 GPa [18] [19]. These experiments provide significant information regarding material thermodynamics, however they provide little insight into off-Hugoniot (non-uniaxial impact) or shear strength behaviors as loading often well exceeds material strength.

This leaves a niche gap in understanding. The threshold for material plasticity in polymers (described through yield criteria or surface) has been shown to be a function of shear (deviatoric) stress and pressure (volumetric) loading. Such behavior could be described by the known Mohr-Coulomb or Drucker-Prager [20] [21] models, but such relationships have remained relatively unexplored as acquiring such shear data at high strain-rates requires more complicated testing methodologies. One approach is the oblique impact experiment, wherein an angled projectile impacts a target aligned to the same angle. On impact a normal and shear stress wave propagate away from the impact surface, with induced strain-rates of approximately $10^5 s^{-1}$ [22]. These tests have been used to observe the pressure-shear response of a many materials at high strain-rate further detailed in *Background Literature*, and are uniquely suited to observe off-Hugoniot behavior. Researchers have already leveraged this approach, investigating polyurea and polycarbonate [23–25].

While the bulk shear strength behavior is of interest implicitly, a common role of polymers in application is to serve as an adhesive between substrates. This expands interest to include surface traction dynamics occurring at a polymer-substrate bonded interface - i.e. dynamic friction and adhesive bond strength characterization. Data on these phenomena is nonexistent for polymers (at high strain-rate), and warrants further study. Friction between metal tribological pairs have been considered, also using oblique impact, the results which would suggest the method would be equally suitable for polymers [26].

1.1.1 Objective

The present work sought to characterize surface tractions and the material shear response of two polymers undergoing combined pressure-shear (off-Hugoniot) loading at high strain-rate. This was done in an effort to (1) further the current understanding of dynamic polymer behavior facilitating more robust constitutive modeling, and (2) expand the limited library of empirical data regarding the shear response and strength of polymers with effort given to isolating the effect of adhesion from that of the bulk material. Fully dense, thermosetting, a two-component polyurethane and epoxy (of high durometer) was selected as materials of interest. This choice was primarily due to their commonality in applications across various industries, and their ease of acquisition. Polymers were subjected to normal and shear stress wave loading via oblique impact experimentation, and the corresponding dynamic response was observed. Two different experimental configurations were utilized to to observe either material and adhesive bond yielding or dynamic friction behaviors. By varying both impact velocity and angle of obliquity, the implication of magnitude as well as ratio of pressure to shear stress are explored. Due to the interest in adhesion, attention was given to surface preparation in an effort to identify any effect of surface roughness on traction dynamics. To demonstrate the applicability of these results, data was used to inform computational simulations conducted in the large-deformation Eulerian hydrocode CTH [27]. Hugoniot and yield strength data were implemented into Mie-Gruneisen equation-of-state and a simple pressure dependent ”Geo-Yield” constitutive model in an effort to reproduce experimental wave-profiles. Simulations were two-dimensional, with geometries representative of the experimental set up. Supplementing observed results, a series of mesoscale simulations were then done to resolve surface roughness and to consider potential effects.

1.2 Background Literature

Polymer materials have been in use far preceding written record beginning with the indigenous peoples of South America making use of the naturally occurring rubber tree [17]. Although always known for their unique elastic properties, polymers were not widely implemented until the mid 1800's when significant advances in processing (molding) and vulcanization were made [28]. Even with common usage, a rigorous understanding of molecular chains and their contribution to unique mechanical properties was not developed until the mid 1900's [29]. Since then, applications have become countless. Materials such as Teflon (brand name for polytetrafluoroethylene or PTFE) and nylons are household names used in commercial products. Polymer adhesives from basic glues to high strength epoxies can be found in both commercial and industrial applications [30]. There are even more niche roles such as binders for energetic composites [31]. Polymers have become particularly important in the development of additive manufacturing as a field, serving as a printable media [32].

This study focuses on specific industrial formulations of either a polyurethane or epoxy. Both are two-part amorphous thermosets. Both were among the first polymers to be artificially synthesized, first by Schlack in 1934 and by Bayer in 1937 for epoxy and polyurethane respectively [33][34]. Together, these polymer groups make up about 30 percent of the total thermosets in production within the United States [17]. Polyurethane can be found as both a thermoplastic and a thermoset, depending on formulation, with thermosetting being more typical. They are synthesized by reacting a poly-isocyanate with a polyol, making it a copolymer constructed of alternating monomers. Both isocyanates (functional group: R–N=C=O) and polyols (meaning multiple hydroxyl groups) each representing a range of possible chemical compositions, which in turn results in wide variations

in polyurethane material properties [35–38]. Epoxies are created through the reaction of a polyepoxide (epoxy resin) with another polyepoxide and/or a catalyst agent, which in either case is termed a hardener. Final material properties can vary, similar to polyurethane, dependent on additives and curing methods [39–41]. Figure 1-1 shows general examples of the chemical structure for both polyurethane and epoxide monomers [1][2].

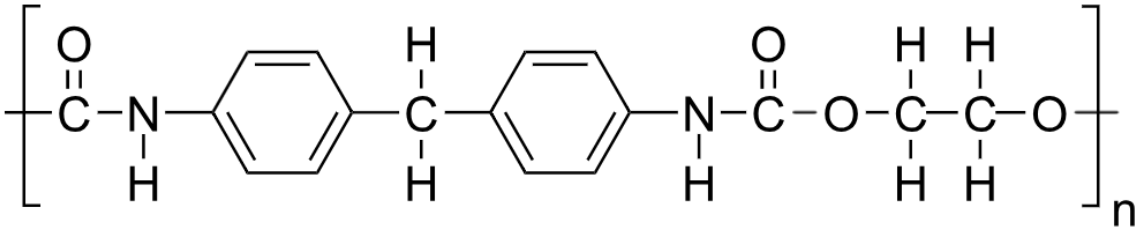

Fig. 1-1. Chemical structure of a polyurethane monomer composed of alternating isocyanate and polyol groups, from [1].

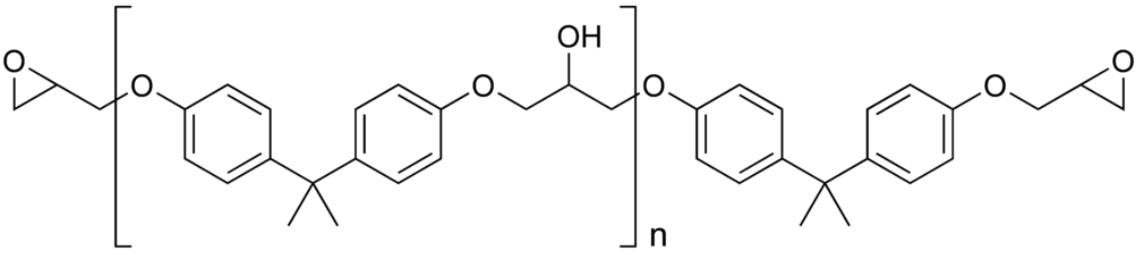

Fig. 1-2. Chemical structure of an epoxide group, from [2].

The excessive variations possible in chemical structure are what have enabled polymers to become a staple in commercial, industrial, and military applications, as they can many times be tailor-made for a given purpose. The same variability makes the characterization of polymers particularly difficult, as material properties are very dependent on chemical structure [42]. Precise details

concerning chemical composition and synthesis are often proprietary, meaning assumptions of material properties based on chemical structure cannot always be made.

While not an exhaustive list, mechanical characteristics of interest include adhesive bonding, friction coefficients, time dependent stress/strain response (creep), viscoelasticity, as well as the temperature and strain-rate dependence of strength [13][43]. Isolating these behaviors necessitates a variety of different tests with varying degrees of complexity. More traditional techniques include tensile testing [44] and Charpy-impact/fracture testing [45][46], which define both uniaxial and flexural properties [47]. More unique behaviors such as creep are tested by placing a polymer under constant stress loading (at a constant temperature), and observing the viscous approach to strain equilibrium. Inversely, constant deformation is provided and the stress response slow decays, i.e. relaxation [48]. Both phenomena demonstrate the time dependence of polymer mechanical response, and are further dependent on other factors such as temperature, molecular weight, crystallinity, and cross-linking [3, 17, 49–51]. This is perhaps best presented in terms of moduli funcationality. Figure 1-3 shows shear modulus as a function of both temperature and cross-linking [3].

The mechanisms behind these nonlinearities are currently thought to be the superposition of monomer chain interactions and bond kinetics within the monomers themselves. Analytically, the transience of mechanical behavior is modeled by introducing a viscous term into the constitutive relationship, the resulting mathematics fittingly termed *viscoelasticity* [4, 16, 43, 52].

Mechanical response is known to be both pressure and strain-rate dependent [52][42], as alluded to earlier and of which is of particular interest to this study. Several methodologies exist which may provide these necessary high pressure or strain-rate conditions in a laboratory setting. The split Hopkinson bar test

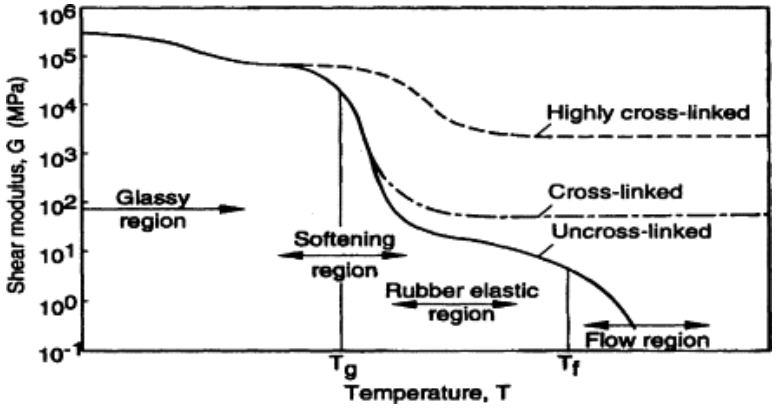

Fig. 1-3. Generalized behavior of polymer shear moduli over a range of temperatures. The role of crosslinking is shown, a characteristic common of thermosetting polymers and copolymers, from [3].

is capable of subjecting specimens to strain-rates on the order of 10^{-2} to $10^{2}s^{-1}$ [53–55]. Experimental data in this loading regime indicates increased magnitude of yield stresses as well as stiffening of moduli, with viscoelastic effects such as relaxation still observable [56][57]. Wherein, a striker impacts an incident bar which serves to propagate a stress wave of desired shape and magnitude into a specimen. Since both the striker and down stream bar remain elastic, the upper limit of stress imparted on each sample is a function of the acoustic impedance of each bar. Using confined-sample compression tests, Rittel and colleagues demonstrate successfully quantified both pressure and strain-rate dependencies in strength, with loading conditions up to 200 MPa and 5,000 s^{-1} imposted [58]. Similar behavior has been identified in polymer foams [59]. Figure 1-4 presents literature data demonstrating the aforementioned strain-rate effects specifically in terms of elastic moduli and strength normalized by temperature [4][5].

Both stress and strain-rate loading conditions may be extended in magnitude by performing uniaxial flyer-plate impact tests, in which a light-gas gun is used to propel a flat, planar, projectile into a target of interest. This induces a one-dimensional pressure wave into the target causing plane strain deformation at up

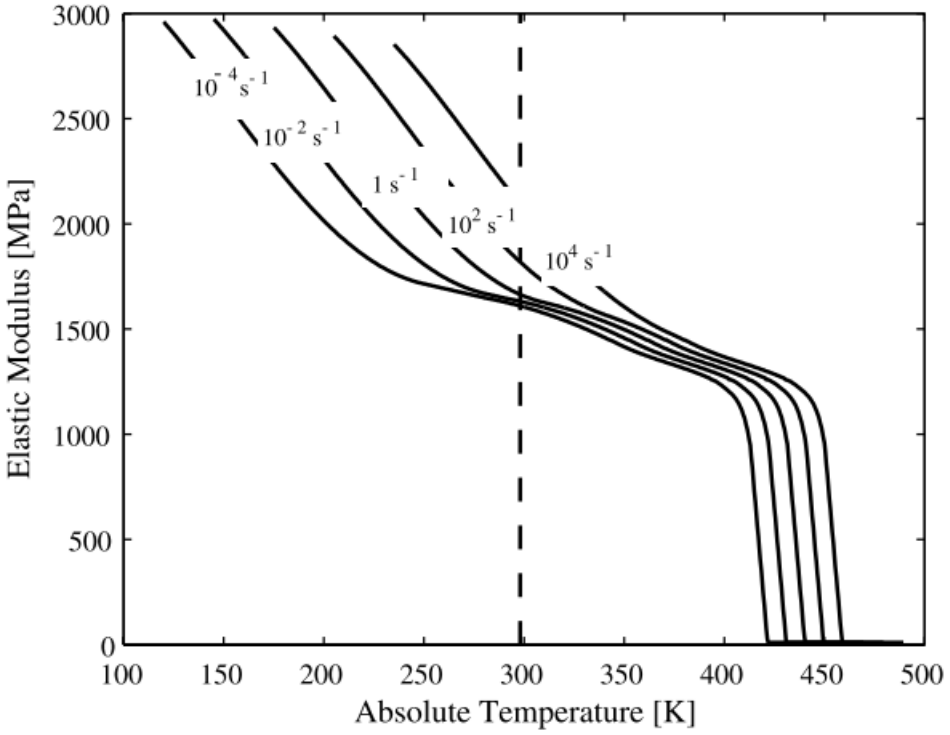

Fig. 1-4. Effect of strain-rate on polycarbonate elastic modulus, from [4].

to $10^6 s^{-1}$ and <1 to 20 GPa [18, 19, 60]. High strain-rate uniaxial (plane strain) testing has led to particularly interesting results, presented originally in the seminal study done by Barker and Hollenbach [61]. They observed a unique rounding phenomena present in shock waves propagating through polymers, and the distinct absence of an elastic precursor wave, typically present upon the stress level exceeding the elastic limit. Both this rounding and the absence of an elastic precursor are hypothesized to be the high strain-rate manifestation of viscoelasticity (sometimes termed *viscoplasticity*) [61]. The precise molecular interactions behind these are still not clear.

A strong foundation of research in dynamic polymer behavior has accumulated from such experimentation, with significant efforts being devoted to both Hugoniot equation-of-state development and characterization of potential viscoelas-

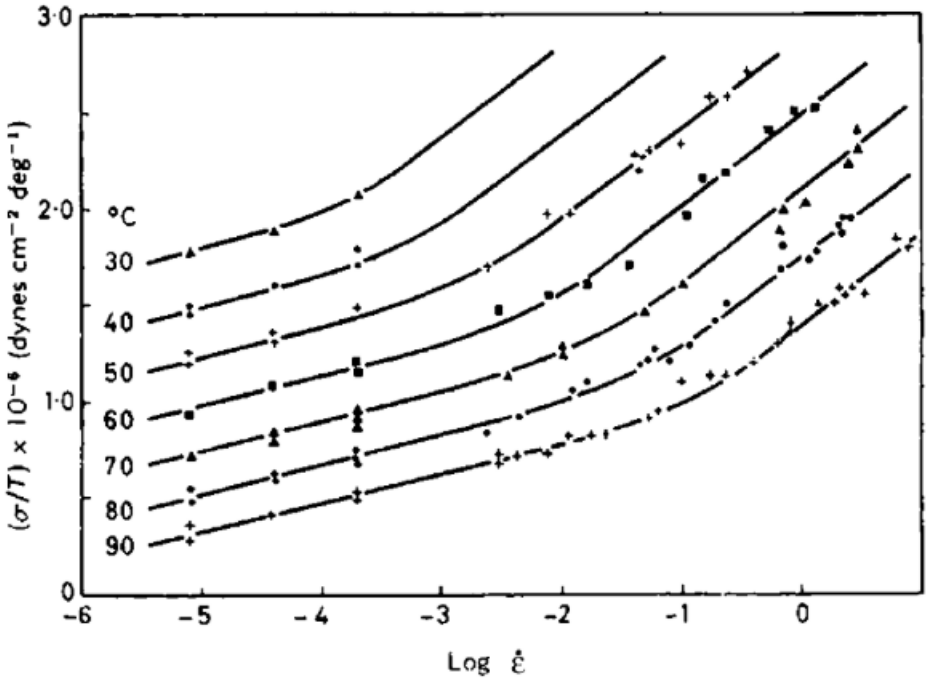

Fig. 1-5. Effect of strain-rate on polymethylmethacrylate yield strength, from [5].

tic effects seen in shock structure [21,62–69]. In compliment, traditional flyer-plate impact testing was modified in the form of oblique impact experiments [22]. This allowed specimens to be subject to pressure *and* shear stress wave loading, and enabled the characterization of material shear response at high strain-rate. Studies have included homogeneous metals such as aluminum and copper as well as heterogeneous granular materials like tungsten carbide and sand [70–74]. Several studies have even evaluated the elastodyrodynamics of non-Newtonian lubricant fluids and pressure-shear loading [75–77]. Overall, experiments have enabled the observation and eventual modeling of rate-dependent strength, yield surfaces, and have demonstrated the differences in damage caused due to combined stress loading.

Despite the useful insights provided by oblique impact experiments, they are difficult to execute. This is primarily due to the necessity of a slotted bore

gun, which ensures the obliquity of the projectile is maintained via a keyed projectile. Experimental setup procedures are also more rigorous. Greater alignment precision is required due to the greater experimental uncertainty introduced by impact tilt. Additionally, transverse wave measurements are needed to quantify shear which is non-trivial. Such complications necessitate expensive and complex infrastructure which has resulted in relatively few tests being performed. For example, investigations of only a few polymers were found in literature, specifically polyurea and polycarbonate [23–25]. Similar polyurethane elastomers and another polycarbonate were also explored using electromagnetic diagnostics [78,79]. These were able to identify increases in shearing resistance (strength) at higher pressures, and latter few investigations observed changes in modulus related to the glass transition - expected for thermoplastics or semi-crystalline polymers. These previous efforts are fortuitous as they provide useful points of comparison despite this studies focus on thermosetting polymers.

Oblique impact is also well suited to explore dynamic friction behaviors. Through careful design consideration, the pressure and shear stresses at the impact interface is measurable, the ratio of which quantifies either a static or dynamic coefficient of friction depending on the presence of slip. This has already been done on various metal tribological pairs [26,80], though a gap in knowledge (relevant to this work) remains with no studies found on polymers of any kind.

In addition to Coulombic friction, polymers may also exhibit adhesion to a substrate surface and must be included when considering the interaction of polymer surfaces. This is of particular interest to the scientific community given the prevalence of polymers used as *adhesives*. Israelachvili summarizes the concept well in *Intermolecular and Surface Forces* [6], visually presented in Figure 1-6. It is hypothesized when two surfaces are in contact, shearing is resisted by either topological obstacles or intermolecular forces formed chemically [9, 81]. Intuitively,

both have been found to vary with surface topology [82, 83]. Figure 1-6 demonstrates the concepts behind asperity-driven (topological, non-chemical) friction.

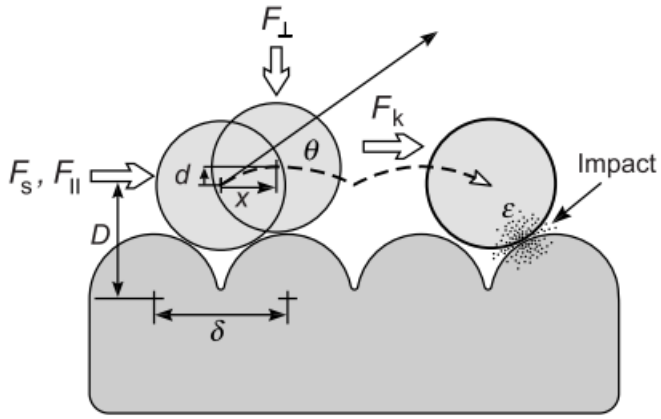

Fig. 1-6. Cartoon demonstrating friction surface interactions, from [6].

Results from quasi-static testing have shown a consistent correlation between these asperities and interface strength [6, 82, 84, 85]. Given the plethora of applications, many studies have been conducted in this vein investigated polymer strength particularly in the context of thin films and their related friction behavior [6, 9, 86–90]. These investigations, over time, have established a strong pressure dependence for both polymer strength both as a bulk material and as a thin-film adhesive. Though this has not as of yet been experimentally extended to high strain-rate ($> 10^4 s^{-1}$) conditions with the exception of polycarbonate, PMMA, and polyurea [24, 25, 78].

It is the composition of all of these behaviors; pressure dependence strengthening, strain-rate sensitivity, and other phenomena all attributed to viscoelasticity, which manifest in the final bulk response. A seminal goal is to, therefore, be able to mathematically model this behavior. this is non-trivial and is done through the

development of highly nonlinear constitutive models, most containing many parameters which must be empirically fit from data [52,91–94].

As has been demonstrated, the dynamic behavior of polymers has a strong foundation of literature, the culmination of which was the driver behind the already discussed motivation and objectives for the effort reported here. Restated with context now in mind, this work intends to characterize the response of two polymers undergoing combined pressure-shear (off-Hugoniot) stress/traction loading at high strain-rate. This serves to (1) further the current understanding of dynamic polymer behavior facilitating more robust constitutive modeling, and (2) expand the limited library of empirical data regarding the shear response and strength of polymers with effort given to isolating the effect of adhesion from that of the bulk material.

1.3 Organization

Following the preceding motivation and background, this dissertation is organized into three parts including: theory, technical reports separated by objective subtopic, and overall conclusions. Theory includes a review of all mathematical framework necessary to conduct included experiments, perform data analysis, and the basis needed for any later-posed conclusions or hypotheses. The study objective was sub-divided into preliminary material characterization, yield behaviors of polymers at high strain-rate, dynamic friction behavior of polymers, and the implementation of data into computational simulation. As such, results are presented in the form of separate reports for each subtopic and (aside from preliminary characterization) each have the format of: brief introduction, methodology, and results/discussion. Some repetition will exist within each introduction such that the sections may be read more-or-less independently, but is avoided when possible. Final observations and discussion taken from all experimentation and simulations are coalesced into a single *Conclusions* section along with suggestions for future work. Supplemental information including detailed target designs, the polymer molding process, step-by-step data analysis, and a more comprehensive library of figures showing relevant individual experiment profiles are included in the appendices.

CHAPTER 2

THEORY

Imparting extreme pressure and temperature conditions reveal unique behaviors such as strain-hardening, rate/history dependence, and even phase transitions. The understanding of these are critical to the development of predictive models and for the design of systems experiencing such conditions. Characteristic of these extreme states are very large magnitude stresses (>1 GPa) over a duration of very small time scales (nano- to micro- seconds). To achieve these conditions in an laboratory setting, materials are often subjected to shock wave loading using gas or explosive-based techniques used to rapidly impacting materials into one another. Defined, a shock is a wave traveling faster than the local sound speed of the medium which drives the material to a state of higher stress, temperature, and density. The thickness of the shock, or the boundary between un-shocked and shocked material, is nearly discontinuous and may be treated as such mathematically [95][96]. Depending on experimental conditions, near-ideal one dimensional waves may be produced simplifying the problem into tractable governing equations, which are expressed through classic conservation laws closed by a material equation-of-state (EOS) and constitutive model. Conditions may be varied to produce (technically non-shock) elastic or elastic-plastic waves depending on the phenomena of interest.

In the context of this work, three variations of impact experiments were conducted, one plane-strain (uniaxial) and two oblique. All configurations used light gas guns to propel a projectile package down a barrel at a known velocity, at which point impact between the projectile and target resulted in high magnitudes of stress loading. The following section provides the theoretical framework necessary for analysis of experiments and includes an overview of uniaxial/oblique

impact physics as well as a conceptual discussion regarding friction, adhesion, and strength of polymers.

2.1 Shock Compression and Uniaxial Impact

Uniaxial (plane-strain) flyer-plate impact experiments are conducted such that an impactor/sabot projectile package impacts a target in a uniaxial manner. The impactor typically consists of a known material with well-characterized shock properties, whereas the target is the un-characterized material of interest. A one-dimensional shock wave is generated at the interface and propagates into both the impactor and target. Figure 2-1 provides a visual representation including a cartoon schematic with wave propagation annotated, including pressure release induced by free surface edges, and an idealized wave structure.

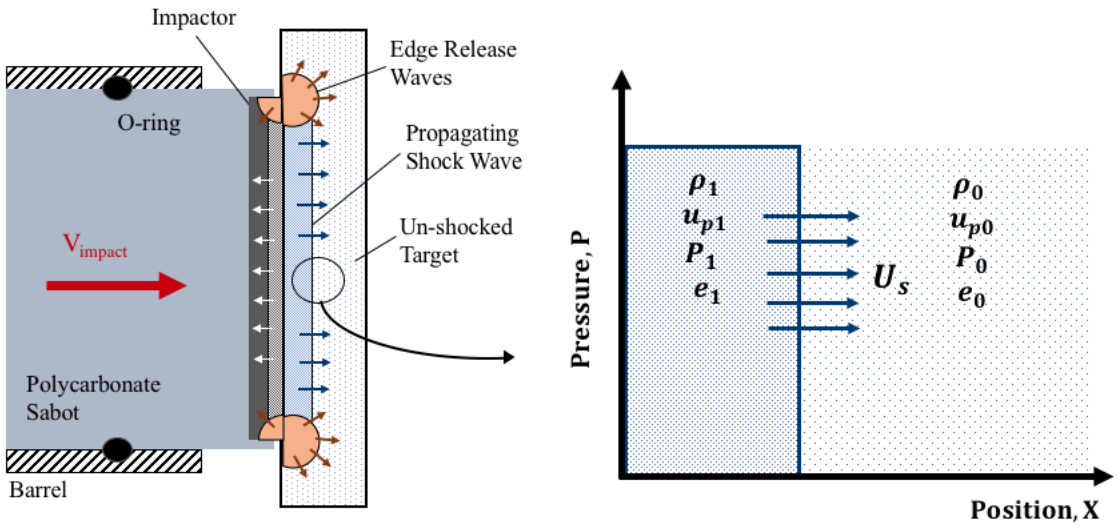

Fig. 2-1. A representative plane-strain flyer-plate impact experiment including a cartoon schematic showing impact and wave propagation.

The relationship between shocked and unshocked properties are related through the conservation of mass, momentum, and energy taken across the shock

front assuming a constant cross section. These are known as the Rankine-Hugoniot jump conditions and, if wave propagation is assumed steady, are expressed as eqs. 2.1 2.2 and 2.3.

$$\frac{\rho_1}{\rho_0} = \frac{U_s - u_{p0}}{U_s - u_{p1}} \tag{2.1}$$

$$P_1 - P_0 = \rho_0(u_{p1} - u_{p0})(U_s - u_{p0}) \tag{2.2}$$

$$e_1 - e_0 = \frac{P_1 u_{p1} - P_0 u_{p0}}{\rho_0(U_s - u_{p0})} - \frac{1}{2}({u_{p1}}^2 - {u_{p0}}^2) \tag{2.3}$$

where ρ is density, U_s is shock wave speed, u_p is particle velocity prior to or after wave arrival, P is pressure (compression is considered positive), and e is internal energy. There are five total variables with three governing equation. This infers some combination of shock-state pressure, particle velocity, density, or shock velocity must be measured to have a well posed problem and fix the thermodynamic state. At this point *strength of material has been neglected* and only material hydrodynamics are considered, the justifications for which will be provided shortly. Impacting a given material at a variety of velocities results in a different induced pressures (and thus shock speeds). The locus of (all of) these end-states defines a material *Hugoniot*. This path represents all possible thermodynamic states corresponding with uniaxial impact conditions. This is comparable in concept to the isentrope which is the path of all possible thermodynamic states of a material assuming no entropy is generated throughout a given process. Notably, at lower impact pressures the material Hugoniot closely approximates the isentrope. Over

the duration of a shock the only heat generated is due to compressive work (dilitation), and as such at lower impact pressures very little heat, and so entropy, is generated. Figure 2-2 shows a generic Hugoniot in $\sigma - v$, $U_s - u_p$, and $P - v - T$ with the last showing a comparison of a Hugoniot to a corresponding isentrope and isotherm [7].

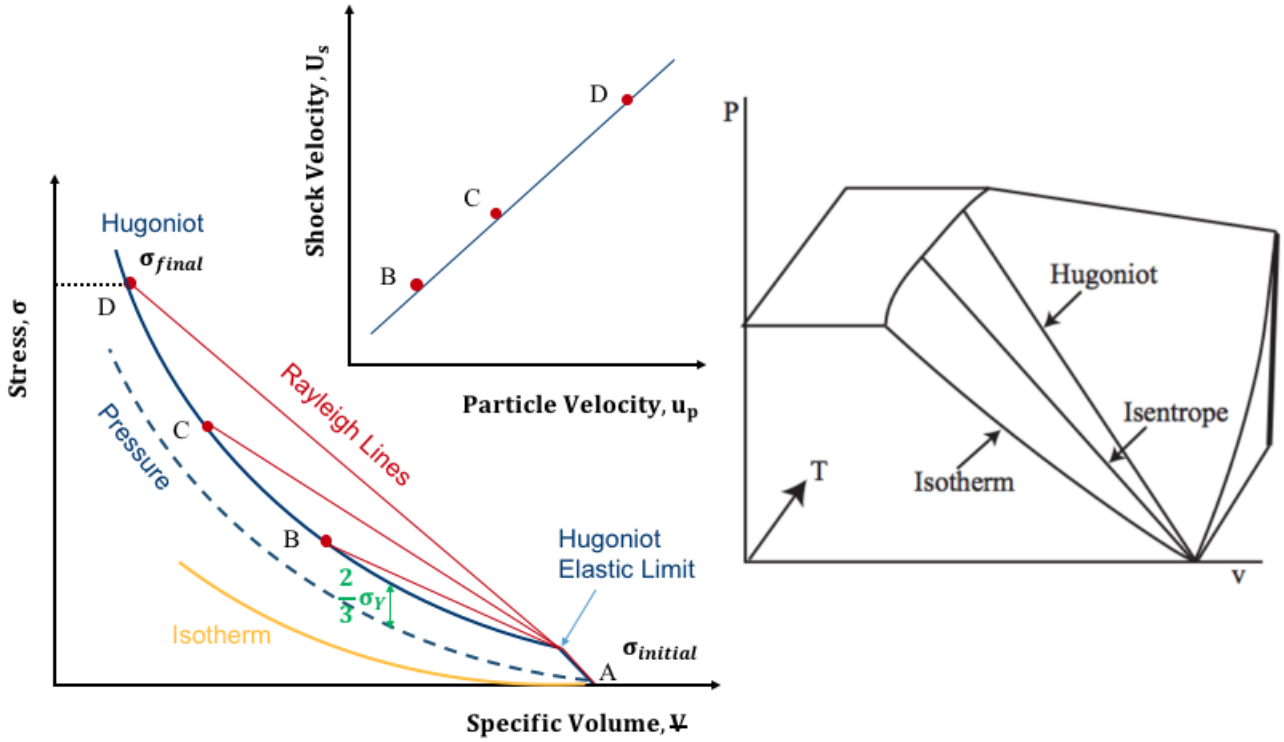

Fig. 2-2. An example Hugoniot shown in $\sigma - v$ and $U_s - u_p$ space as well as in the context of a full $P - v - T$ thermodynamic surface [7]. Note $\sigma - v$ shows a measured Hugoniot which would include contributions from both thermodynamic pressure and material strength.

In Figure 2-2, three distinct shock loading processes are shown driving the material from state A at an initial $\sigma_{initial}$ to final states B, C, or D with a σ_{final}. In $\sigma - v$ space, the unshocked and shocked states are connected by something called a *Rayleigh line*. The slope of this line is indicative of the shock wave impedance or magnitude of shock loading. A Hugoniot must be taken with respect to some

reference state. Commonly this (point A) is the unloaded material state at room temperature and zero pressure with most experiments conducted under near vacuum (<200 mtorr).

A quick distinction should be made between stress σ and pressure P. Total stress σ in a material has contributions from both volumetric dilatation (hydrostatic pressure) and deviatoric stresses dependent on material strength. In experiment, the total material stress is measured not just pressure and so implications of strength must be considered. This will be expounded shortly, however note that Figure 2-2 schematically shows the thermodynamic pressure alongside an idealized material Hugoniot including strength. This is the *reference Hugoniot*, and is the most persistent in literature.

Many material Hugoniots show a linear relationship in $U_s - u_p$ space, defined simply by the two-parameter eq 2.4.

$$U_s = su_p + C_0 \tag{2.4}$$

where s is a slope term and C_0 is the intercept. C_0 is in units of velocity and closely approximates the materials bulk sound speed, at atmospheric pressure and temperature, however is defined only as the intercept of the Hugoniot at the ordinate and is technically speaking non-physical. This an important distinction as C_0 does not capture the complexities of elastic to elastic-plastic/plastic behavior.

This empirical relationship can further be used as a closure equation in conjunction with the conservation laws. While not a complete equation-of-state (EOS) in an of itself (lacking any temperature consideration), the parameters can be readily implemented into a *Mie-Gruneisen* EOS. This has the form of eq 2.5,

$$P = \frac{\rho_0 {C_0}^2 \chi[1 - \frac{\Gamma_0}{2}\chi]}{(1 - s\chi)^2} + \Gamma_0 \rho_0 c_v \Delta T, \; where \; \chi = 1 - \frac{\rho_0}{\rho} \tag{2.5}$$

This includes a compression term χ, constant volume heat capacity c_v, and change in temperature ΔT. The Gruneisen coefficient at the reference state Γ_0, is based analytically on vibration in a solid's lattice structure and may be determined experimentally [97] [98]. Temperature increase is assumed to be due to increasing internal energy related by the heat capacity.

Further clarification regarding "pressure" and "stress" is useful as they are sometimes used interchangeably which is incorrect. Upon loading, uniaxial impact results in a longitudinal stress σ_{11}, where 11 describes the shot direction x of the plane orthogonal to x. This induces stress in the off-axis (σ_{22} and σ_{33}) due to Poisson effects, i.e. plane-strain deformation. Keeping this coordinate system, loading produces only pressure terms (elements of the Cauchy stress tensor diagonal), but what is measured is the longitudinal stress, from which the other terms may be inferred. For materials with Poisson's ratios $\nu \approx \frac{1}{2}$, $\sigma_{11} \approx \sigma_{22} = \sigma_{33}$, which given $P = \frac{1}{3}(\sigma_{11} + \sigma_{22} + \sigma_{33})$ infers $P \approx \sigma_{11}$. This is a special case, however, and otherwise pressure is only a portion of the longitudinal stress. Stress here refers specifically to elements of the third order Cauchy stress tensor. A complete continuum mechanics analysis of the uniaxial impact problem can be found in *Fundamentals of Shock Wave Propagation in Solids* [99] and *Shock Compression of Condensed Matter: A Primer* [100]. In short thermomechanical pressure is only a component of stress.

Including material strength in Hugoniot behavior, three possible regimes become apparent: an elastic regime, elastic-plastic transition, and a plastic regime. Figure 2-3 shows a Hugoniot now in longitudinal stress and volume ($\sigma_{11} - v$) space where the contribution of EOS pressure is shown separated. Distinguishing these regimes is best summarized by Cooper [95]. The elastic regime is defined as stress loading less than the Hugoniot Elastic Limit (HEL), which is the longitudinal stress

corresponding to material yield. Stress waves of this magnitude propagate at the constant material sound speed, resulting in a linear-elastic response and no irreversible deformation of the material. Once this threshold is exceeded, material yield begins to occur and a plastic wave begins to develop (elastic-plastic regime). Schematically this is seen as two Rayleigh lines, the first coming to the HEL, with a second jump then bringing the material to final stress. Greater slope of Rayleigh line, represents faster wave propagation. This corresponds with the two-wave structure seen in experiment, and is shown generically in Figure 2-3. At high enough stresses the the slope of Rayleigh line is greater than the that of the elastic regime, at which point the plastic wave over takes the elastic-precursor resulting in a single "strong" shock. In this regime material strength is great exceeded such that even solids behave as fluids. As such, strength is considered negligible and thermodynamic pressure is taken as the relevant metric for material response. This is called the hydrodynamic assumption.

More complicated (nonlinear) strength behaviors, caused by various dependencies, can very much affect the shape of the Hugoniot and even manifest in complicated shock wave structure. Even with strength far exceeded, physiochemical changes such as phase change can drive the material to a different Hugoniot altogether or other phenomena which would go unobserved in any other circumstance. For example, BCC iron shifts to an HCP crystalline structure when exposed to shock exceeding around 13 GPa [101]. This results in a three wave structure where you have an elastic precursor followed by a BCC-governed shock then an HCP-governed shock. Of course, additional methods are often necessary in confirming behaviors such as phase change, like post-mortem microscopy, in-situ x-ray diffraction imaging, or Raman spectroscopy, but the potential for their observation demonstrates the usefulness of impact experiments.

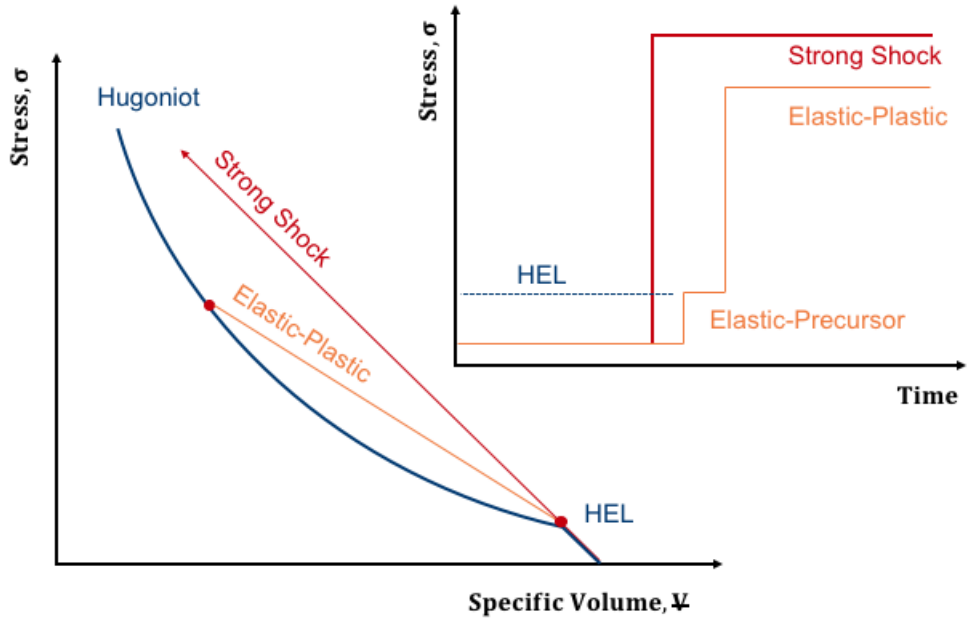

Fig. 2-3. Under uniaxial loading, a target can experience elastic, elastic-plastic, and plastic wave behaviors depending on impact conditions.

2.2 Pressure-Shear Wave Theory in Oblique Impact

While uniaxial plane-strain impact experiments are excellent for understanding material behavior at high pressures, they are limited in the loading conditions they may induce. Variable or combined stresses to produce off-Hugoniot thermodynamic states cannot be achieved, nor can shear be introduced which may effect yield behavior. While the implications of strength for many materials may be observed through the elastic precursor (recall the Hugoniot elastic limit), polymers specifically do not show HEL behavior and so no polymer strength information can be gleamed in traditional plane-strain tests.

Oblique impact experiments seek to supplement this, by leveraging similar gas gun methodologies to facilitate both normal and shear stress wave propagation within a material. This is accomplished by shooting a keyed projectile down a slotted barrel (Figure 2-4) which serves to maintain the obliquity and orientation

of an impactor set at an angle, θ. The target is aligned to the same angle such that the impactor/target surfaces are planar upon impact. Doing so, results in both a longitudinal (normal) and shear stress wave being imparted to the target [22].

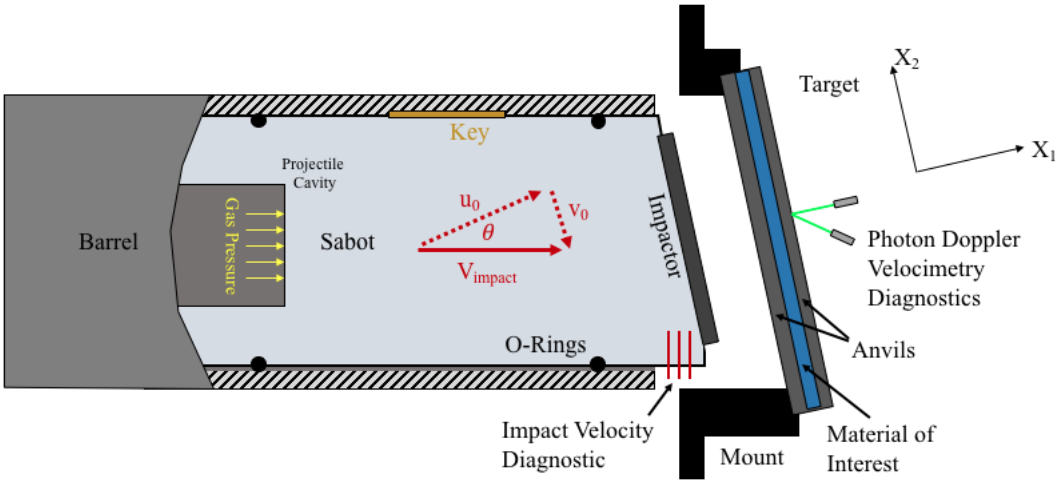

Fig. 2-4. The schematic of an oblique impact test, specifically a constant-pressure pressure-shear experiment wherein homogeneous pressure is attained within the material of interest prior to shearing.

For clarity, as with the uniaxial case, the longitudinal stress wave is many times referred to as a pressure wave. The term oblique impact experiment is often interchangeably used with *pressure-shear plate impact* (PSPI) experiments. To avoid any confusion it is worth re-specifying that a longitudinal σ_{11} wave propagates upon impact, which then induces only pressure terms within the Cauchy stress tensor. This assumes an $X_1 - X_2$ coordinate system aligned to the impact surface, shown in Figure 2-4. Moving forward, within the context of oblique impact, preference will be given to "normal stress" but the correspondence with pressure should be noted with respect to literature.

Pressure-Shear Plate Impact Experiments

The presence of two distinct waves requires additional considerations so they may be distinguishable and their effects isolated. This has led to several different variations depending on a given test objective. A common configuration is the *constant-pressure pressure-shear plate impact* (CPPSPI) experiment, pictured in Figure 2-4. In CPPSPI, the target consists of a thin layer of specimen material sandwiched between two anvils. Anvils are selected to remain elastic during loading. As such, they are typically high strength / high stress impedance materials, where impedance is define as $Z = \rho_0 C_B$ with C_B being the material bulk sound speed.

Elasticity ensures that only two distinct pressure and/or shear waves are ever present within the anvils (no elastic-plastic two wave structures), regardless of the potential stress state in the specimen. This also allows one-dimensional elastic wave theory to be used to infer sample stress from particle velocity histories taken off the rear back free surface [70,71,75,102].

Assuming a shot-direction impact velocity of V_p, and that the impactor and front anvil are of the same material (symmetric impact) the pressure and shear stress waves induce respective particle velocities of

$$u_0 = V_p cos\theta \tag{2.6}$$

$$v_0 = V_p sin\theta \tag{2.7}$$

where u_0 and v_0 are the longitudinal and transverse velocities within the front anvil associated with each stress wave, and θ is the angle of obliquity. While both waves propagate in the same direction, the way in which they distort material (longitudinal or transverse) is orthogonal, and so it is assumed they do not interfere with one another. Under the elastic assumption, each wave travels at a constant

sound speed of C_L (longitudinal) or C_S (transverse) within the anvil materials regardless of loading.

Given $C_L > C_S$, the pressure wave travels ahead of the shear wave reaching the specimen first. CPPSPI experiments leverage this, and the front anvil thickness is designed such that the pressure wave arrives and reverberates within the sample attaining a homogeneous state, all prior to shear wave arrival. Thus *constant-pressure* pressure-shear impact. This results in a more simplified pressure *then* shear stress loading of the specimen, allowing the material response to each to be decoupled. Figure 2-5 presents a representative position-time (X-t) diagram showing the expected wave propagation in a CPPSPI target. Using the X-t diagram as reference, experiment design then becomes a list of geometric constraints, timing steady-state pressure attainment against release waves from free surfaces and target edges. In general this requires a very "thin" specimen, usually less than a millimeter, particularly for very low impedance specimens which require more reverberations to attain homogeneous pressure. Specific design details such as the process of material selection and the limitation of impact conditions to maintain elasticity are provided in Appendix A, with experiment relevant details provided as needed in following sections.

Despite two wave-types being present, the problem still only depends on one spatial direction over time (X_1). As such elastic stress wave equations [102] simplify into a single elastic characteristic equations for each wave [75], represented by 2.8 and 2.9

$$\sigma_{11} = \sigma = (\rho_0 C_L)_F (u_0 - u) \tag{2.8}$$

$$\sigma_{12} = \tau = (\rho_0 C_s)_F (v_0 - v) \tag{2.9}$$

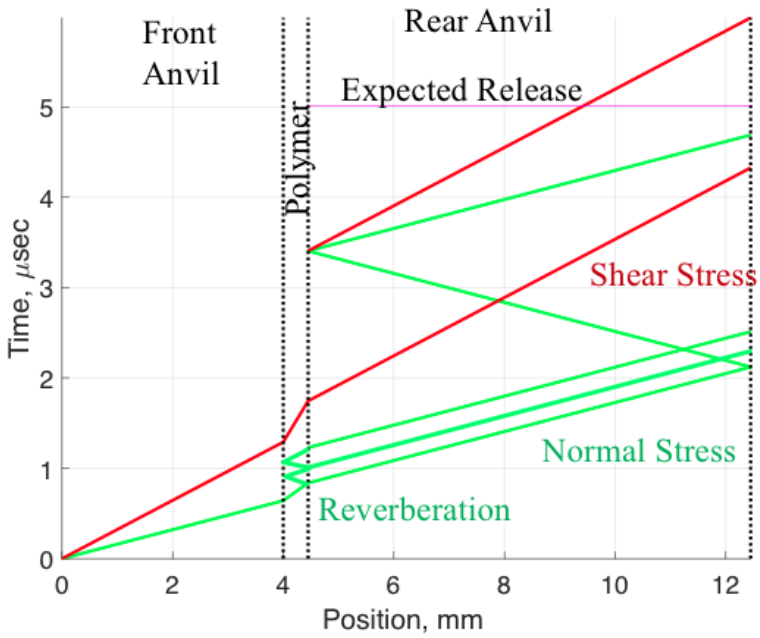

Fig. 2-5. An example X-t diagram demonstrating the expected wave propagation behavior in a CPPSPI experiment. The pressure wave arrives first, reverberating within the sample prior to shear wave arrival. Each reverberation step and eventual shear wave is transmitted through the rear anvil, and resulting particle velocities are measured off of the rear free surface.

where σ_{11} is normal stress, σ_{12} or τ is shear stress, u_0 and v_0 are the longitudinal and transverse particle velocities induced by oblique impact, $(\rho_0 C_L)_F$ is the longitudinal stress impedance of the front anvil, and $(\rho_0 C_s)_F$ is the shear stress impedance of the front anvil. Similarly, the rear anvil must follow 2.10 2.11.

$$\sigma_{11} = \sigma = (\rho_0 C_L)_R u \tag{2.10}$$

$$\sigma_{12} = \tau = (\rho_0 C_s)_R v \tag{2.11}$$

with stress impedance corresponding now to the rear anvil. Presented in this work the front and rear anvils are of the same material (7075-T6 aluminum), however to be general front anvil material properties are denoted F while rear anvil properties

are denoted R. Compression is considered positive by convention. Per enforcement of the conservation of momentum, the stress state of the specimen is confined by the anvil equations in both $\sigma_{11} - u$ and $\sigma_{12} - v$ space. This mathematically describes reverberation, and is shown in Figure 2-6.

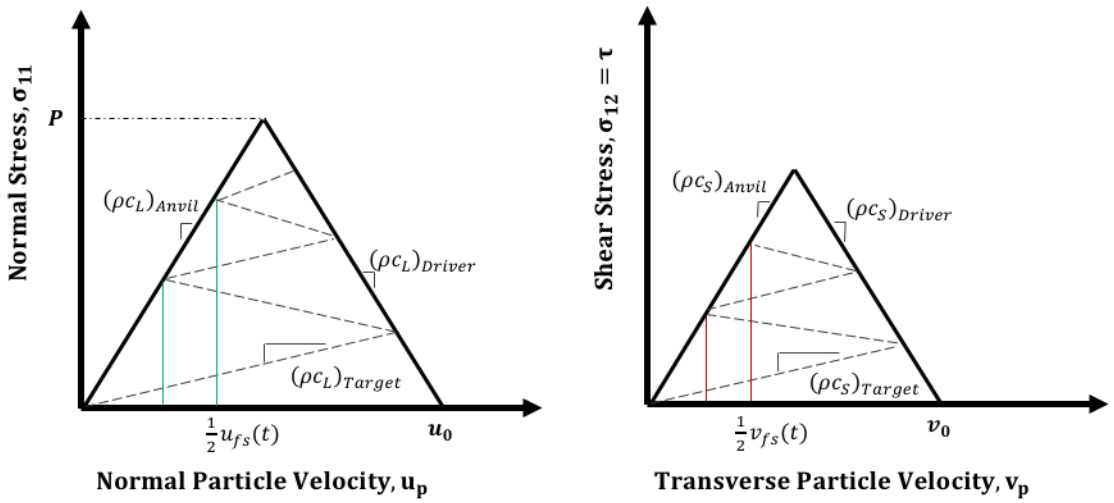

Fig. 2-6. Stress-particle velocity space for both longitudinal and shear stress loading of a specimen between two anvils corresponding to a CPPSPI experiment.

The expected homogeneous pressure ($P \approx \sigma_{eq}$) is found by assuming enough reverberations have occurred for the rear anvil/specimen interface to be in pressure equilibrium with the front anvil/specimen interface. At which point eq. 2.8 must be equal to eq. 2.10 resulting in eq. 2.12, which simplifies further to $\sigma_{eq} = \frac{1}{2}(\rho_0 C_L)u_0$ if the anvils are the same material [75].

$$\sigma_{eq} = \frac{(\rho_0 C_L)_F (\rho_0 C_L)_R}{(\rho_0 C_L)_F + (\rho_0 C_L)_R} u_0 \tag{2.12}$$

Precautions are taken to ensure the anvils remain elastic, but no such restrictions are placed on the sample itself. On the contrary, often the point of these experiments is to explore yield behavior. This makes analysis of the reverberations

themselves more complicated as it is unknown whether Hugoniot or elastic wave theory should be used. The impact speeds of these experiments are relatively low, inducing pressures less than a GPa. Even if a shock is developing within the sample, the speed would be less than or nearly equivalent to the sound speed. So for design purposes, in the context of this study, the sample is assumed elastic (at least during pressure reverberation) for the purposes of design. Post experiment, wave transit times may be examined directly and designs can be refined.

The u and v in eqs. 2.8 through 2.11 are particle velocities within the rear anvil, or more specifically this is the particle velocity induced at the specimen/rear anvil interface. Upon arrival at the free surface these release in stress corresponding to a increase particle velocities where

$$u_{fs} = 2u, \quad v_{fs} = 2v \tag{2.13}$$

Given free surface velocity histories u_{fs} and v_{fs} , and a known relationship between stress and said particle velocities, determining the combined stress state then becomes a diagnostic one. Free surface velocities are readily measurable via various interferometry technique like open optic normal/transverse displacement interferometry (NDI/TDI) or photon Doppler velocimetry [103] [104]. The yields final stress equations for the specimen of eqs. 2.14 and 2.15

$$\sigma = \frac{1}{2}(\rho_0 C_L)_R u_{fs} \tag{2.14}$$

$$\tau = \frac{1}{2}(\rho_0 C_s)_R v_{fs} \tag{2.15}$$

From these calculations, it is apparent by inspection that off-Hugoniot thermodynamic states are achievable and quantifiable, if only be the introduction of shear stress. However, another primary objective is to explore yield behavior and

so yield of the material specimen must be identifiable. If no-slip may be reasonably assumed, the maximum shear stress loading is known based on impact velocity, angle, and anvil impedance alone similar to eq. 2.12 where

$$\tau_{eq} = \frac{(\rho_0 C_s)_F (\rho_0 C_s)_R}{(\rho_0 C_s)_F + (\rho_0 C_s)_R} v_0 \tag{2.16}$$

or $\tau_{eq} = \frac{1}{2}(\rho_0 C_s)_R v_0$ for symmetric impact with equivalent anvil materials. For the simplest case, if it is assumed that after yielding a material can no longer support shear stress, then any shear stress that exceeds that yield criteria will not be transmitted through the specimen into the rear anvil. Therefore, at a given pressure, if the shear stress inferred from free surface velocities is less than the imparted shear, it is assumed to be the shear strength of the material, τ_y.

In this manner both thermodynamics and yield strength surface mechanics may be probed with this technique. For example, in a von-Mises material, strength is not pressure-dependent and so regardless of imparted σ the same τ_y would be expected. In contrast, a Drucker-Prager or Mohr-Coulomb material would show increase in τ_y linearly with increasing pressure. Figure 2-7 schematically projects CPPSPI experiment loading conditions onto a thermodynamic and then yield surface [7][8].

A further usage of CPPSPI experiments is to inform constitutive modeling of a material. This is somewhat implicit given the ability to map yield behavior, however is incomplete with the associated kinematics - enabling combined stress to be related to strain and strain-rate. First, assume an infinitesimal material element with the specimen of interest and that loading occurs in the order of pressure followed by shear only after pressure equilibrium has been attained. Then assume a coordinate system still consistent with Fig. 2-4, where $X_1 - X_2$ are angled from the shot direction by an angle θ. Local deformation can than be written as

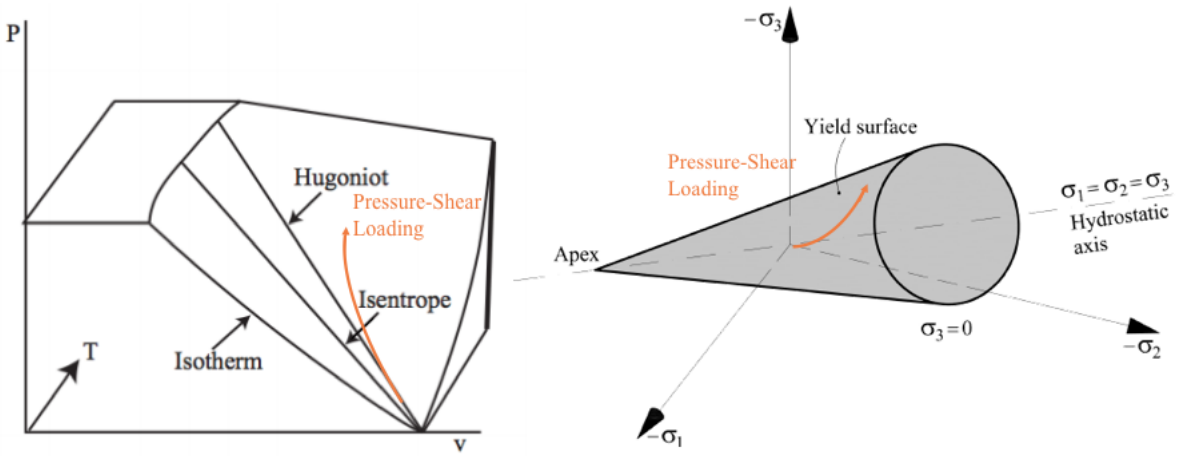

Fig. 2-7. Potential paths of pressure-shear stress loading on a thermodynamic surface and then a Drucker-Prager, pressure-dependent, yield surface in principle stress space [7] [8].

$$x_1 = \lambda(t)X_1,\ \ x_2 = X_2,\ \ x_3 = X_3 \tag{2.17}$$

for compression, a term here used in with respect to deformation only and not of stress. $x_{1,2,3}$ are the time dependent material locations with respect to the reference location $X_{1,2,3}$. $\lambda(t)$ is the time dependent variable which governs compression and is termed the "stretch". Assumed to occur at some time later, shear deformation equations take the form of

$$x_1 = X_1,\ \ x_2 = X_2 - \kappa(t)X_1,\ \ x_1 = X_1 \tag{2.18}$$

where $\kappa(t)$ is a coefficient proportional to shearing. Each set of eqs. 2.17 and 2.18 inform their own deformation matrix $\mathbf{F}^P$ *and* $\mathbf{F}^S$ where

$$F_P = \begin{bmatrix} \lambda & 0 & 0 \\ 0 & 1 & 0 \\ 0 & 0 & 1 \end{bmatrix} \ and\ F_S = \begin{bmatrix} 1 & 0 & 0 \\ -\kappa & 1 & 0 \\ 0 & 0 & 1 \end{bmatrix} \tag{2.19}$$

Combining each of these in order of occurrence (right to left), the complete deformation matrix over the entirety of the experiment then becomes **F**

$$F = F_S F_P = \begin{bmatrix} \lambda & 0 & 0 \\ -\kappa\lambda & 1 & 0 \\ 0 & 0 & 1 \end{bmatrix} \tag{2.20}$$

from which the Velocity Gradient or Strain-rate tensor may be calculated, giving **L**

$$L = \dot{F}F^{-1} = \begin{bmatrix} \frac{\dot{\lambda}}{\lambda} & 0 & 0 \\ -(\dot{\kappa} + \kappa\frac{\dot{\lambda}}{\lambda}) & 0 & 0 \\ 0 & 0 & 0 \end{bmatrix} \tag{2.21}$$

and finally the Rate of Deformation, **D**:

$$D = \frac{1}{2}(L + L^T) = \frac{1}{2}\begin{bmatrix} 2\frac{\dot{\lambda}}{\lambda} & -\dot{\kappa} - \kappa\frac{\dot{\lambda}}{\lambda} & 0 \\ -\dot{\kappa} - \kappa\frac{\dot{\lambda}}{\lambda} & 0 & 0 \\ 0 & 0 & 0 \end{bmatrix} \tag{2.22}$$

Note the dilatation of the material element is described by the first material invariant also called the Jacobian, $J = det(\mathbf{F}) = \lambda$, which is physically intuitive as compression should have the only effect on volumetric change. As pressure comes to equilibrium, the longitudinal strain-rate would decay meaning $\frac{\dot{\lambda}}{\lambda} \to 0$, simplifying the problem to simple shear. References for this derivation are found in [76][75][73]. These specific kinematic tensors are the building blocks of constitutive modeling. There derivation reveals additional experimental objectives necessary to define them, specifically the calculation of longitudinal and transverse strains and strain-rates. In the pressure-shear experiments, velocity histories are known, and strain-rates may be defined as

$$\dot{\epsilon} = \frac{\Delta u_{sample}}{h} \, and \, \dot{\gamma} = \frac{\Delta v_{sample}}{h} \tag{2.23}$$

where $\dot{\epsilon}$ and $\dot{\gamma}$ are the longitudinal and transverse strain-rates, Δu_{sample} and Δv_{sample} are the change in longitudinal and transverse velocity within the sample, and h is the samples initial thickness. Assuming a CPPSPI experiment done with anvils of the same material, this refines to

$$\dot{\epsilon} = \frac{u_0 - u_{fs}(t)}{h} \, and \, \dot{\gamma} = \frac{v_0 - v_{fs}(t)}{h} \tag{2.24}$$

where all variables are known. Transient strains are then simply calculated by through the integration of each strain-rate over the entirety of the experiment, or

$$\epsilon = \int_0^t \dot{\epsilon}(t)dt \, and \, \gamma = \int_0^t \dot{\gamma}(t)dt \tag{2.25}$$

Strain and strain-rate information may then be implemented directly into kinematic tensors, and proportionality terms for compression and shear deformation can be seen to be equivalent to $\lambda = 1 - \epsilon$ and $\kappa = \gamma$

Dynamic Friction Impact Experiments

An alternative test to CPPSPI is the *Dynamic Friction Impact* experiment. Still an oblique impact test, the material of interest serves as the angled impactor with the target consisting only of an anvil. Anvil materials are held to the same design constraints as the previous experiment, and elastic behavior is assumed. The specimen/impactor is immediately subjected to both (simultaneous) pressure and shear stress loading, with no time separation between wave arrivals [26] [80]. Stresses are inferred from particle velocities measured on the rear free surface using the same methodologies as previously mentioned for CPPSPI. Figure 2-8 shows a schematic and corresponding X-t diagram showing wave propagation in the anvil.

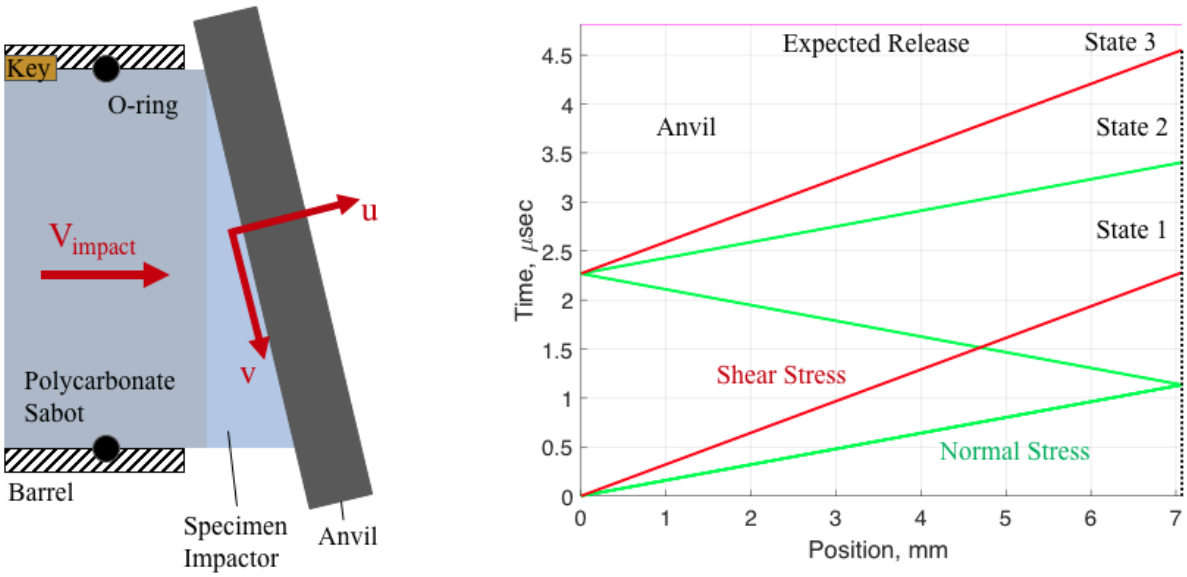

Fig. 2-8. A schematic and X-t plot for a typical dynamic friction impact experiment, consisting of a angled specimen-flyer impacting an anvil target. The specimen is subjected to immediate pressure and shear stress loading, the ratio of which describes the friction behavior of the interface.

The measured stress state is the interface of specimen impact as opposed to propagation through the specimen and so the observed response reflects the traction behavior of the specimen-anvil interface, not the bulk material. This makes the configuration uniquely suited for quantifying friction. As in the classic case, the dry-Coulomb coefficient of friction (COF), termed μ_s (static) or μ_k (kinetic), is defined as the ratio of shear force to the normal confining force, can be defined in terms of measured PSPI values shown in eq 2.26

$$\mu = \frac{V}{N} = \frac{VA_0}{NA_0} = \frac{\tau}{\sigma} = \frac{C_L u_{fs}}{C_S v_{fs}} \tag{2.26}$$

where V and N are the shearing and confining force, A_0 is area of loading which in this case is the same for both forces, τ and σ are the shear and normal stress inferred from free surface particle velocities u_{fs} and v_{fs}, after having propagating

through the target anvil with longtitudinal and transverse sounds speeds of C_L and C_S. If interface surfaces are moving with respect to one-another this is kinetic COF (with slip) where $\mu = \mu_k =\mid \frac{\tau}{\sigma} \mid$, otherwise the no-slip condition is assumed true and the COF $\mu = \mu_s$ with $\mu_s >\mid \frac{\tau}{\sigma} \mid$. μ is known to be dependent on parameters such as surface roughness [9] and load pressure [86], both of which may be observed through this technique.

Multiple combined stress states are experienced throughout a given experiment as shown in Figure 2-8. State 1 (σ_1 and τ_1) occurs as the shear stress wave arrives at the back surface representing initial loading on impact. The longitudinal wave releases after reaching the back surface and reflects back releasing the impact surface to about $\frac{1}{3}$ of the initial normal stress resulting in State 2 (σ_2 and τ_1, where $\sigma_2 \approx 0.33\sigma_1$ [80]). Depending on experiment duration, a State 3 can also be seen after partial shear release (σ_2 and τ_2). Together, each test may provide two or more measurements of μ for a given tribological pair at multiple confining pressures.

Dynamic friction experiments are kinematically distinct as they experience pressure **and** shear (as opposed to pressure **then** shear). Deformation is governed by a single set of equations (eqs. 2.27) beginning on impact,

$$x_1 = \lambda(t)X_1,\ x_2 = X_2 - \kappa(t)X_1,\ x_3 = X_3 \tag{2.27}$$

Notation, is has been maintained where λ and κ are proportionality constants for compression (”stretch”) and shearing related to either longitudinal or transverse strains. These result in very different deformation (**F**) and rate of deformation (**D**) tensors eqs 2.28 and 2.29 [73].

$$F = \begin{bmatrix} \lambda & 0 & 0 \\ -\kappa & 1 & 0 \\ 0 & 0 & 1 \end{bmatrix} \tag{2.28}$$

$$D = \frac{1}{2}\begin{bmatrix} 2\frac{\dot{\lambda}}{\lambda} & \frac{-\dot{\kappa}}{\lambda} & 0 \\ \frac{-\dot{\kappa}}{\lambda} & 0 & 0 \\ 0 & 0 & 0 \end{bmatrix} \tag{2.29}$$

The dilatations for both oblique impact experiments discussed are equivalent to the Jacobian, $J = det(\mathbf{F}) = \lambda$, meaning both experience the same volumetric change. Given the shearing portion of loading is an ischoric process, CPPSPI and dynamic friction are equivalent in thermodynamic space. However, the specimen may experience plastic deformation and the related irreversibilities associated with permanent failure, friction, and heat generation (all inter-related) making them distinct.

2.3 Mechanical Behavior of Polymers

The provided theoretical framework up to this point has been kept general, with comments being applicable to any generic "specimen" of interest undergoing an impact event. Now the purview is narrowed, only considering polymers like those selected for this study (polyurethane and epoxy) - specifically the characterization of their dynamic response undergoing pressure-shear stress loading. This requires additional polymer-specific phenomenological considerations to be made, particularly concerning friction, adhesion, and high strain-rate visco-elastic behavior. Friction and adhesion are linked and will be discussed together under the archetype of polymer surface or contact physics. These have significant implications on how stresses (surface tractions) transmit through an interface. Visco-elastic/plastic phenomena introduce time dependent deviations in impact response from traditional Hugoniot trends.

Surface Physics

First consider surface interactions, where two arbitrary surfaces are confined together, with one being a polymer and the other being a hard (metal) substrate. If these were infinitely *flat* with no roughness, then the entire surface area of each would be in contact with the other. No material is infinitely flat, instead material contact occurs on the level of surface roughness asperities either interlocking, akin to gear teeth, or peak-to-peak. This is shown schematically in Figure 2-9. At individual points of contact, approximately nanometers in diameter, very high areas of stress concentration develop at even very small confining pressures resulting in bonded material welds. Chemical bonding on an atomic level may also occur depending on surface energies. Both contributions define surface *adhesion* [9].

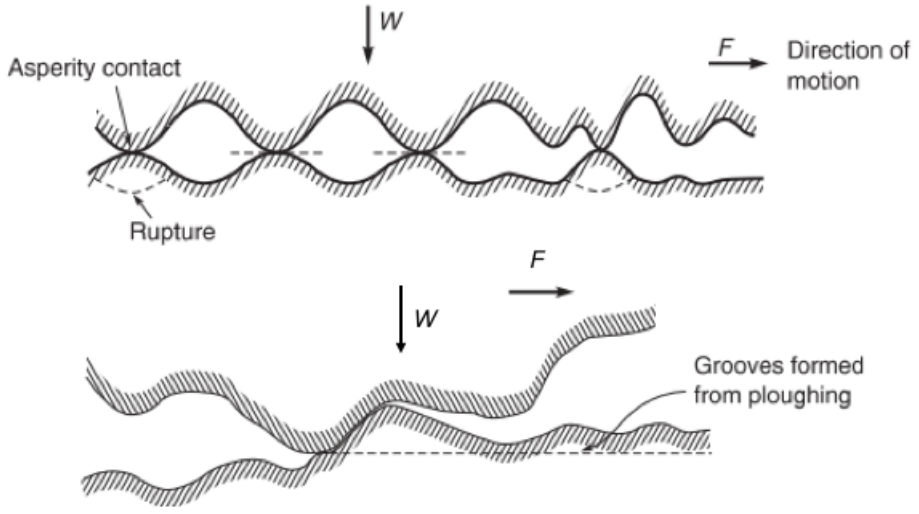

Fig. 2-9. Example of ”rough” solid-solid surface contact through asperities, from [9].

When subjected to shear, two types of failure may occur either at the point of asperity bonding (adhesion failure on the micro-scale) or the harder surface asperities break into the softer material resulting in *ploughing* (material failure on the macro-scale). Because of these distinct failure modes, strength becomes critically relevant and is also dual in nature. Either the softer polymer material fails in which bulk material strength governs behavior, or the physio-chemical adhesion bond between polymer and substrate fails. Shear strength in polymers in contact is known to be dependent on load pressure, and takes the general linear form shown in Eq. 2.30.

$$\tau = \tau_0 + \alpha P \tag{2.30}$$

where τ_0 is the initial material shear strength under no pressure, P is the confining pressure, and α is the change in strength with increasing compression [6, 9, 21, 89]. Separating the contribution of bulk material strength from that of adhesion is not well understood, with the latter being very dependent on surface roughness (i.e. asperity contact) as well as surface energy leading to chemical bonding. Through experiment with thin-film solid lubricants, it has been established that adhesive strength cannot greatly exceed that of the softer material itself. If this were the case, the softer material would yield near the spot of adhesion and no bond would form at all. These same experiments have shown little deviation in τ due to which polymer-bonded substrate used as long as it was of higher strength (metals). While conclusions around these observations are clearly approximate, it is pragmatic to consider the interface (adhesion) strength to be empirically equal to the bulk polymer shear strength [9, 86, 89].

With shear behavior defined, friction is the ratio of shear to the confining pressure. Dependence on pressure is carried through embedded in shear stress

giving the relation Eq. 2.31

$$\mu = \frac{\tau_0}{P} + \alpha \tag{2.31}$$

For polymers at high confinement, shear is a significantly low in magnitude meaning the ratio $\frac{\tau}{P} \to 0$ which results in an asymptotic approach to some constant α. Experiments at both low and high strain-rate have observed this to be $\alpha \approx 0.2$ [9] [21]; with variation due to the orientation of polymer processing. Notably, this formulation is akin to the Mohr-Coulomb yield surface formulation which originally used this concept setting bulk shear strength as a function of compression and internal cohesion [74].

Impact Viscoelasticity

Turning from the interaction of surfaces to the bulk material response, the review of literature has already provided significant evidence and observation of the nonlinear transience of polymer response to mechanical loading [17] [43]. This extends to high strain-rate loading during uniaxial impact experimentation. In comparison to more traditional homogeneous isotropic materials, there is an apparent absence of an elastic-precursor, inferring no observable Hugoniot elastic limit. There is still a yield strength of course, which has been measured by Bourne for several polymers [67] undergoing uniaxial impact, however the distinct propagation of an elastic then plastic waves is not present (i.e. no two-wave structure). In place of this, there is a characteristic tendency for polymers to show an initial (steep) rise in stress/particle-velocity to about $\frac{2}{3}$ of the expected Hugoniot, before rounding and gradually attaining a final equilibrium state [64]. This was first discussed by Barker and Hollenbach, [10], and their plot is shown alongside a labeled example particle velocity history in Fig. 2-10.

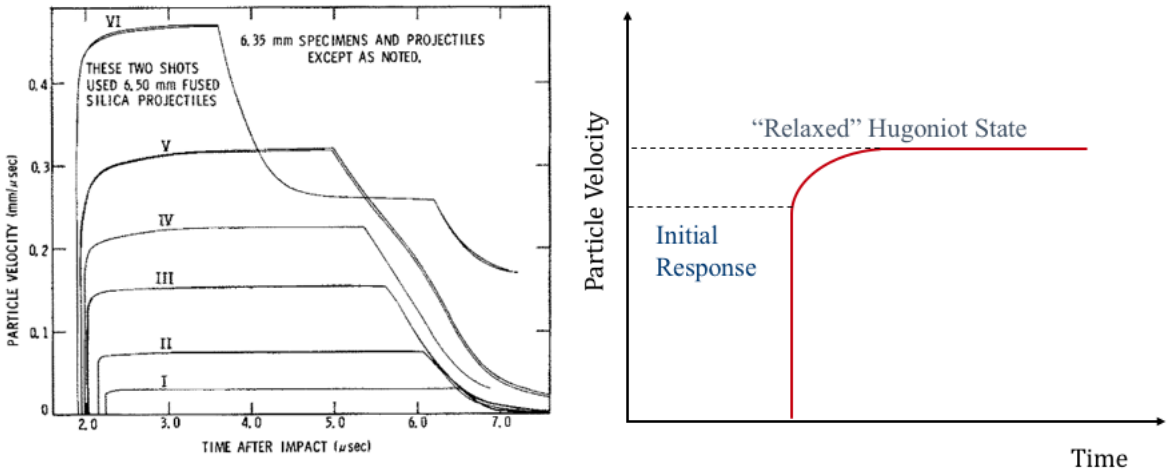

Fig. 2-10. Experimental particle velocities of polymer response to shock [10] alongside an idealized plot showing the initial rise followed by hypothesized relaxation/viscous dispersion.

Mechanically, as a stress wave propagates through the target, and the polymer-chains compress, bend, and flex with respect to one another. Unless the shock is strong and over-driven, regardless of elastic-plastic conditions, this introduces an additional characteristic time as chains prevent each from the otherwise immediate response seen in crystalline materials. Posed another way, chain entanglement slows the physical time it takes to achieve a new equilbrium state, a state which itself is varying as the reference material structure has now changed. This is termed relaxation in low-rate experiments where a constant strain condition results in *gradual* release in stress. Similar interactions are occuring even under impact conditions, with ”relaxation” in stress increasing the observed particle velocity. Mathematically this has was first modeled by Schuler [105] who considered in the repercussions in Hugoniot space, shown in Figure 2-11. Hugoniot equilibrium is modeled as a literal shift into a different material Hugoniot due to the change in chain-arrangement.

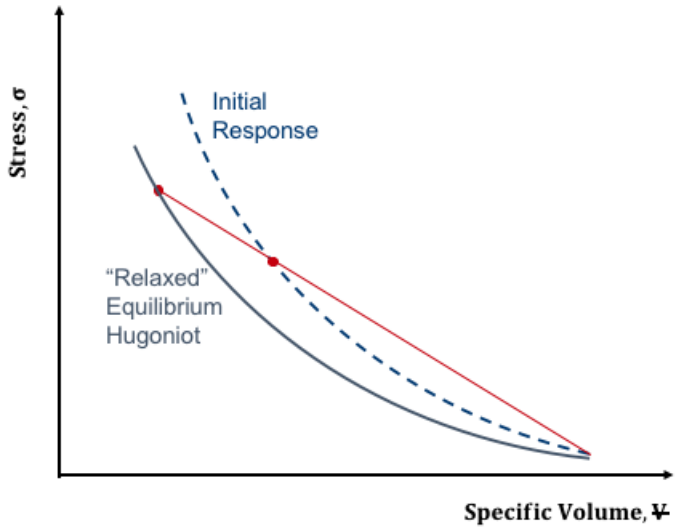

Fig. 2-11. Relaxation of a polymer during uniaxial impact shown in Hugoniot P-v space.

Assuming this mechanism, it is intuitive that orientation of chains within a polymers would have large implications on the dynamic response just as in static or low-rate cases. This is expected to be particularly true for unordered amorphous polymers, which may vary greatly depending on processing/mold. It is even further complicated by the slight variations in (often proprietary) chemical composition used by different manufacturers. To that end, the epoxy and polyurethane (both 2-part resin) systems used in this study are characterized via uniaxial impact and quasi-static shear testing prior to any pressure-shear testing to capture variations from previous formulations studied.

Strength and Viscoplastic Modeling

To examine strength behavior in polymers, first consider the general Cauchy stress tensor σ_{ij} where $i, j = 1, 2, 3$. It is convenient to express the three dimensional stress in a single von-Mises effective stress term defined as Eq. 2.32

$$\sigma_{eff}^2 = 3J_2 = \frac{1}{2}[(\sigma_{11} - \sigma_{22})^2 + (\sigma_{22} - \sigma_{33})^2 + (\sigma_{33} - \sigma_{11})^2] + 3[\sigma_{12}^2 + \sigma_{13}^2 + \sigma_{23}^2] \tag{2.32}$$

J_2 is the second material invariant of the deviatoric portion of Cauchy stress, each σ_{ij} where $i = j$ is a Cauchy stress component along the tensor trace, while each σ_{ij} where $i \neq j$ is deviatoric shear stress. Strength of a material is generally then defined as maximum effective stress attainable prior to yielding. Several theories have been posed expressing the functionality of this yield *surface* which often vary between material groups. Among the most common, von-Mises assumes a constant yield strength value with no dependencies. This criterion is expressed very simply as Eq. 2.33, with a yield strength value κ [20].

$$\sigma_{eff} < \kappa \tag{2.33}$$

This is quite accurate for many materials, particularly metals, however many materials exhibit varying yield strength depending on pre-conditions. As previously noted in the discussion on friction, polymers have been experimentally found to have increased strength at increasing pressure. Such behavior is modeled well be the Drucker-Prager criterion [58] [59], which in its most simple form is Eq. 2.34.

$$\sqrt{J_2} < Y_0 + \alpha I_1, \textit{ where } \sqrt{J_2} = \frac{\sigma_{eff}}{\sqrt{3}} \tag{2.34}$$

Y_0 is the yield strength with no confining pressure, $I_1 = trace(\sigma_{ij}) = \sigma_{ii}$ is the first material invariant of Cauchy stress, and α is the rate of change of strength with respect to I_1. Depending on notation a common formulation is in terms of mechanical pressure recalling that $P = \frac{1}{3}trace(\sigma_{ij})$. Figure 2-12 compares the Drucker-Prager and von-Mises yield surfaces.

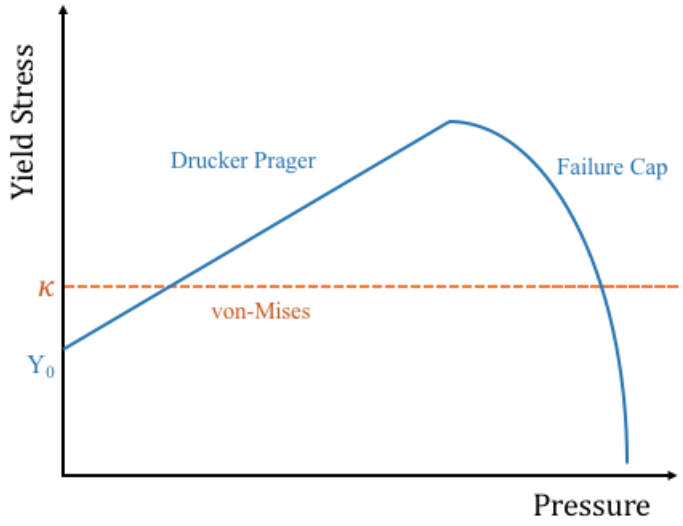

Fig. 2-12. A representative comparison of von-Mises and Drucker-Prager yield surfaces in strength-pressure space. The base version of Drucker-Prager would allow yield strength to increase indefinitely, however this is known to be false and at some pressure all bulk strength will give way to hydrodynamic behavior. This transition is often modeled by a failure "cap" as shown.

A significant flaw in eq. 2.34 is the implication that strength may infinitely increase alongside I_1, which is not physically likely. Increasing compression in polymers encourages greater entanglement and interaction between polymer-chains, which is hypothesized as the mechanism behind strengthening. This eventually reaches some limit related to the maximum theoretical molecular density, at which point hydrostatic pressure alone will exceed strength and the polymer equation-of-state will govern material response, up to and include phase change (like melt).

The presented inequalities have addressed only the threshold at which a material will yield, and not behavior after yielding. This regime is known as viscoplasticity, and resulting models attempt to predictive residual strength during plastic flow. These are more complicated in general and incorporate phenomena such as strain, strain-rate, temperature, and work hardening dependence. Flow models vary from first principles based models grounded in dislocation mechan-

ics [106] to those entirely based on empirical parameters. One formulation, of the latter type, is the Johnson-Cook constitutive model shown in Eq. 2.35 [107].

$$\sigma_y(\epsilon, \dot{\epsilon}, T) = [A + B\epsilon^n][1 + Cln(\frac{\dot{\epsilon}}{\dot{\epsilon_0}})][1 - (T^*)^m] \tag{2.35}$$

Flow stress σ_y is a function of strain ϵ, strain-rate $\dot{\epsilon}$, and temperature with respect to a melting point T^*. The contribution of each dependency must be tuned from experimental data through the values A, B, C, n, and m. Complete development of such as constitutive model for polyurethane and epoxy was not an objective the current study, but the use of such a model for simulation was required.

CHAPTER 3

CHARACTERIZATION OF SELECTED POLYMERS

3.1 Description of Polyurethane and Epoxy

Polyurethane (PUR) was chosen as a material of interest due, primarily, to its prevalence in applications as either a structural component, coating, or adhesive. It is also relatively easy to acquire and has a substantial library of data available from other mechanical characterization studies. Specifically, the tested polyurethane was 1512 two-part liquid plastic purchased from *Polytek*. Relevant mechanical properties include a mix viscosity of 400 cP, a shrinkage of about $5x10^{-3}$ in/in, a quasi-static tensile yield strength of approximately 46 MPa after 24 hours of curing, with a shore hardness of 71D. A 20-minute pot life window was available for mixing and molding, with color after curing being an opaque white. Mixing was one-to-one by weight.

Epoxy, selected based on the same motivations, was AA-Bond F110 epoxy adhesive purchased from *Atom Adhesives*. Also a two-part compound, F110 has a mix viscosity of 310 cP, listed as ”low” shrinkage with none measurable in practice, a lap (adhesive) shear strength of 14.8 MPa after 24 hours of curing, and a shore hardness of 83D. Pot life was 30 minutes, and the material is transparent upon curing with a slight yellowish hue. Mixing was 100:11 resin-to-hardener by weight.

For both, the presence of air bubbles post-molding were a significant concern and so samples were degassed during pot life with a vacuum less than 29 in-Hg. This was sufficient to remove most bubbles from the mixed polymer with the remainder being crushed by the return of ambient pressure, any potentially remaining microbubbles were considered negligible. Post-mold densities were on

average $1.135^{\pm}0.020$ and $1.155^{\pm}0.020$ g/cc for polyurethane and epoxy respectively. Preliminary characterizations served to establish a baseline for material behavior, and identify potential discrepancies in mechanical properties due to formulation - which was proprietary and not provided by either manufacturer. Tests consisted of sound speed measurements, quasi-static/low-rate shear testing, and traditional Hugoniot measurements using uniaxial impact tests.

3.2 Longitudinal and Transverse Sound Speed

Sound speeds were measured using *Olympus* 5058PR high voltage pulser-reciever, using a through-transmission configuration, with the experimental setup and data processing shown in Figure 3-1. Transducers are placed and aligned on either side of a target of known thickness Δx.

One transducer serves as the pulse transmitter, imparting an acoustic wave into the target, while the other transmitter serves as a pulse reciver. Both transmitted and recieved waveforms are recorded via oscilloscope and differences in wave arrival times result in a Δt value quantifying transit time. Elastic wave speed, C, is then simply decribed by eq. 3.1

$$C = \frac{\Delta x}{\Delta t} \tag{3.1}$$

Depending on the equipped transducers, either longitudinal or transverse waves may be imparted allowing the observation of both normal and shear stress (acoustic) wave speeds. For polyurethane nominal longitudinal and shear wave speeds of 2.30 and 0.99 mm/μs were observed, with an uncertainty of $^{\pm}0.04$ mm/μs. These, in conjunction with an average bulk density 1.135 g/cc, infer elastic longitudinal and shear stress impedances of 2.61 and 1.12 $\frac{g-mm}{cc-\mu s}$. Likewise, epoxy measurements resulted in wave speeds of 2.64 and 1.24 mm/μs (longitudinal and

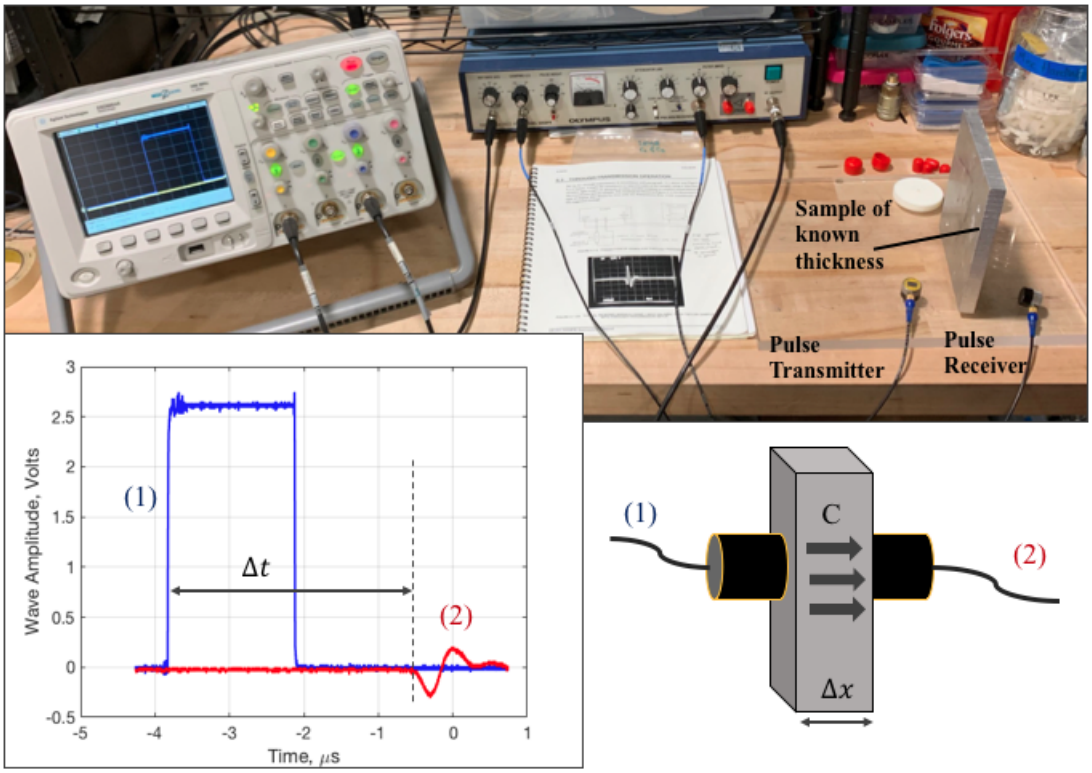

Fig. 3-1. The experimental setup for measuring material sound speeds using the *Olympus* 5058PR. Waveforms from a tested 7.05 mm thick polyurethane sample is shown to demonstrate how transit time is measured.

shear) respectively with impedances of 3.05 and 1.43 $\frac{g-mm}{cc-\mu s}$ - which suggests that epoxy would have a *stiffer* mechanical response in general.

3.3 Quasi-static and Low-rate Strength Testing

Quasi-static and low strain-rate shear testing was done according to the ASTM-D143 standard [108]. Specifications called for a stair-step block of material, shown in Figure 3-2. Samples are constrained such that when sheared, loading was isolated to a single plane. Deformation was facilitated using an MTS machine. Two variations were conducted with tests performed on either the bulk polymer (epoxy or PUR) material, or on a thin-film molded between 7075-T6 aluminum surfaces.

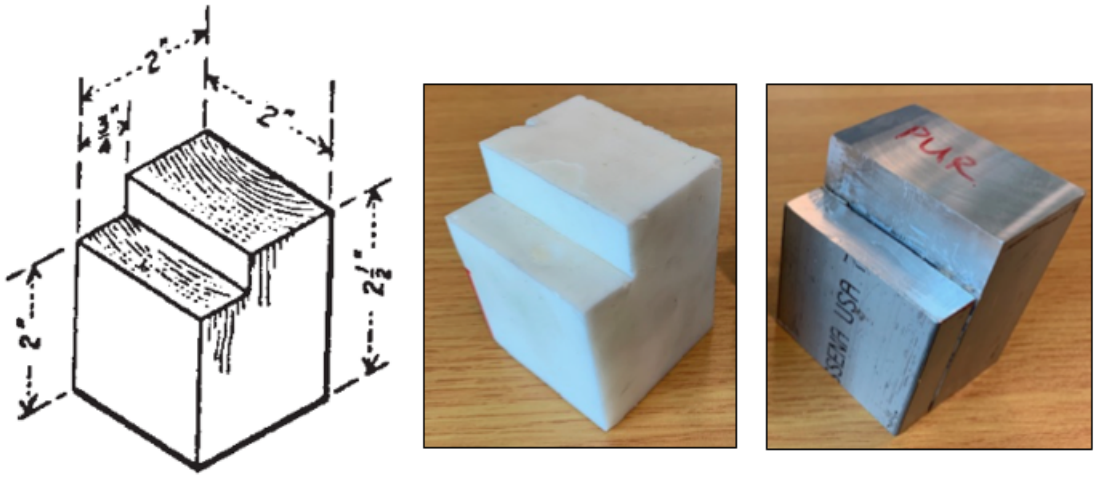

Fig. 3-2. Sample specification required by the ASTM-D143 shear test, shown alongside manufactured polyurethane specimens for both the bulk material and thin film configurations.

Testing of the thin-film strength is akin to standard lap-shear tests used to evaluate adhesive strength (ASTM D5868). These were conducted to better mimic the high strain-rate oblique impact experiments, discussed later, which consists of thin polymer targets molded between two 7075-T6 aluminum anvils.

An experimental schematic demonstrating loading is shown alongside stress-strain results for PUR in Figure 3-3. Specimens were sheared at three different speeds 0.042 mm/s (quasi-static), 0.42 mm/s, and 25.4 mm/s which equate to shearing strain-rates of 10^{-3}, 10^{-2}, and $10^{0}s^{-1}$. Each showed a distinct stress curve with ultimate shear stresses of 18, 23, and 25 MPa with 0.5 percent uncertainty (from the manufacturer). The dashed curve shows thin-film results strained at a rate of $10^{0}s^{-1}$, which indicates a comparable ultimate strength of 25 MPa.

Variation due to slight differences in pre-loading (less than 1 MPa) have been corrected to reflect comparable initial strain. The observed strengthening behavior corresponds well other studies conducted over similar strain-rate ranges using both MTS tension-compression and Split Hopkinson-bar test. These saw an

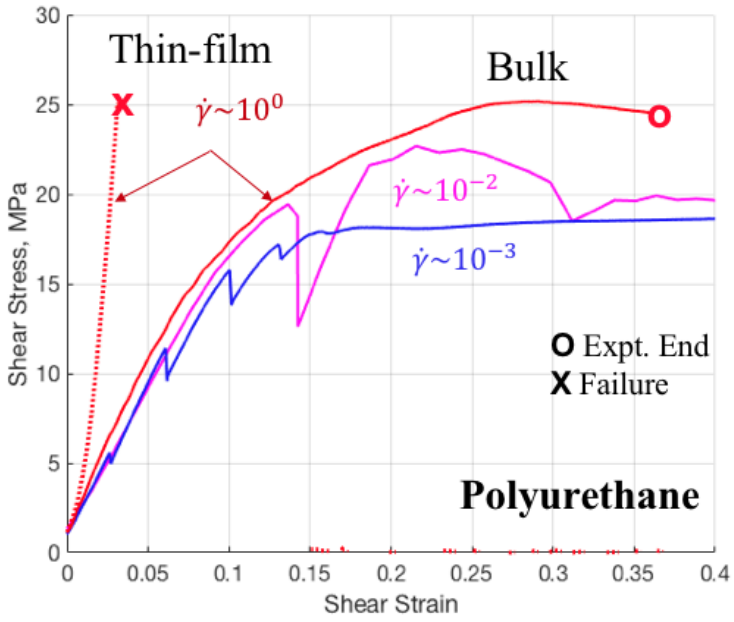

Fig. 3-3. Polyurethane response shown in engineering shear stress - engineering shear strain space. Slight strain-rate dependence is observable as well as drops in stress throughout loading indicative of polymer-chain relaxation. The dashed profile represents the thin film experiment conducted at the fastest rate, which shows comparable strength but with a large increase in modulus. Results are shown alongside a schematic demonstrating loading conditions.

increase of only a few MPa in shear strength from 10^{-3} to $10^{1}s^{-1}$ after which point the rate strengthening becomes more dominant and strength was seen to double between strain-rates of 10^{2} to $10^{4}s^{-1}$ [109] [92]. However, it is important to note experiments at higher strain-rates were also done at higher pressures.

Note the lower-rate load histories exhibit stair-step drops in stress during straining. This type of behavior has been seen previously in other studies [110] and is indicative of relaxation within the polyurethane polymer-chains. Time-dependent in nature, as strain-rate increases it would be expected that the phenomena would become less and less apparent. This is reflected in these results as drops become less in frequency with increasing rate.

Recall shear modulus G, defined as the ratio of shear stress to shear strain during elastic loading ($G = \frac{\Delta\tau}{\Delta\gamma}$). For bulk polyurethane specimens these values saw only a slight increase varying from 165, 169, and 199 MPa over the tested rates. All were significantly lower than the 654 MPa modulus seen in the adhesive case, more reminiscent of brittle polymer behavior - albeit resulting in the same overall ultimate strength. This is intuitive when one considers the interlinking nature of the polymer network. Just as the interaction of chains allows for the relaxation of stress within the material, constraining that network to a thin film would be expected to reduce overall material toughness, block the dissipation of stress to other linking molecules and more immediately relying to *pure* material response. This is readily visualized when bulk specimens are examined post-mortem as shown in Figure 3-4. By inspection, the influence of shear extends well into the specimen.

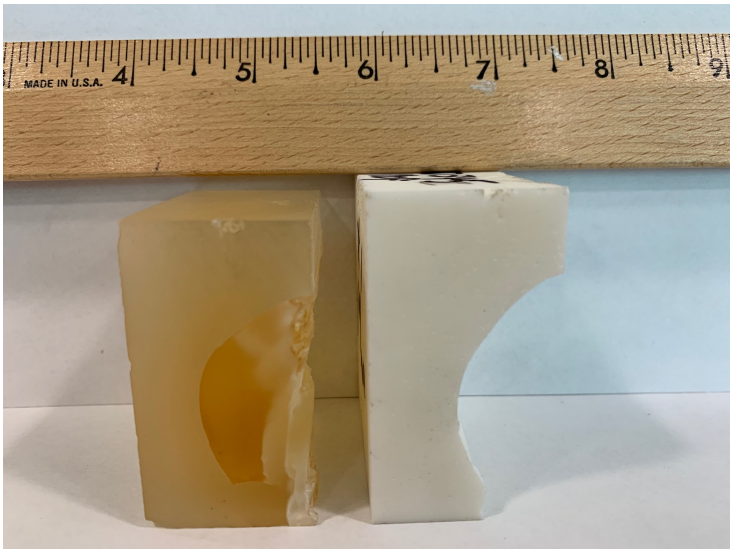

Fig. 3-4. Post-mortem epoxy (left) and polyurethane (right) specimens subjected to shear via the ASTM-D143 standard. Samples are constrained such that the shear plane should be limited to the face of the stair-step, however the amorphous network of polymer-chains allows for the dissipation of shear stress well into the bulk material, increasing material toughness. Ruler units are inches.

Similar testing was performed on epoxy samples, shown in Figure 3-5. Note only one strain-rate ($10^0 s^{-1}$) was explored. This was in an effort to conserve material for impact experimentation and considered sufficient given other literature data demonstrating strain-rate dependence with trends similar to that of polyurethane [66]. Both responses show an ultimate shear strength of near 31 MPa, with variation between the two within the reported uncertainty of 0.5 percent. Calculated shear modulus values were distinct by an order of magnitude being 183 and 1393 MPa respectively. While the difference is much greater, the trend is consistent with polyurethane - and is hypothesized to be facilitated by the same chain interaction mechanisms.

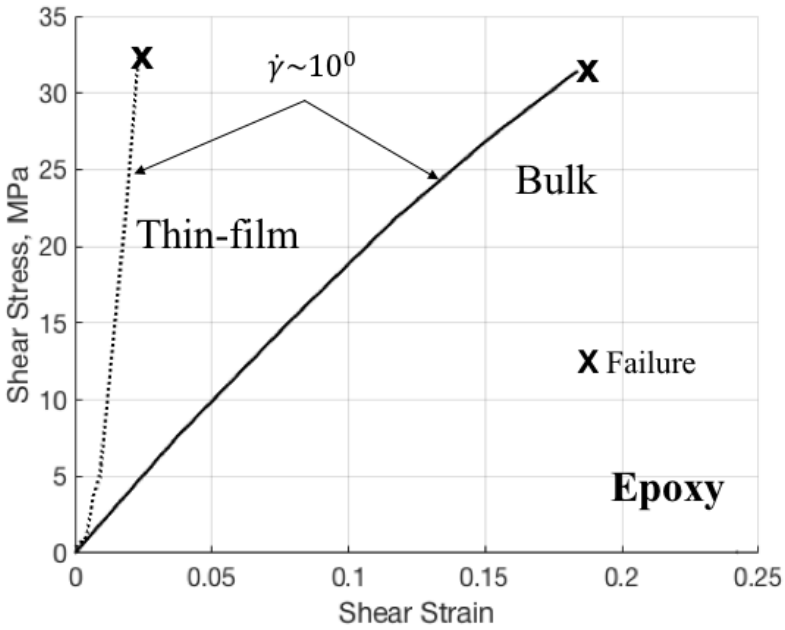

Fig. 3-5. Epoxy response shown in engineering shear stress - engineering shear strain space.

3.4 Polymer Hugoniots

Higher strain-rate characterization consisted of plane-strain unaxial impact experiments in order to measure a Hugoniot for each polymer. Tests were conducted at the Air Force Research Laboratory's High-Pressure Particulate Physics (HP3) facility located on Eglin AFB. A 101.6mm (4") bore wrap-around and 60mm bore powder gun were utilized, depending on desired speed, to produce impact velocities of up to 1200 m/s. In all cases, polymer targets were nominally 5mm in thickness, 46mm in diameter, and were backed by a poly-methylmethacrylate (PMMA) 12.7mm thick transparent window, 42.7mm in diameter. The setup is shown in Figure 3-6.

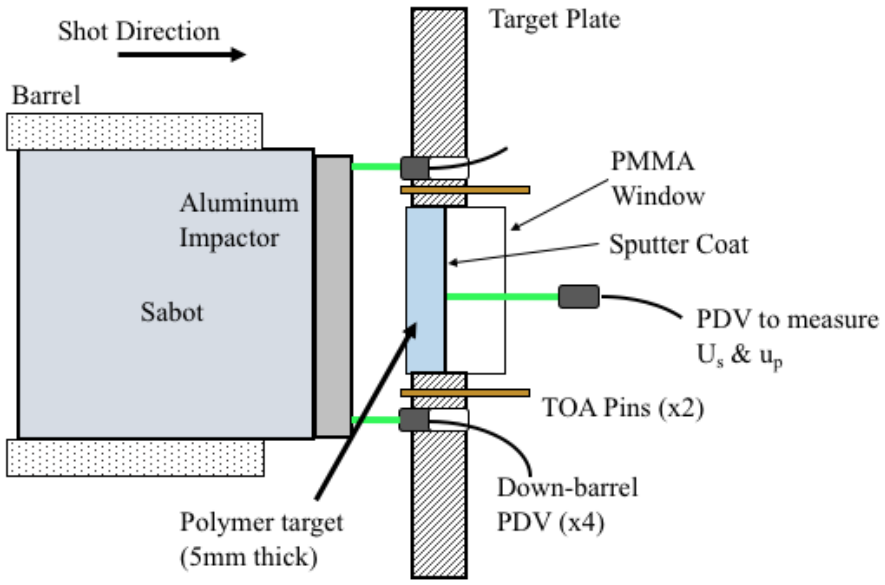

Fig. 3-6. Experimental setup for Hugoniot shots done at HP3. Multiple 5 mm polyurethane targets, confined by a PMMA window, were impacted at velocities up to 1200 m/s. Measured values include particle velocity from PDV and shock velocity inferred from wave arrival times.

Each polymer specimen was embedded within a target plate so as to be compatible to mount and align within the HP3 target fixture. Time-of-arrival (TOA) measurment and diagnostic triggering was achieved using two *Dynasen* make (closure) pins, concentrically set on opposite sides of the polymer face within the target plate. Impact velocity and tilt were measured using four down-barrel PDV collimators (probes). The PMMA window transmits 1550 nm light, and as such PDV diagnostics aligned to the back surface could measure particle velocity at the PMMA-polymer interface, which was sputter coated with aluminum to facilitate better light return (signal power). All shots were done under vacuum conditions not exceeding 200 mtorr.

Polyurethane

The observed Hugoniot for Polytek 1512 polyurethane is plotted in both $U_s - u_p$ and $\sigma_{11} - \rho$ space, shown in Figure3-7. Data is plotted alongside similar studies done by Los Alamos National Laboratory (LANL) [111] and Appleby-Thomas in 2011 [112] for contrast. The LANL study is most directly comparable, as the material was another fully dense polyurethane, while the included results from Appleby-Thomas and coauthors investigated the behavior of a PUR resin modified with nano-particles. Overall, results indicate the polyurethane of interest in this study has similar dynamic pressure behavior to others explored previously.

Upon inspection, immediate attention is drawn to the nonlinear behavior seen below particle velocities of approximately 0.15 mm/μs. As mentioned by Appleby-Thomas [112], this is attributed to the nonlinear elastic-plastic transition with unknown contributions possibly caused to cross-linking or volatile changes in material moduli, none of which are overdriven at such low impact pressures (shock velocities). Despite the underlying being unknown, the behavior is consistent and is also seen in PMMA and polychloroprene [69] [61].

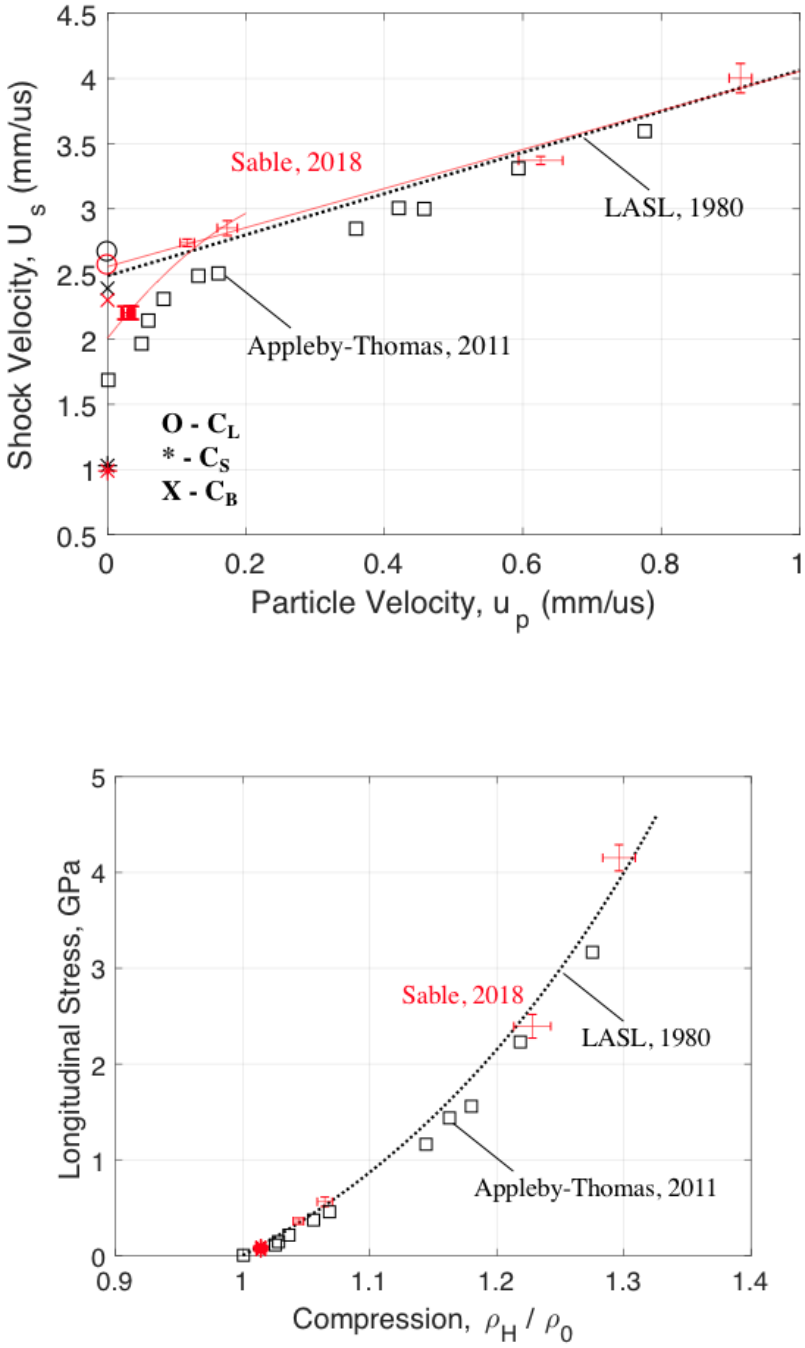

Fig. 3-7. The experimental Hugoniot for Polytek 1512 fully-dense polyurethane, compared against other literature data.

It should be noted that no uniaxial impact experiments were conducted below 150 m/s. The plotted data was taken from initial stresses seen in constant-

pressure pressure shear plate impact experiments conducted later. While oblique impact results are detailed in following sections, recall from *Theory* that prior to shear stress wave arrival, the target is subjected to a series of longitudinal stresses during reverberation. Only the first of these pressure states is located on the polymer's *reference* Hugoniot, with the rest being re-shocks with difference initial states. When plotted, as shown in Figure 3-7, these provide a foothold to examine the Hugoniot (or near Hugoniot) at low pressures and in this case suggest similar nonlinear viscoelasticity/viscoplasticity.

Quantifying these observations, two Hugoniot equations are needed to fit each regime of behavior. First, the more classical regime, is fit as a single line with only a slope and intercept term considered valid for particle velocities between 0.15 and ≈ 1 mm/μs based on current testing shown by eq. 3.2. The fit intercept was calculated to be 2.557 mm/μs by regression, however this was a very close approximate to the bulk sound speed ($C_B = 2.568$ mm/μs) and as such the intercept was replaced in favor of the more physical value.

$$U_s = 1.498u_p + 2.568, \;\; u_p > 0.15\, mm/\mu s \tag{3.2}$$

This agrees well with LANL data ($U_s = 1.577u_p + 2.486$), and so it is reasonable to assume the equation is valid up to the tested range of that study, extending the applicable regime to ≈ 5 mm/μs. Concerning the nonlinear regime below 0.15 mm/μs, there is less published data for comparison. A second order polynomial fit is assumed sufficient resulting in eq. 3.3.

$$U_s = -9.72{u_p}^2 + 6.7356u_p + 2.077, \;\; u_p < 0.15\, mm/\mu s \tag{3.3}$$

The inclusion of this "viscoelastic" Hugoniot relationship is particularly important for future modeling endeavors, as eq. 3.3 is more applicable in strain-rate and

pressure regime explored by oblique impact experiments.

Epoxy

Figure 3-8 shows the measured Hugoniot for Atom Adhesives F110 epoxy, plotted again in both $U_s - u_p$ and $\sigma_{11} - \rho$ space. Also plotted are Hugoniot equations found by Munson [113] and Wood [114] investigating multiple variations of epoxy resins. F110 data agrees well overall with others seen in literature, particular LANL and Munson data. The nonlinear trend seen at low velocities is consistent with both other resin data (Wood) and other polymers such as the PUR data obtained in this study. There is a notable descrepancy between the second order polynomial fit (which includes the nonlinear viscoplastic region) and other epoxy data around 0.6 mm/us particle velocity. Comparing linear fits alone there is an apparent increased stiffness at lower particle velocity. This is somewhat expected, however, given the presence of a hardener compound.

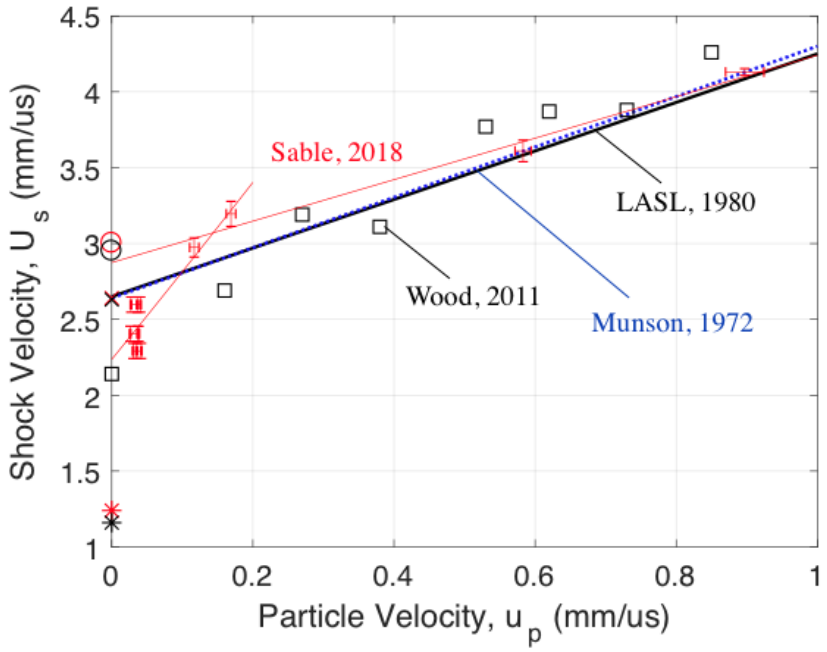

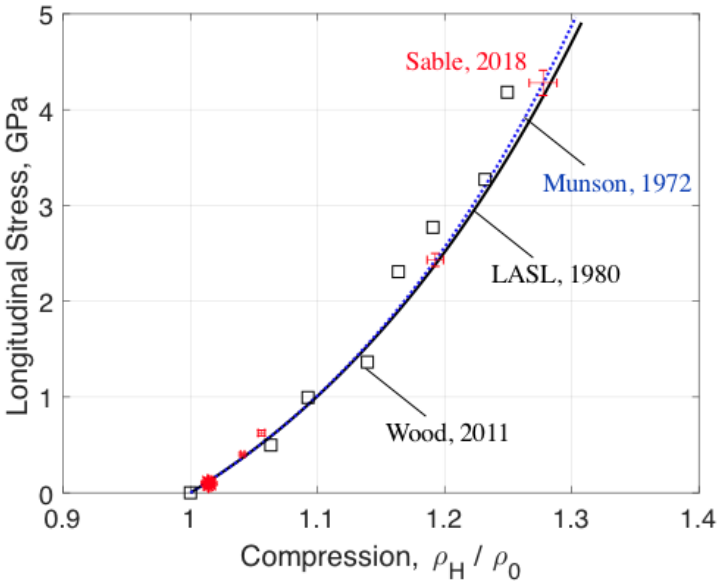

Fig. 3-8. The experimental Hugoniot for F110 two-part epoxy compared against literature data for several epoxy resins.

Again, two equations are used to quantify the two distinct behaviors seen over the tested range. The linear range, with suggested applicability at particle velocities in excess of 0.17 mm/μs is calculated through regression to be eq. 3.4, with the nonlinear regime better captured by the polynomial eq. 3.5.

$$U_s = 1.367u_p + 2.874, \;\; u_p > 0.17\, mm/\mu s \tag{3.4}$$

$$U_s = 0.597{u_p}^2 + 5.7135u_p + 2.236, \;\; u_p < 0.17\, mm/\mu s \tag{3.5}$$

CHAPTER 4

YIELD STRENGTH BEHAVIORS OF OBLIQUELY IMPACTED POLYMERS

4.1 Introduction

Initial experiments sought to evaluate the yield strength behavior of polymers during impact, including their relevant dependencies such as pressure (normal stress) and strain-rate. Specific interest was placed on observing non-Hugoniot conditions through oblique impact. The constant-pressure pressure-shear configuration of the oblique impact experiment (described in this chapter) was used to subject the previously described polyurethane and epoxy specimens to stresses not exceeding 800 and 120 MPa of normal and shear stress respectively, at strain-rates on the order of $10^5 s^{-1}$. Polymers were molded between 7075-T6 aluminum anvils and impacted by an angled projectile consisting of the same alloy. Particle velocity histories observed off the rear free surface were used to infer both the complete combined stress state, any yield behavior, and the nominal strain-rate of deformation. It should be noted that some details have been left to the previous background/theory sections, or adjoining appendices. Specifically, greater detail concerning target design (CAD), target alignment techniques, and diagnostic principles are left to appendices A, B, and C.

4.2 Experimental Methodology

Pressure-shear experiments were performed utilizing both the 50.8 mm bore, slotted barrel, dual-diaphragm gas gun at the Marquette University Shock Physics Laboratory, shown in Figure 4-1, as well as the 63.5 mm bore, slotted barrel wrap-around breech gas gun at the Air Force Research Laboratory's High-Pressure Particulate Physics (HP3) facility at Eglin AFB.

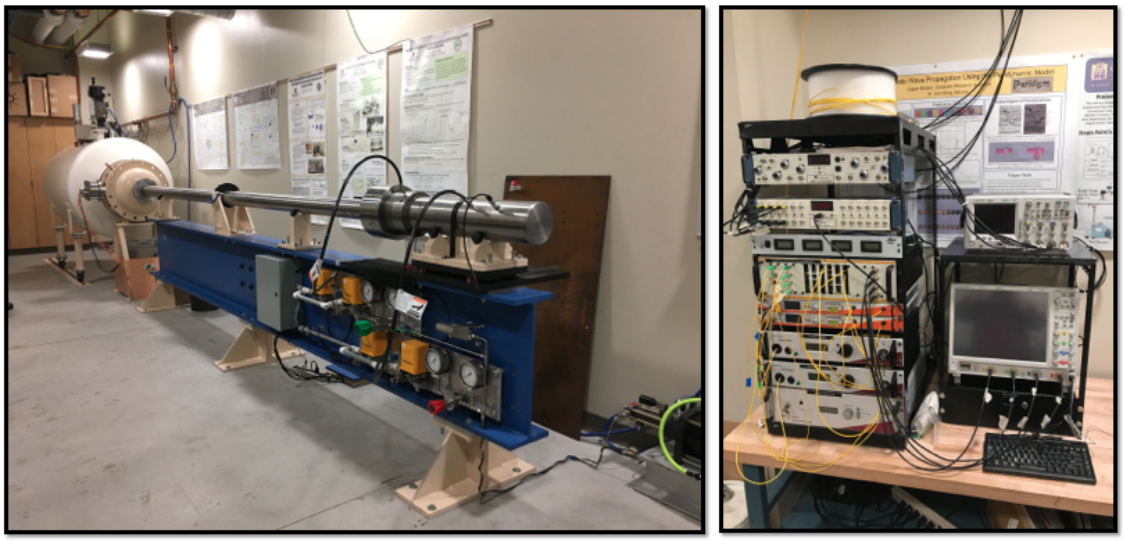

Fig. 4-1. The Marquette University Shock Physics Laboratory, which includes two 50.8 mm bore, smooth or slotted, barrel gas gun operated in a dual diaphragm configuration. Depending on projectile mass and operating gas, impact velocities in excess of 1100 m/s are attainable. The primary diagnostic includes a 4-channel heterodyne photon Doppler velocimeter, with transverse measurement capability, and an implementable 6km delay leg for use in the time-multiplexing of signals.

4.2.1 Overview

The first series of oblique impact tests consisted of the constant-pressure pressure shear plate impact (CPPSPI) experiments wherein an impactor hits a target package consisting of a front anvil, thin polymer sample, and rear anvil. Upon impact, both a normal and shear stress wave are produced and propagate into the target package and impactor respectively. The front anvil thickness is set such that the normal stress wave, traveling at a faster sound speed, arrives at the polymer sample and reverberates between anvils bringing the polymer to an equilibrium normal stress state prior to the arrival of the slower moving shear wave. This ensures the effect of shear loading is temporally distinct from that of normal stress and is more readily distinguished within observed wave profiles. Samples were kept nominally under 0.5 mm, minimizing reverberation time to approximately

a microsecond. After propagating through the polymer, stress waves continued through the rear anvil and their behavior was observed via free surface particle velocity traces measured through traditional and transverse PDV techniques. For convenience, a schematic and X-t diagram are restated from Chapter 2 as Figure 4-2.

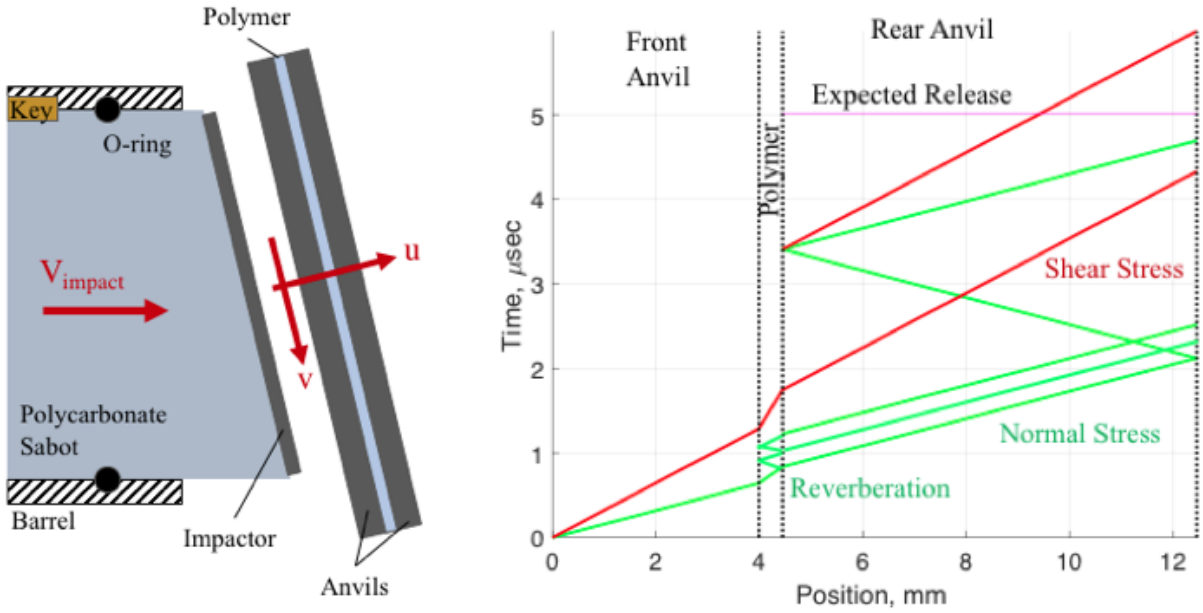

Fig. 4-2. A schematic diagram demonstrating the wave propagation kinematics expected within a constant-pressure pressure-shear plate impact experiment.

Anvil materials and impact conditions were chosen such that the yield strength of all components, except the sample, was never exceeded. This was necessary to ensure only anvils could sustain shear loading and reduces the problem such that one-dimensional elastic wave theory could be applied [13]. This additionally allows the assumption that the normal and shear stress waves do not interact, being perpendicular to one-another – unless in cases of severe skew which is minimized through experimental alignment. Recall eqs. 2.14 and 2.15 stating

$\sigma = \frac{1}{2}(\rho_0 C_L)_R u_{fs}$ and $\tau = \frac{1}{2}(\rho_0 C_s)_R v_{fs}$, govern the relationship between measured free surface particle velocity and the specimen stress state at any point in time. The measurement of both normal and shear stress states results in the characterization of the stress response of the inner target to the imparted loading conditions. If no failure occurs, then the expected magnitude of the shear wave upon reaching the free surface is known. As such, any deficiency in transverse particle velocity from the expected magnitudes infers shear failure of either the internal polymer material or the adhesive bond between aluminum and polymer. Impact angles and velocities are chosen such that no-slip is assumed at the impact surface.

4.2.2 Target Description and Setup

Polymer specimens consisting either of the *Polytek* 1512 liquid plastic polyurethane or the *Atom Adhesives* F110 low viscosity epoxy. For each separate case resin-hardener components were mixed (by weight according to manufacturing specifications), degassed, and then molded between the sandwiched anvils through a molding vent. A thin gasket between the anvils created the interior cavity and helped ensure planarity of the anvils. To ensure proper fill, sound speed pulse-receiver testing was conducted on the target ensuring expected wave transmission. All polymers were allowed *at least* 24 hours to cure, as per manufacturer specifications in order to achieve full strength.

Anvil materials consisted of the previously discussed 7075-T6 aluminum alloy, with a density of 2.792 g/cc and sounds speeds of 6.23 and 3.10 mm/us respectively for the longitudinal and shear wave-types. Anvil surfaces, were of varying surface roughness which was tracked in order evaluate any potential correlation between surface characteristics and shearing behaviors. The surface roughness of anvils was allowed vary between approximately 0.1 and 10 μm (arithmetic mean roughness, Ra-value) in order to investigate any potential relationship between

surface preparation and shear wave transmission at material interfaces. Surfaces referred to as "smooth", were polished to Ra values of approximately 0.5 μm or less. Ra values were measured with a Pocket Surf sapphire stylus profilometer. Roughened surfaces were either milled or roughened with sand paper. Anvil and polymer thickness varied slightly between each shot. Nominally the front anvil was between 4 and 5 mm, the specimen was always less than 0.5 mm, and the rear anvil was between 6 and 7 mm (with one exception at 8 mm). Thickness were selected based on an analysis of sound speed propagation given the necessity of normal stress wave reverberation to a nominal state. Design is further detailed in Appendix A. Table 4-1 shows measured anvil and polymer thickness for each shot.

Table 4-1: Description of relevant target specifications for each shot conducted in the CPPSPI series of experiments. EP and PUR labels signify epoxy or polyurethane targets respectively.

Shot ID	Front Anvil Thickness ($\pm$0.02mm)	Polymer Thickness ($\pm$0.02mm)	Rear Anvil Thickness ($\pm$0.02mm)
EP1	4.81	0.49	6.84
EP2	4.82	0.45	7.05
EP3	4.95	0.45	6.83
EP4	3.99	0.47	6.96
EP5	4.04	0.45	6.95
EP6	3.94	0.50	6.81
EP7	3.81	0.50	6.88
PUR1	4.98	0.43	7.90
PUR2	4.84	0.46	7.03
PUR3	4.87	0.46	7.02
PUR4	4.20	0.46	8.12
PUR5	4.04	0.44	6.95
PUR6	4.06	0.45	6.98

Impactors were guided down the barrel via polycarbonate sabots manufactured in-house at Marquette University. These were 5 inches in length, with a

nominal diameter of 1.988 inches (50.5 mm) just under the bore size, and two O-rings inset on either end to ensure smooth travel down the barrel. Flats, 0.25 inches in width, were milled on corresponding opposite sides of the sabot to allow orientation to be consistently referenced, with a brass key inset onto one side. The key mated with the slotted barrel and ensured projectile orientation was maintained through to impact. Both target assembly and impactor are shown in Figure 4-3.

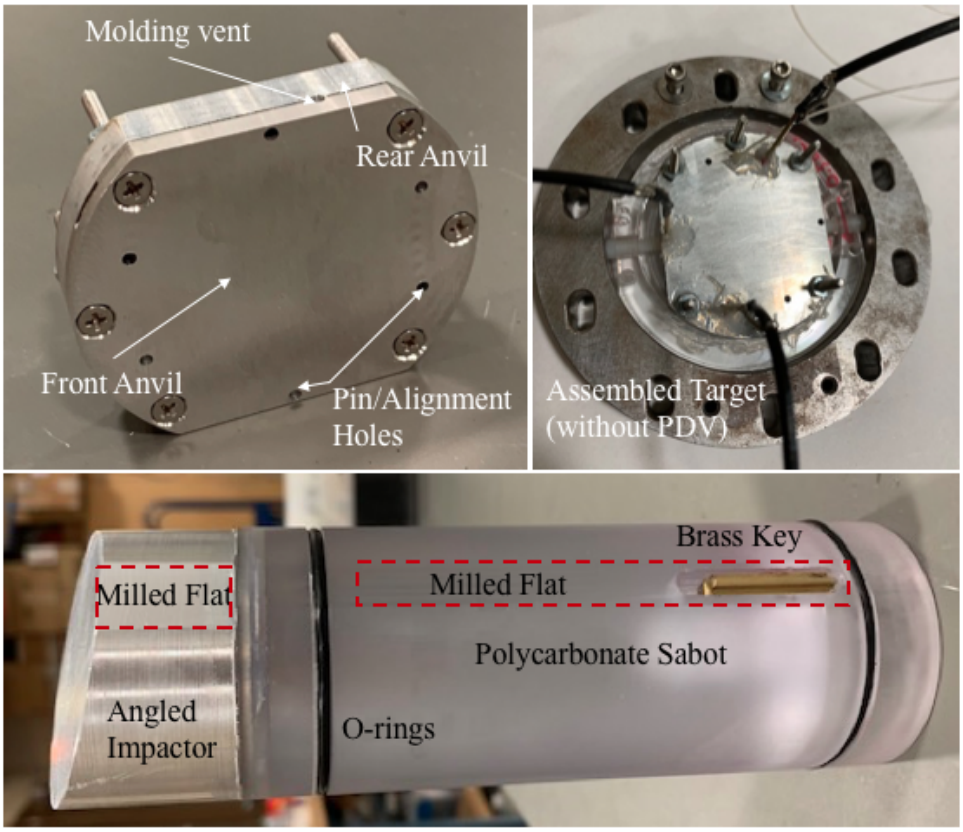

Fig. 4-3. (Top Left) Target assembled prior to polymer molding. (Top Right) Final assembled target placed within a gimbal mount to allow for oblique alignment. (Bottom) A representative projectile including sabot and impactor.

Aligning the target was a multi-step procedure which sequentially ensured that (1) the projectile and target centers were aligned, (2) the target mount plate

was orthogonal to the shot direction, and (3) the angular orientation of the projectile face was planar to that of the target orientation with respect to both the shot direction axis and oblique impact angle. The latter was achieved using a gimbal design. Details of the alignment procedure are available in Appendix B. Impact tilt was quantified and is reported alongside results, with measurements varying between 1 and 15 mrad.

The final portion of setup was the implementation PDV diagnostics. Three collimators (probes) are embedded onto an acrylic bridge affixed to the inner gimbal ring such that emitted laser light may shine onto rear target surface. One probe is aligned perpendicular to the target surface normal while the other two are set at $\pm$20 deg inclines offset from the normal probe on either side shown in Figure 4-4. The apparent velocity measured by PDV is the velocity vector projected onto the light path. This is described by eq. 4.1

$$v^* = \frac{1}{2}V_n cos(\phi) + \frac{1}{2}V_t sin(\phi) \tag{4.1}$$

where v^* is the apparent velocity seen by a PDV collimator emitting and collecting light along its orientated light path with respect to a surface. This normal probe angle ϕ is with respect to the surface normal, and the orientation is assumed to be two-dimensional with any off-axis skew assumed negligible. Any set of normal and angled probes represent two equations, of the form eq. 4.1 with the normal case simplifying to $v^* = V_n$. With the probe orientation known to be 20 deg, transverse velocity is calculable through the solution of simultaneous equations.

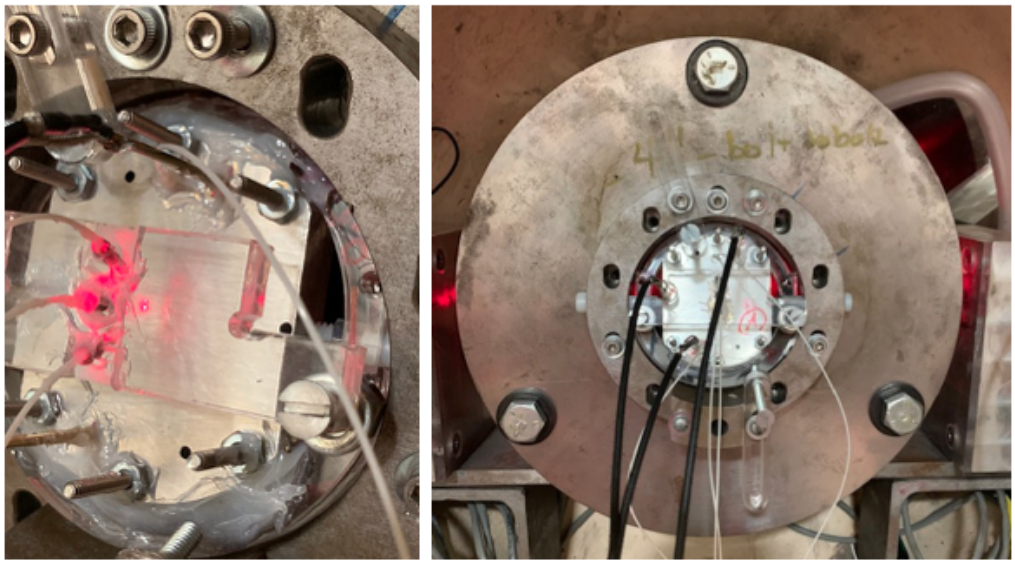

Fig. 4-4. Collimators embedded within a PDV bridge, affixed to the back of a target read for experimentation. The combination of angled and normally orientated probes allows for the normal and transverse velocities to be measured. The gimbal used to facilitate oblique impact can be seen

4.3 Results and Discussion

Thirteen CPPSPI experiments were conducted overall including 6 with fully dense polyurethane and 7 with epoxy. Resulting stress magnitudes were varied by changing either the impact velocity or angle of obliquity. Table 4-2 presents a description of initial impact conditions for each experiment including velocity, angle, stress loading conditions, anvil surface roughnesses, and impact tilt.

4.3.1 Free Surface Velocities

Figure 4-5 shows a typical CPPSPI experiment conducted on epoxy with an impact velocity of 96.7 m/s and a 20 deg angle of obliquity. There are several recognizable characteristics within the particle velocity wave structures, which have been labeled for convenience. First consider the longitudinal (normal) velocity profile, whose arrival time has been arbitrarily set to zero. There is an initial

Table 4-2: Summary of shot conditions for the series of CPPSPI experiments conducted on polyurethane and epoxy. *Actual data unavailable, surface treatment procedure (roughening) was identical to those used in the PUR case and are assumed to be approximately the same values.

Polymer Material	Impact Angle ($\pm$1 deg)	Impact Vel. ($\pm$5 m/s)	Normal/ Shear Load (MPa)	Ra($\pm$0.01 μm)	Impact Tilt(mrad)
PUR	18	98.8	817/132	0.20	8.2
PUR	18	57.8	478/77.3	0.22	9.7
PUR	18	103.5	856/138	8.6	1.0
PUR	18	95.0	786/127	5.5	0.8
PUR	18	101.9	843/137	7.6	1.0
PUR	25	99.5	784/182	0.27	5.9
Epoxy	18	105.8	875/141	9*	4.9
Epoxy	18	105.0	868/140	6*	3.3
Epoxy	18	100.6	832/135	8*	0.5
Epoxy	20	79.0	645/117	0.24	8.3
Epoxy	20	96.7	790/143	0.77	8.6
Epoxy	20	51.8	423/76.7	0.28	7.3
Epoxy	20	66.3	542/98.1	0.62	4.9

rise followed by several incremental steps toward a final state. This is indicative of stress wave reverberation within the polymer specimen between the two aluminum anvils - with each step increasing the normal stress (or pressure) until the front anvil, specimen, and rear anvil have all attained stress equilibrium. The first state of reverberation is particularly useful since it is equivalent to a uniaxial impact state and is on the epoxy Hugoniot. Given the absence of shear, each following state is then on a reshock Hugoniot with a different reference points other than standard temperature and pressure. Calculated shock speeds and particle velocities from this information supplemented previously provided Hugoniot data for both polyurethane and epoxy.

The (expected) final equilibrium velocity value is known based on impact velocity and angle (eq. 2.6), which for the case of Figure 4-5 is expected to be 90.9

m/s. Note the expected arrival times for each reverberation appear slow compared to the experiment profile. Expected times were calculated based on polymer elastic wave speeds, this indicates the speed of wave propagation is increasing with pressure suggesting plastic shock-wave formation and that the normal stress alone is enough to induce some plasticity in the polymer. This has implications on whether the ”pure” yield strength of the polymer is being observed, or rather some residual strength maintained after the onset plasticity.

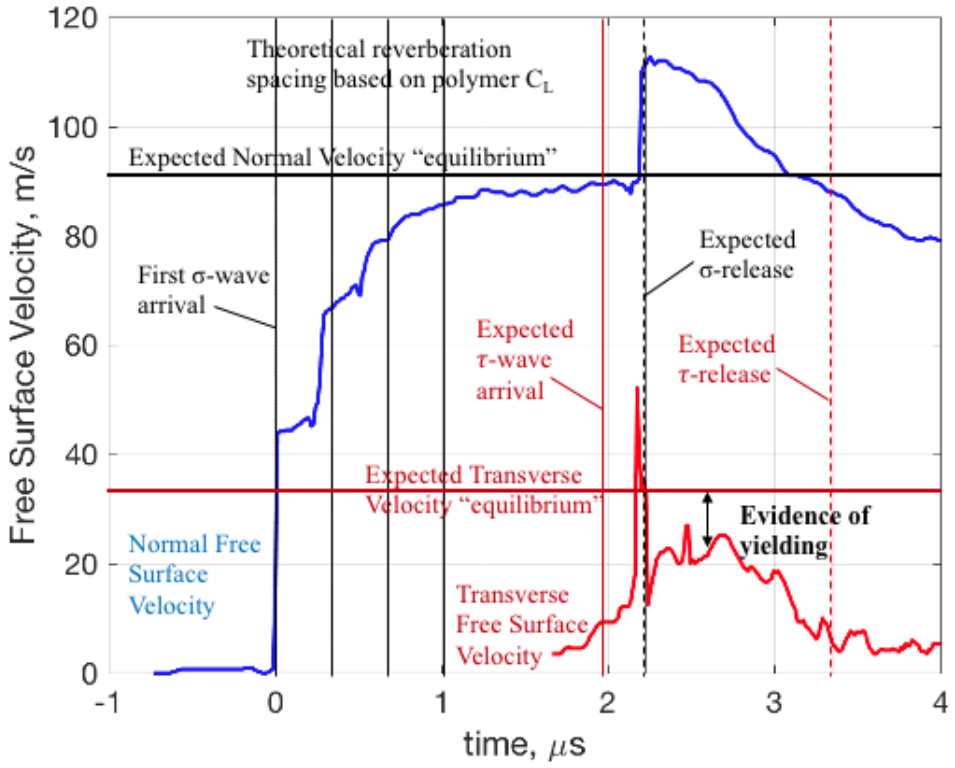

Fig. 4-5. Normal and transverse velocity profiles, processed from PDV, measured off the rear free surface of a CPPSPI target impacted at 96.7 m/s with an oblique angle of 20 deg. Time is arbitrarily set such that time zero coincides with the arrival of the first normal stress wave. Normal stress release is from longitudinal reflections not radial edge boundaries.

Through careful selection of the front anvil thickness, transverse velocity indicative of the shear wave arrives after the polymer as reached near-equilibrium normal stress conditions. Due to tilt concerns, discussed in the next subsection, this arrival was sometimes difficult to identify. Sound speed calculations were used to identify approximately when longitudinal and transverse wave should arrive at the free surface. These approximations were guided the identification of shear windows within the velocity profiles. The expected transverse velocity magnitude was also calculable based on shot conditions (eq. 2.7), with 33 m/s expected for the epoxy example. As can be seen, the trace falls short of this value rising instead to around 20 m/s. This difference suggests that only a shear stress wave corresponding to a transverse velocity of less than 20 m/s (in magnitude) could transmit across the polymer specimen. Under this assumption, that transverse velocity is then a quantification of shear yield strength in the polymer, the calculation of which is discussed in the Inferred Combined Stress States subsection. Overall, each of these discussed behaviors are identifiable in all successful oblique impact results.

4.3.2 Tilt and Timing Considerations

Labeled in Figure 4-5, there is a spike in the transverse velocity profile just after 2 μs. This is associated with a mismatch in timing between normal velocity and angled apparent PDV velocity profiles. Transverse signals are small in magnitude and found by taking the difference of two larger magnitude equations (see eq.4.1). As such, even small discrepancies in relative wave arrival result in large errors particularly around wave arrival. The spike shown in Figure 4-5 is due to the arrival of longitudinal stress release mismatched in time between the two PDV profiles. While this effect is minimized taking into account impact tilt and resulting angled wave propagation in the target [115], the location of the PDV interrogation

site on the surface changes as the surface itself moves and this has not been corrected for at this time. Though shown, spikes such as these have been neglected and assumed erroneous during data analysis.

Impact tilt is important to consider as it results in angled stress wave propagation magnified by the ratio of sound speed to impact velocity [72] [115]. For a two-dimensional case, the angle of wave propagation Φ is calculated from a tilt measurement ϕ through eq. 4.2

$$sin(\Phi) = \frac{C_L}{v_{p,norm}} sin\phi \tag{4.2}$$

for the longitudinal elastic wave case where C_L is longitudinal wave speed as before and $v_{p,norm}$ is the component of impact velocity projected in the direction normal to the impact plane. For shear wave propagation this equation may be adjusted to be in terms of C_S and $v_{p,transverse}$.

Under such conditions, the normal stress wave sweeps across the material, off-axis from the surface normal. Upon the arrival of the normal wave at the free surface, velocity diagnostics (aligned with respect to the surface normal) see an artificial decrease in normal stress (normal velocity) and the appearance of non-zero shear stress (transverse velocity) prior to the arrival of the actual shear wave. Figure 4-6 shows this phenomena through computational and experimental velocity profiles of the symmetric oblique impact of a 6061-T6 aluminum flyer onto a target of the same material with a velocity of 98 m/s and 15 deg angle. Simulations from Figure 4-6 were conducted in CTH, a shock-wave physic Eulerian hydrocode which will be described in detail in Chapter 6. Manifestation of tilt in Figure 4-6 show a negative transverse velocity arriving alongside the normal wave, and it should be noted that this can be positive or negative depending on the orientation of impact tilt.

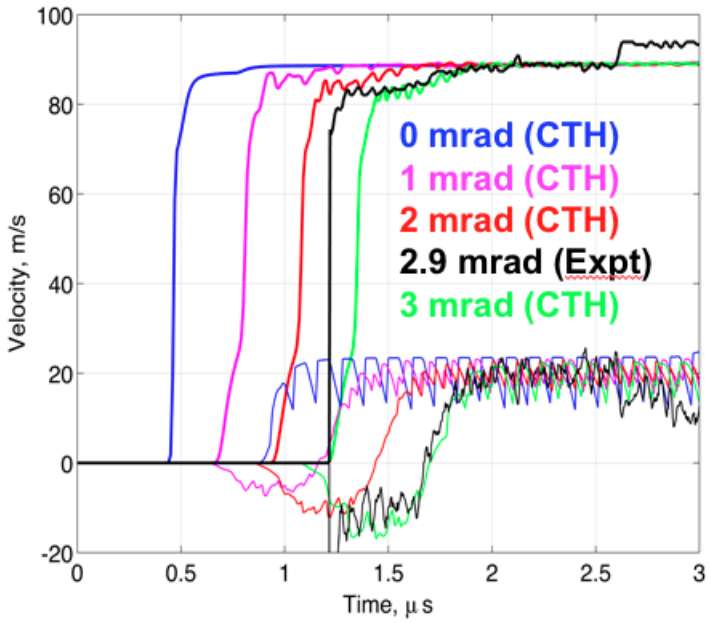

Fig. 4-6. Normal and transverse velocity profiles showing the oblique symmetric impact of (6061) aluminum at 98 m/s and a 15 deg angle. Simulations (validated by experiment) show the effect of increasing tilt in the lessening of normal velocity (and therefore stress) and the presence of transverse velocity (shear) prior to shear wave arrival.

As would be expected, this phenomena has the same effect on shear wave propagation. With increasing tilt there is less (in magnitude) shear stress and an apparent increase normal stress (w.r.t. the material surface normal). If tilt is two-dimensional (minimal skew about the shot direction axis), then the arrival of the angled shear stress wave superimposes with angled normal stress wave and tilt effects are "canceled out" resulting in equilibrium stress states identical to those expected under no-tilt conditions. Figure 4-6 demonstrates this, as all profiles converge on the same equilibrium states in both normal and transverse velocity. Some amount of tilt is present in all experiments, and is observable in this way. Because skew is negligible and end-states are achieved these portions of the transverse velocity profiles have been clipped to aid in clarity when examining profiles in the previous Figure 4-5.

4.3.3 Inferred Combined Stress States

The usefulness of observing free surface velocities is in the ability to infer the time dependent stresses occurring within the polymer specimen. This requires the use of eqs. 2.14 and 2.15, $\sigma = \frac{1}{2}(\rho_0 C_L)_R u_{fs}$ and $\tau = \frac{1}{2}(\rho_0 C_s)_R v_{fs}$, converting velocity to stress. Release stresses may also be quantified, and represents a decrease in normal stress, however this was not utilized in analysis and so processing is not detailed here.

Conversion of profiles to stress magnitude does not provide the entire context for interface dynamics. Because of the thickness of the rear anvil the longitudinal and transverse waves are further separated in time, because of the differences in sound speeds. As such, each trace must shifted in time to reflect the combined stresses occuring at the interfaces rather than at the free surface. Figure 4-7 shows the same epoxy experiment in terms of normal and shear stress with times already shifted. The time axis has been left consistent with zero being the arrival of the first normal wave at the rear surface.

With processing complete, profiles are indicative of the stresses loading the polymer, specifically at the polymer-rear anvil interface. A measurement window over which to quantify the combined stress state for the specimen is then chosen. This is based on the transverse velocity state and an average value is found for both normal and shear stress over that duration. While much consideration was given to wave structure within the normal (velocity/stress) wave profiles, the low magnitudes seen in transverse velocities make it difficult to discern any comparable structure - particularly due to the large (between 12-15 percent) uncertainties seen for transverse PDV measurements. As such, average state values were considered sufficient.

The normal stress state represents the confining stress within the polymer, 780 MPa for Figure 4-7. Likewise the shear stress is the quantification of any shear propagtion through the polymer specimen, which can be observed to be 91 MPa in the example. From velocity profiles, it was evident that transverse velocity was approximately $13 m/s$ less than expected from impact conditions. The transverse velocity is then assumed to be indicative of polymer yield, meaning the resulting shear stress is equal to the polymer yield strength in shear.

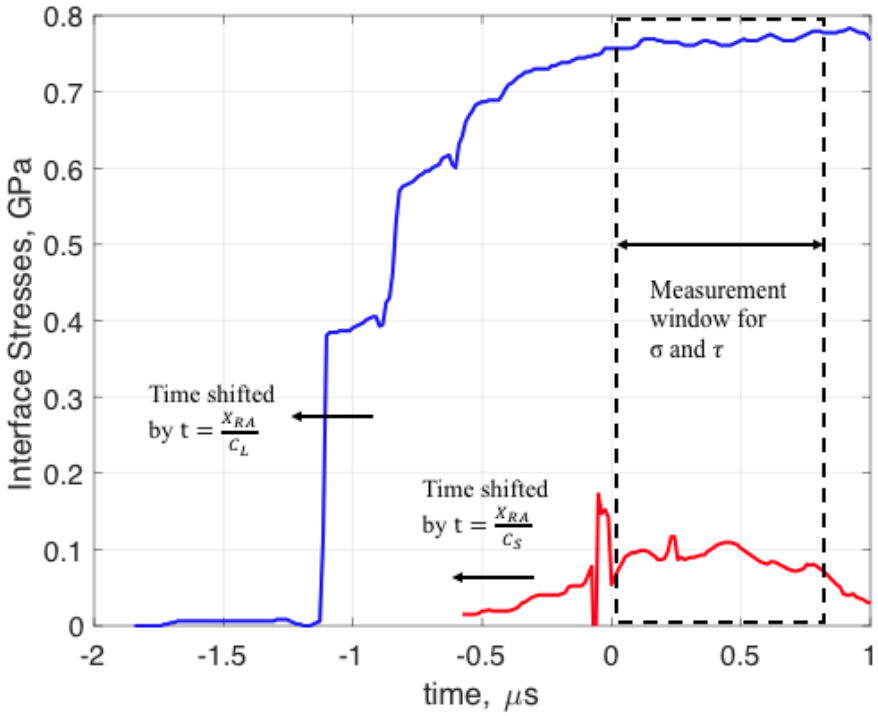

Fig. 4-7. Normal (blue) and shear (red) stress profiles calculated from free surface velocities. They have been time shifted with respect to respective sound speeds and represent the transient stress state within the polymer specimen. Data was from the same oblique impact of epoxy experiment with conditions of 96.7 m/s velocity and an oblique angle of 20 deg.

4.3.4 Yield Surfaces

The 13 CPPSPI oblique impact experiments conducted on the polyurethane and epoxy of interest covered a range of normal stresses from 400 to 800 MPa with imparted shear stresses up to approximately 120 MPa. When compared, these demonstrate the effect of confining normal stress (representative of pressure) on polymer yield strength in shear. Figures 4-8 and 4-9 present the results for both polyurethane and epoxy (respectively) in shear-confining stress space. Also included are the material responses from dynamic friction oblique impact (DFI) experiments and the low-rate tests discussed previously. DFI results will be detailed in the following section, but are included now to provide a more comprehensive look at material behavior over a wider range of tested conditions. Low strain-rate testing was done with no confinement (see Preliminary Characterization), while DFI tests subject normal-shear stress loading simultaneously (CPPSPI consists of normal *then* shear stress loading). It is important to note that these test are not equivalent. Errorbars in all results were calculated using the method for propagation of uncertainty taking into account measurement error in sound speed, density, and PDV spectogram variance. Error was calculated using the traditional uncertainty propagation via eqs. 2.8 and 2.9 **??**. Shear stresses imparted by the two lowest stress uniaxial experiments are provided for comparison. These should not be considered polymer strengths, but as shear caused by differences in principal stresses (i.e. $\tau = \frac{1}{2}(\sigma_1 - \sigma_2)$).

First consider polyurethane results, Figure 4-8. Qualitatively there appears to be a linearly increasing correlation between confining stress and polyurethane yield strength made particularly apparent with the inclusion of data with lower or no confinement. Attention is drawn to data in excess of approximately 670 MPa where shear strength appears to roll off. While further testing is always

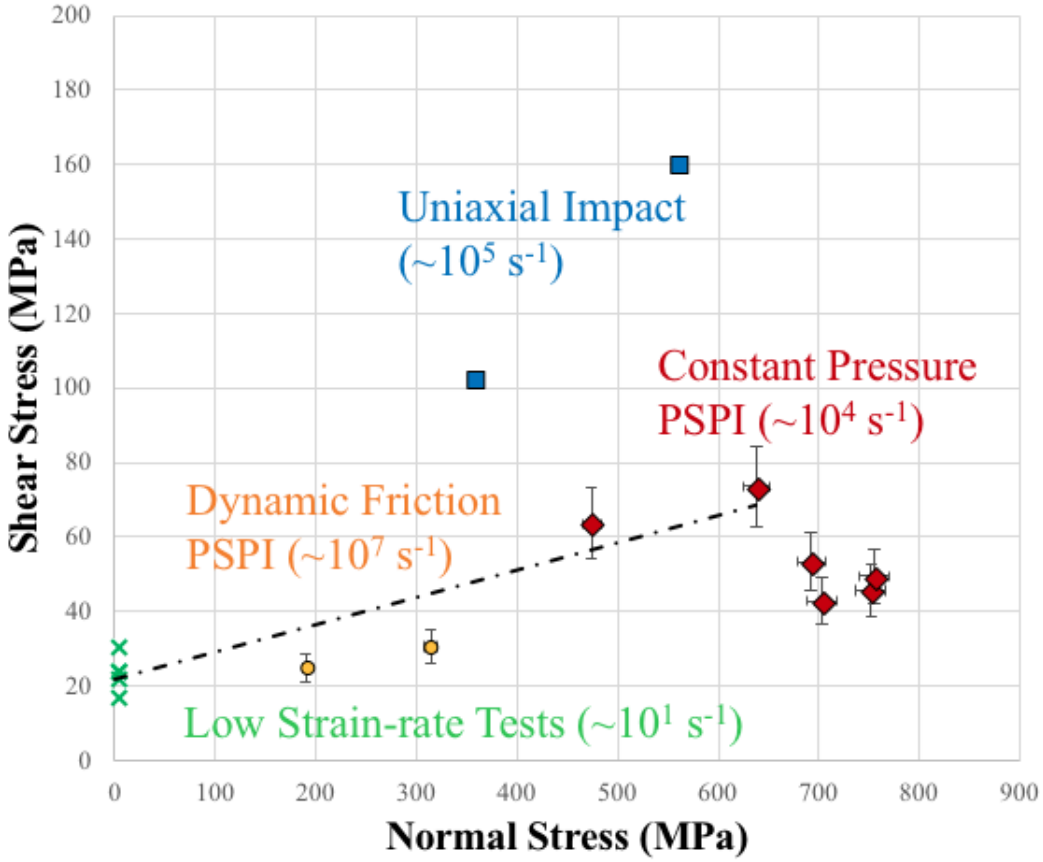

Fig. 4-8. Shear strength of polyurethane over a range of tested confining stresses. Results suggest a linear increase in strength with increasing confinement which is made more apparent with the inclusion of lower confinement DFI and low strain-rate responses. At normal stresses in excess of 670 MPa there appears to be a dropoff in strength reminiscent of a Drucker-Prager failure cap.

desired, behavior infers a threshold after which normal stress alone may render polyurethane unable to support shear. This is conceptually compatible with the elastic-plastic transition into hydrodynamic behavior discussed in the context of shock compression in Chapter 2. Notably, even this is speculations as some other viscoelastic mechanisms may instead be responsible for decreased strength. Regardless, analytically this sort of yield phenomena has been modeled through a Drucker-Prager failure ”cap”. This mathematically imposes a strength limit on an otherwise infinitely strong pressure-dependent material.

As noted previously, DFI results will be detailed in a later section, however it is worth mentioning that qualitatively shear strengths in such an orientation appear low (for PUR). This cause of this cannot be known for certain. It is speculated that either (A) yield is not occurring at all, and these values represent the full shear stress response of polyurethane, or (B) the yield strength of PUR undergoing simultaneous pressure-and-shear is less than that undergoing pressure-then-shear loading. Regardless, the trend of increasing shear response with increasing normal stress (pressure) persists.

Assuming the observed roll-off is a failure cap, linear strength dependence on confining stress for polyurethane is then restricted to between 0 and approximately 670 MPa. A simple linear regression suggests a line fit of eq. 4.3

$$\tau = 0.073\sigma + 21.873\,[MPa] \tag{4.3}$$

Recalling $\sigma = \sigma_{11} = 3P\frac{1-\nu}{1+\nu}$ for an isotropic material (which is assumed here), and that the poisson's ratio for polyurethane is $\nu \approx 0.3$, the same relations may be restated as eq. 4.4 or reformulated in terms of von-Mises equivalent yield stress ($\sigma_{vm} = \sqrt{3J_2} \approx \sqrt{3}\tau$) and pressure shown in eq. 4.5

$$\tau = 0.118P + 21.873\,[MPa] \tag{4.4}$$

$$\sigma_{vm} = 0.204P + 37.89\,[MPa] \tag{4.5}$$

Now consider Figure 4-9 which presents the CPPSPI results for epoxy in shear-normal stress space. The same motivations drive the inclusion of data from other test. Consistent with polyurethane results, epoxy strength also shows a linear correlation with confining normal stress.

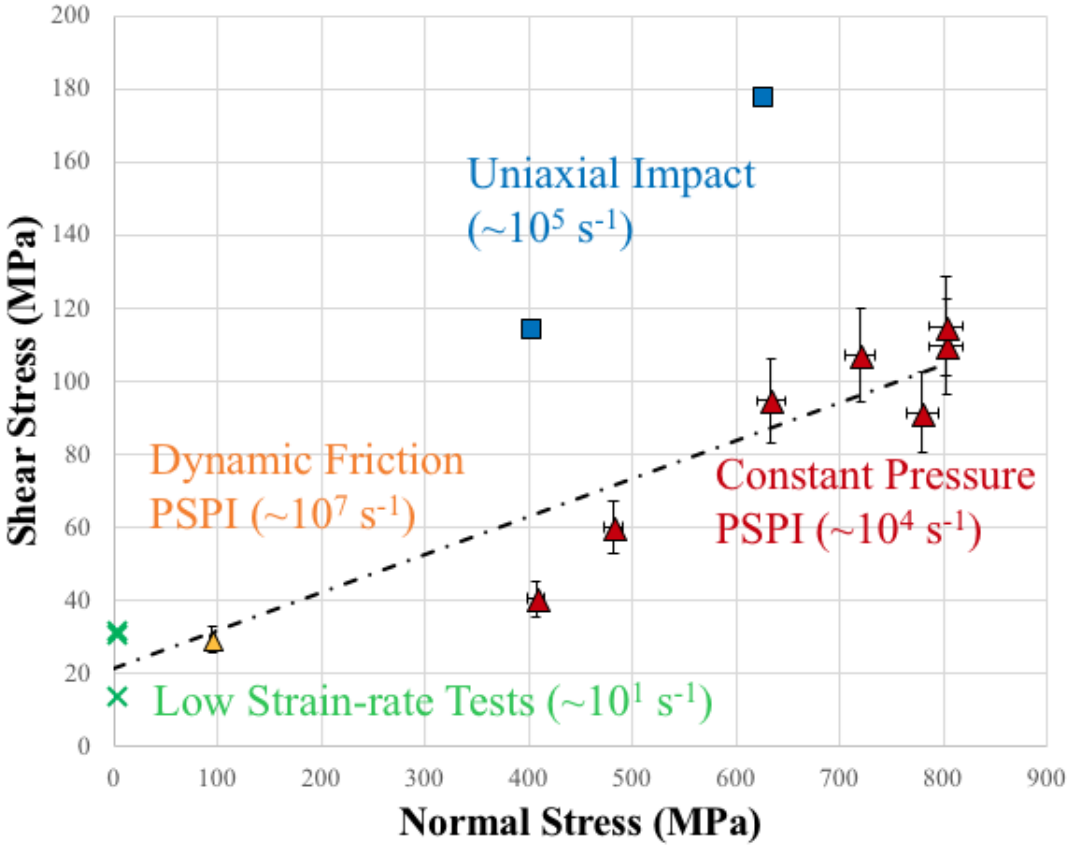

Fig. 4-9. Shear strength of epoxy over a range of tested confining stresses. Results suggest a linear increase in strength with increasing confinement which is made more apparent with the inclusion of lower confinement DFI and low strain-rate responses. No failure cap is evident in this range.

No evidence appears to be present of a failure cap as was seen with PUR. It is believed that if the tested regime was expanded to higher impact velocities (via high impedance anvils) this behavior would become apparent but this cannot be corroborated with the available data-set. Higher stress testing could not be done with the 7075-T6 aluminum anvils as the HEL would have been exceed and the elastic wave theory implemented in analysis would have been invalid. The same normal stress (pressure) dependencies are observable, and are quantified through the same linear-regression fits. Unlike PUR, all data is included given the absence of cap behavior. These are stated in eqs. 4.6, 4.7, and 4.8. For these calculations,

Poisson's ratio is again assumed to be 0.3 which is specified for the epoxy as well. This is an approximate Poisson's ratio, which is known to vary in polymers even with slight differences in processing.

$$\tau = 0.1043\sigma + 21.203\,[MPa] \tag{4.6}$$

$$\tau = 0.168P + 21.203\,[MPa] \tag{4.7}$$

$$\sigma_{vm} = 0.291P + 36.72\,[MPa] \tag{4.8}$$

Slopes describing confining stress dependence in Eqs. 4.4 and 4.7 can be compared to similar values found in literature for lower strain-rate experiments. In his work, Rosenberg [21] reported slopes of 0.2 $\frac{MPa}{MPa}$ for plexiglas and 0.196 $\frac{MPa}{MPa}$ for cellulose acetate. Similarly Tabor found slopes of between 0.1-0.24 $\frac{MPa}{MPa}$ for PMMA and 0.17-0.45 $\frac{MPa}{MPa}$ for polystyrene, in his low-rate study of the shear properties of thin film polymers [86]. These previous investigations agree quite well with the results found here despite differences in strain-rate and loading conditions.

While the data-set is limited, other polymers have been explored using oblique impact. Analytic models have also been formulated which predict the pressure-dependence of polymer strength. Figure 4-10 presents data from this study alongside amorphous polycarbonate data from Prakash [25], polyurea shear sensitivity observed by Jiao and Clifton [23], and the Mulliken-Boyce analytic model [91]. Good agreement can be seen.

It is here that an important disclaimer must be noted concerning the use of proposed yield surfaces. Overall results have relied on the coalescence of strength measurements from multiple experiments (CPPSPI, DFI, and Low strain-rate tests). Each has subjected the polymers of interest to different load conditions implicit to

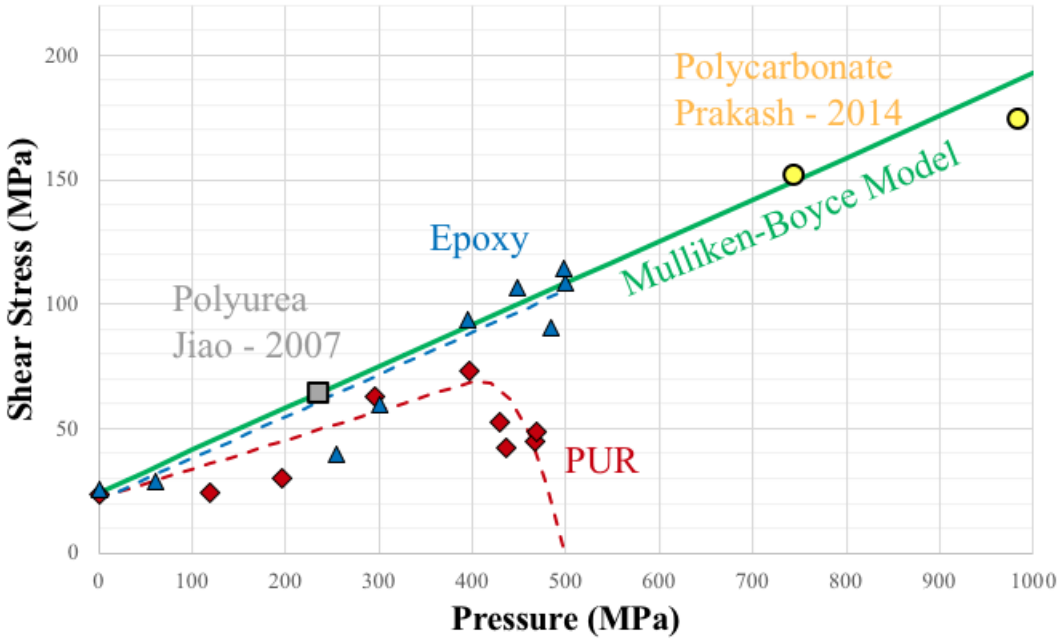

Fig. 4-10. Shear strength with respect to pressure for polyurethane and epoxy, compared to data found for polycarbonate, polyurea, and finally an analytic model by Mulliken and Boyce.

each set. As such the numerical relations proposed for a pressure-dependent yield criteria must be considered approximate.

4.3.5 Strain-rate Effects

Aside from pressure/confinement dependencies found and discussed up to this point, polymers are known to be strain-rate dependent. Furthermore, this rate dependence is known to be highly nonlinear. A review by Siviour and Jordan [66], strain-rate behaviors of polymers in general are discussed. They observed that in general there is very little increase in strength up to around $10^3 s^{-1}$ which then quickly transitions into a strong dependency where strength can be doubled over an order of magnitude of strain-rate. Their review of data included specimens subjected to a range of pressures however, and it is of interested to decouple strain-rate from pressure dependencies. Figure 4-11 presents data from uniaxial and oblique impact as well as low strain-rate shear testing plotted in stress/strain-rate space. Both stress and strain-rate values were taken at observed experimental equilibrium states. The plotted strain-rates take into account both longitudinal and transverse strain (if applicable), through a von-Mises relation.

In agreement with literature [66], two regimes are readily distinguishable with almost no strengthening observed until high strain-rate oblique impact. Strain-rate alone does not corroborate this behavior as DFI experiments (with characteristically lower pressures but higher strain-rates) show a lower magnitude shear stress response. This suggests then that polyurethane strength is more dependent on pressure that strain-rate. It is expected Hopkinson bar data be a useful supplement to this observations. Note, strain-rate in DFI experiments was defined with polymer surface roughness as the characteristic length scale.

Epoxy data, shown in Figure 4-12.

To provide further context, and connect to related concepts, it is useful to compare behavior alongside results from other dynamic experiments. In shock-compression studies, strain-rate dependencies are often discussed in terms of a

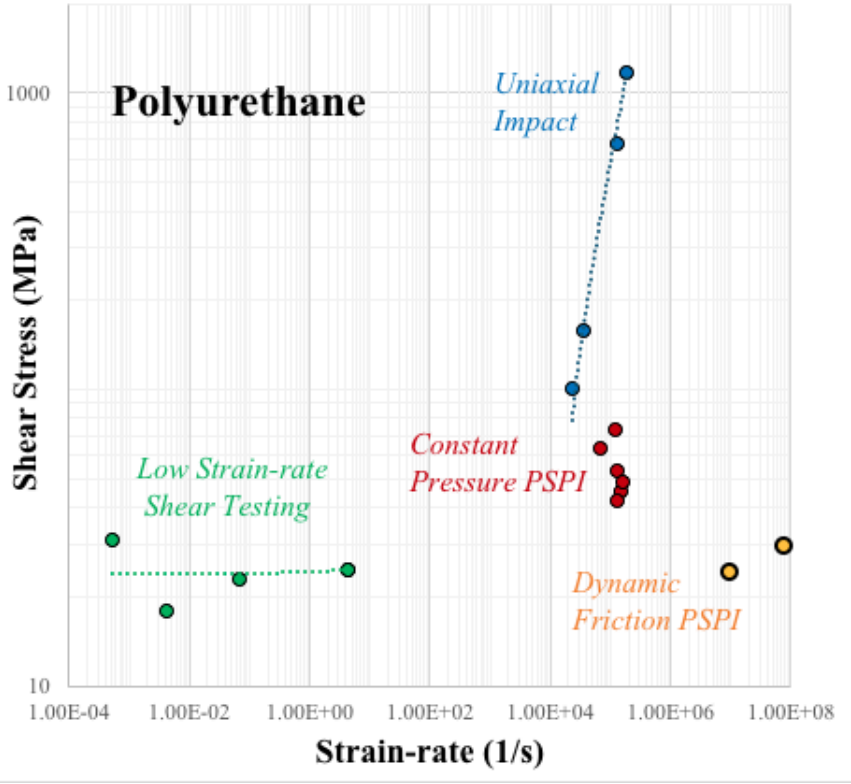

Fig. 4-11. Strength over a range of tested strain-rate conditions for polyurethane. Data is in terms of shear stress and strain-rate. Both CPPSPI and DFI experiments were conducted at similarly high strain-rates, however pressure loading in DFI is much lower. The result suggests that pressure dominates polymer strengthening (for the observed conditions). Uniaxial impact shear stress is included as a point of reference, though again is not a metric for polymer yield.

Swegle-Grady formulation expressed as eq. 4.9

$$\dot{\epsilon} = K\sigma^n \tag{4.9}$$

Fitting the oblique impact polyurethane and epoxy results into such a form produces stress exponents of $n \approx 2.09$ and $n \approx 1.02$ respectively. Shock studies conducted on epoxy/aluminum and epoxy/stainless-steel layers, tested over 10^5 to $10^7 s^{-1}$, found exponents of $n \approx 2.1$ and $n \approx 1.1$ [116]. Loading conditions are quite different, but overall exponent values are relatively close. Such a conclusion

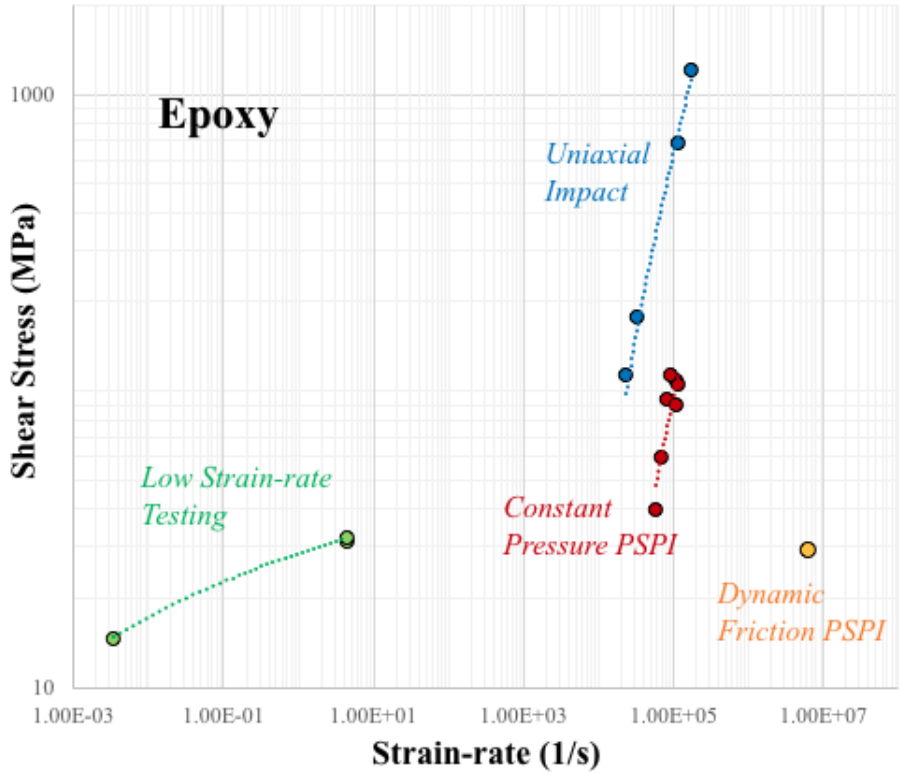

Fig. 4-12. Strength over a range of tested strain-rate conditions for epoxy. Data is in terms of shear stress and strain-rate. Both CPPSPI and DFI experiments were conducted at similarly high strain-rates, however pressure loading in DFI is much lower. The result suggests pressure dominates polymer strengthening (for the observed conditions). Uniaxial impact shear stress is included as a point of reference, though again is not a metric for polymer yield.

is qualitative only, with more extensive testing over wider parameters necessary to be declared with any certainty. With further consideration, comparing such metrics across varying loading conditions could serve as a metric in determining the validity of using Hugoniot-based equations-of-state to model off-Hugoniot material behavior.

4.4 Conclusions

4.4.1 Overview

In summary, 13 CPPSPI oblique impact experiments were performed on thin polyurethane and epoxy specimens molded between two 7075-T6 aluminum anvils confining the material. Polymer shear strength was observed over confining stresses between 400 and 800 MPa in an effort to map a material yield surface for each. In both cases, shear strengths were found to linearly increase with increasing confinement reminiscent of the Drucker-Prager yield criterion. For confining stresses exceeding 670 MPa, polyurethane sees a significant drop in strength suggesting the presence of a possible failure cap. This suggests that normal stresses exceeding that magnitude begins the transition into more plastic, perhaps almost hydrodynamic, deformation. Epoxy, in contrast, shows no evidence within the same range of confining stress, but it is hypothesized that similar behavior would occur if higher stresses were tested.

Both exhibit two distinct strain-rate dependencies similar to other polymers observed in literature - minimal dependence at low strain-rates and significant dependence at high strain-rates. High strain-rate behaviors for both polymers, fit to a Swegle-Grady relationship, are found to behave similarly to uniaxial shock compression experiments done for comparable materials. Despite known strain-rate dependency, pressure was found to have a more dominate role for both polyurethane and epoxy.

4.4.2 Implications of Adhesion

A prominent unanswered question, unavoidable when examining these results, is whether the strength being measured is that of the bulk polymer mate-

rial or rather the adhesive strength at the polymer-anvil interface. The relevant physics governing each, while of course interconnected, would appear quite distinct. Even if polymer processing concerns are assumed equal and strength dependencies have similar trends, bulk material strength is dictated by the internal interaction of polymer-chains while adhesion is determined by both polymer-metal surface interactions.

Consider low-rate testing detailed in Chapter 3. As mentioned, a motivation for performing such characterization was to evaluate possible discrepancies between thin-film (potentially adhesive) polymer behavior and that of the bulk material. Performed at identical strain-rates, the measured ultimate shear strengths were identical between the two configurations for both materials. The most apparent discrepancy was the shear moduli and related material toughness. While the epoxy was more brittle than polyurethane overall, the thin film case was significantly more brittle than the bulk case for both (by an order of magnitude). This is hypothesized to be due, mechanically, to the inability for polymer-chains to disperse stress (relax) in the thin film case. With this in mind, it is inferred that the thin film behavior (under comparable loading conditions) would perhaps vary in the failure energy it could sustain but would fail under the same stresses as a bulk material.

While this is informative conceptually when dissecting oblique impact tests on similar thin films, it still does not isolate which phenomena is being observed - only that if interface adhesive strength is being seen that it is qualitatively close in magnitude to that of the pure polymer strength. Tabor made similar comments in his study on thin films polymer strength [86]. He found pressure dependence of thin films v. bulk polymers to have comparable values with potential variation attributed to processing differences. Additionally, surface roughness was varied in CPPSPI tests (over a limited range always less than 10um Ra) and little change

was *observable* - change which would be expected if correlated surface adhesion was also changing.

Following this train of thought, reconsider the surface physics discussed in Chapter 2. The total shear strength of an interface is thought to be governed by two main processes; the the interlocking of surface roughness features, and the inter-molecular bonding between surfaces (polymer and substrate). This is mathematically stated in eq. 4.10, with similar formulations explained more eloquently by [6] [9].

$$\tau(P) = (\mu_{adh} + \mu_{def})P + \sigma_{adh} \tag{4.10}$$

Roughness interactions are modeled through the classic Coulombic relationship $\tau = \mu P$, where $\mu = \mu_{adh} + \mu_{def}$, decoupled into a deformation and mechanical adhesion term. Deformation refers to the shearing action of surface asperities acting as gears at which point failure is failure of the "teeth" themselves (bulk material). μ_{adh} describes the mechanical welding that occurs along the peak-to-peak contact of asperities, enabled by the *very* small surface areas involved. Despite the incredibly high pressures which could produce strong weld conditions, this strength cannot greatly exceed that of the material itself otherwise the asperity itself could rupture. Restating Figure 2-9 from Chapter 2, Figure 4-13 re-presents schematically distinct behavioral contributions.

Non pressure-dependent adhesion (including chemical considerations) is stated plainly as σ_{adh}, but this masks complex functionality reliant on surface energy and polymer wetting during molding. Overall, this relationship is assumed valid for the interface, but notably takes a form similar to that of bulk polymer strength $\tau = aP + \tau_0$ (as shown in eq. 4.7). By inspection,

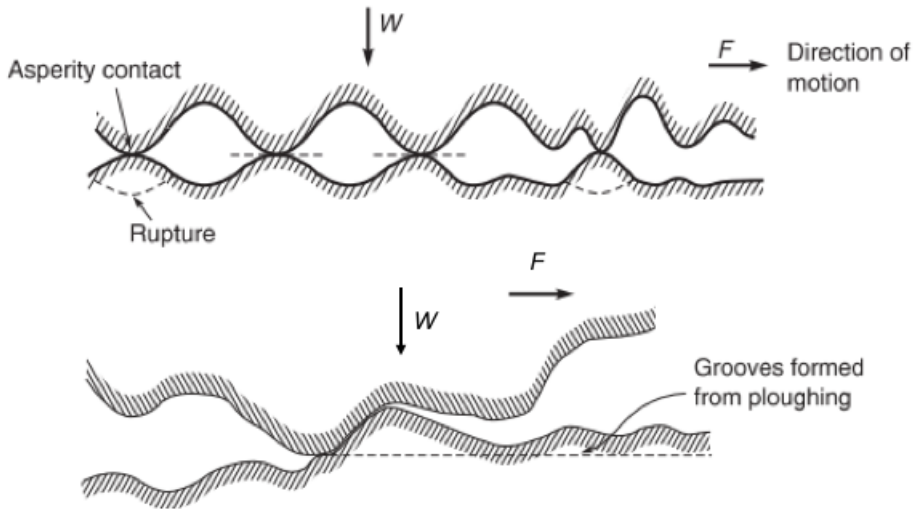

Fig. 4-13. Example of "rough" solid-solid surface contact through asperities, from [9].

$$if\ \tau_{interface} = \tau_{polymer} \tag{4.11}$$

$$then\ a = \mu\ and\ \tau_0 = \sigma_{adh} \tag{4.12}$$

However, if the two are distinct, then the measurement of a coefficient of friction, and estimate for μ at similar loading conditions would provide an approximation for the adhesive strength contribution through the reformulation of eq. 4.10.

$$\sigma_{adh} = \tau - \mu P \tag{4.13}$$

This requires the isolation of μ from other surface behaviors; in other words, removing the effects of adhesion in an effort to quantify it. This motivates the implementation of dynamic friction oblique impact experiments. Through such testing, a dynamic coefficient of friction can be measured at the same strain-rate

and (similar) stresses for both epoxy and polyurethane paired with the same 7075-T6 aluminum used as anvils in CPPSPI experiments. The resulting μ may then be compared to the shear-to-pressure slope found in yield surfaces and more informed comments may be made on the role of adhesion.

CHAPTER 5

QUALITATIVE SEM ANALYSIS

To provide some amount visual context for the measured material response, scanning electron microscopy (SEM) was performed on both polyurethane and epoxy specimens. Figures 5-1 - 5-7 show images taken from raw molded samples as well as post-mortem examples taken from low and high strain-rate experiments. The interaction of polymer chains was not observable as they are on the scale of nanometers to angstroms; however, qualitative images of failure were resolvable on the scale of microns. Evidence of ductile and brittle failure can be identified in low-rate polyurethane test images corroborating stress-strain results of greater toughness, while brittle failure dominants the epoxy response. Images from samples which had undergone PSPI loading show a rough and chaotic microstructure persistent throughout the sample as evidence of material deformation and failure. This is particularly apparent when constrasted against un-shot specimens which show a more smooth and homogeneous surface in both cases (typical of amorphous polymers). Figures are presented followed by a discussion.

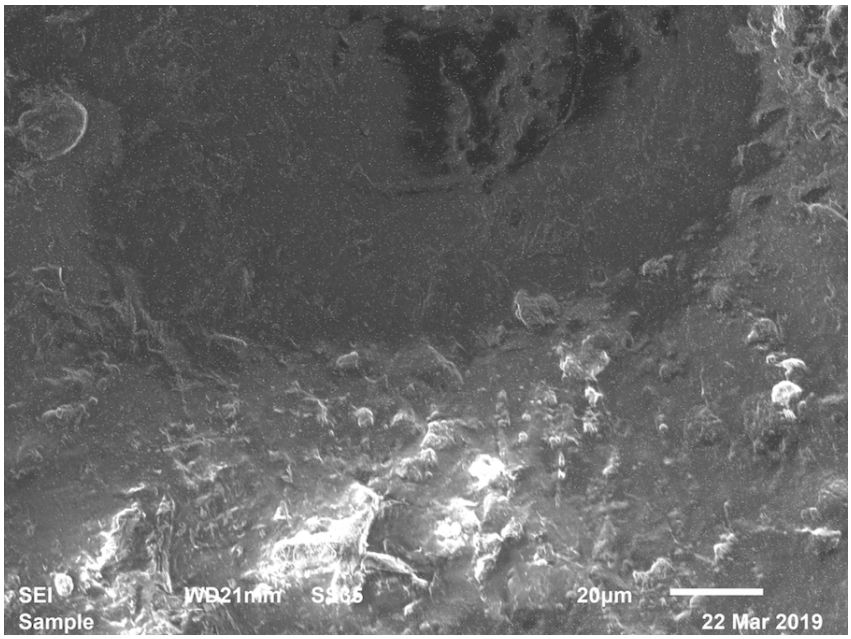

Fig. 5-1. Molded polyurethane imaged at x700 magnification.

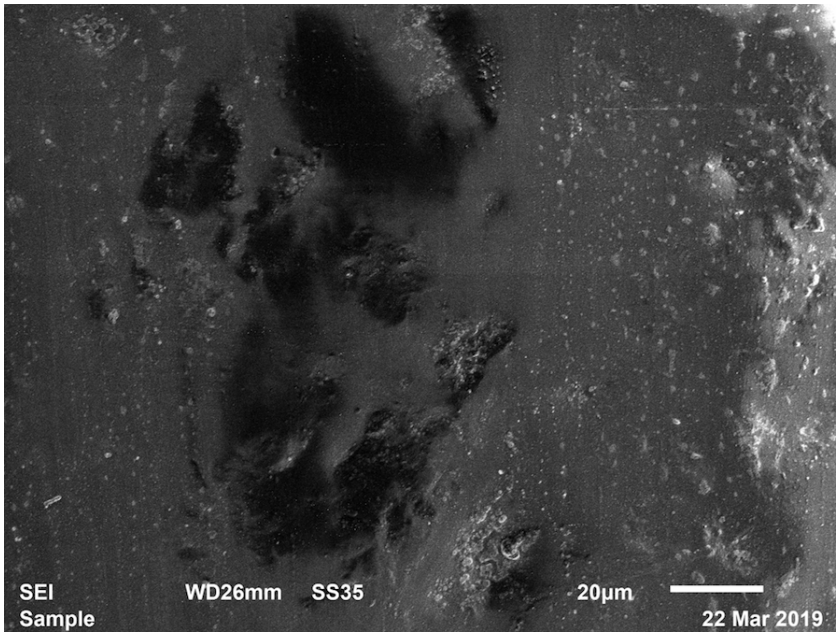

Fig. 5-2. Molded epoxy imaged at x700 magnification.

Pre-shot samples, Figure 5-1 and 5-2, consisted of polymer materials which has already been degassed and were molded into a 2 inch diameter, approximately 5mm thick, puck. They originally used for longitudinal and transverse sound speed measurements. SEM images were taken on the surface of both the polyurethane and epoxy, as opposed to examining a cross-sectional area. Surfaces were not were lapped or polished and so some topological contours are expected. Both polymers look fairly homogeneous in texture suggestive of being fully-dense, with no micro-bubbles apparent.

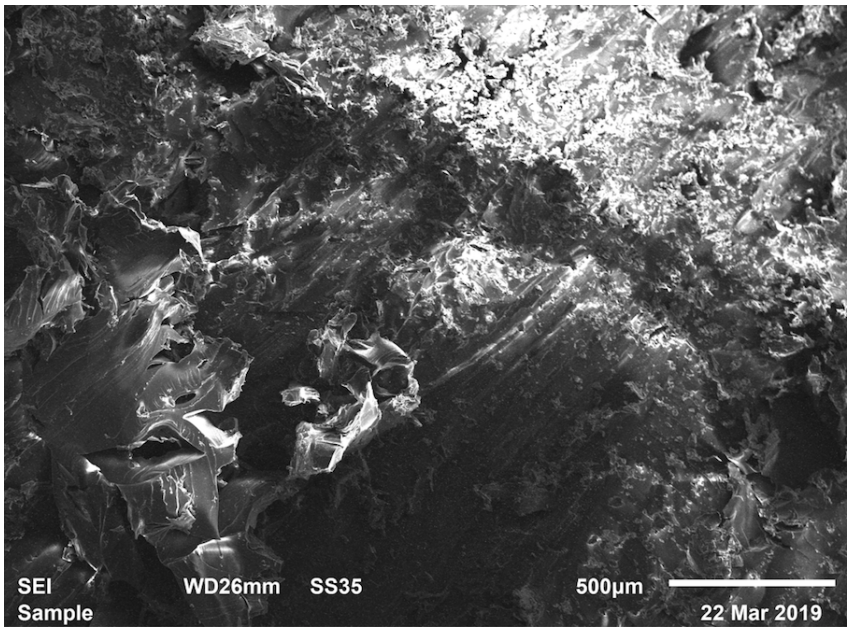

Fig. 5-3. Post-mortem of a polyurethane specimen sheared at $10^0 s^{-1}$, x50 magnification - image 1/2. Evidence of ductile and brittle failure of amorphous structure.

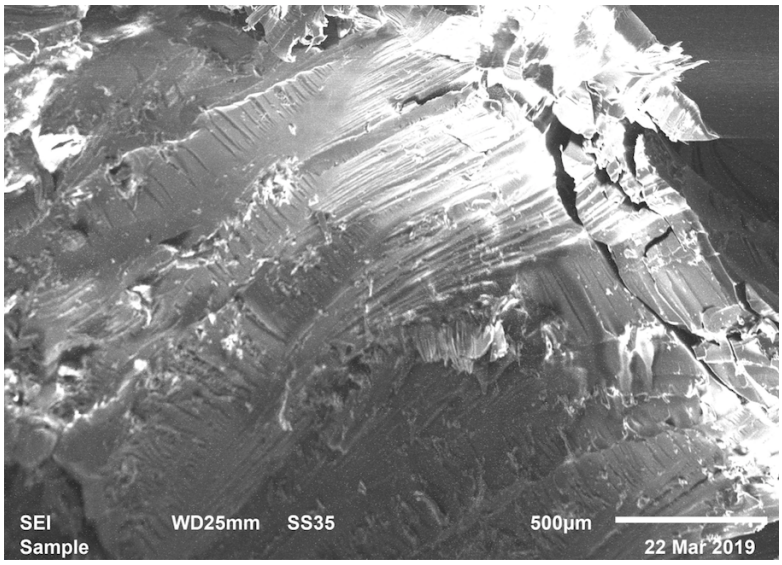

Fig. 5-4. Post-mortem of a polyurethane specimen sheared at $10^0 s^{-1}$, x50 magnification - image 2/2. Increasing evidence of brittle shear failure found closer to the shearing plane.

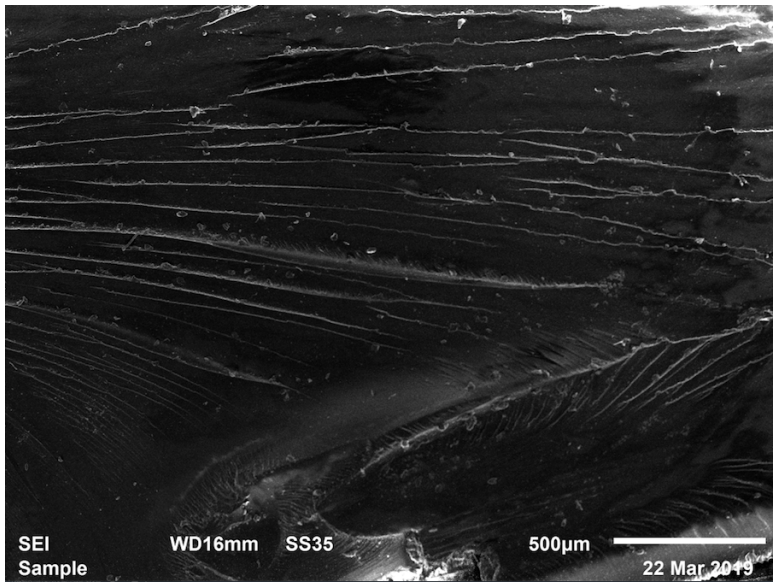

Fig. 5-5. Post-mortem of an epoxy specimen sheared at $10^0 s^{-1}$, x50 magnification. Brittle failure is predominant with little evidence of ductility found, consistent with stress-strain results.

Low strain-rate test samples, Figures 5-3 - 5-5, were taken from the bulk material specimens (not thin film), specifically those which experienced the fastest shearing deformation ($10^0 s^{-1}$). Failure modes are readily observable. For polyurethane there is evidence of ductile tearing in addition to shear planes. In contrast, only shear is identifiable in the epoxy specimen. This corroborates stress-strain trends which suggested epoxy to be more brittle while polyurethane exhibited more toughness - related to the more ductile failures present.

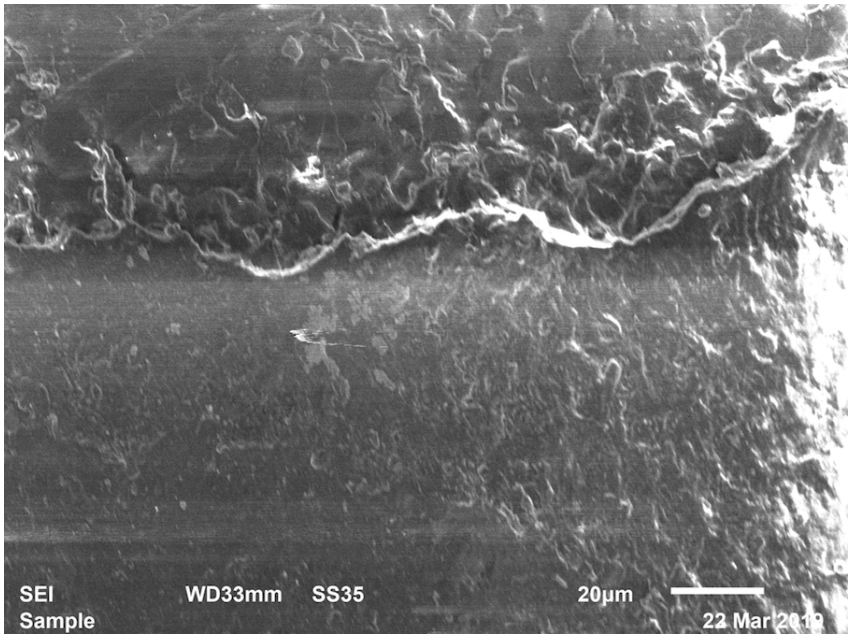

Fig. 5-6. Post-mortem of a thin polyurethane PSPI specimen, impacted at ∼100 m/s (18 deg angle). x700 magnification.

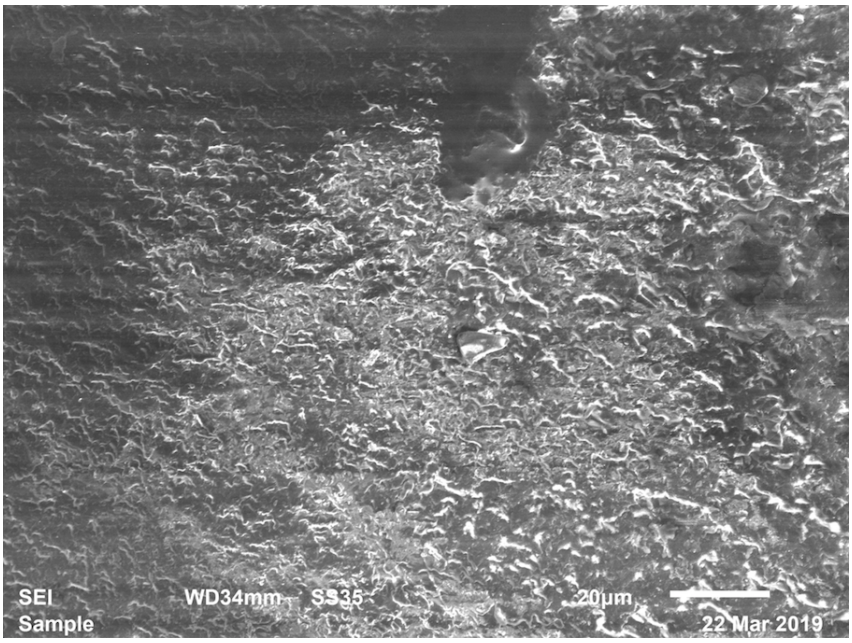

Fig. 5-7. Post-mortem of a thin epoxy PSPI specimen, impacted at ∼79 m/s (20 deg angle). x750 magnification.

Lastly, post-mortem samples recovered from CPPSPI experiments are considered in Figures 5-6 and 5-7. These are best discussed specifically in comparison to the pre-impacted molded specimens. Observable texture is consistent throughout the entirety of the field-of-view for both specimens. The homogeneity is qualitatively quite ruffled in comparison to their pre-tested counterparts. This could be the manifestation of yield (damage) which permeated through the polymer specimens throughout pressure-shear loading. These perturbations are more frequent in the polyurethane image, particularly around the crack. While notable, the crack itself could have formed during the CPPSPI experiment, the catastrophic aftermath, or even when separating the confining anvils to retrieve a polymer sample - as such no conclusions concerning its origins may be made. If the texture change is damage than it is qualitatively pervasive perhaps isotropic throughout the specimen.

CHAPTER 6

DYNAMIC FRICTION OF POLYMER-ALUMINUM TRIBO-PAIRS

6.1 Introduction

The next portion of experimental investigation explores the dynamic friction behavior between both polyurethane or epoxy polymers and a 7075-T6 aluminum tribological partner. Transient normal and shear stresses were inferred from particle velocity histories observed off the rear surface of the aluminum target impacted by an oblique polymer projectile. The ratio of these shear to normal stresses were used to quantify coefficients of friction. The overall intention was to simultaneously extend the suite of material characterization for both polymers, and to use observations of friction behavior to comment on the potential role of adhesion in CPPSPI testing. Described is an overview of the experimental methodology and corresponding results. As in the previous chapter some details have been left to the previous background/theory sections, or adjoining appendices.

6.2 Experimental Methodology

In an effort to better understand the possible effects of inter-facial friction from the behavioral contributions of material strength and adhesion during rapid shearing, a series of dynamic friction oblique impact experiments were conducted. These were conducted using at the Marquette University Shock Physics Laboratory utilized the 50.8 mm bore, slotted barrel, dual-diaphragm gas gun - shown in Figure 4-1 of the previous chapter.

6.3 Overview

Akin to a reverse ballistic experiment in uniaxial impact configurations, dynamic friction impact experiments require a projectile impactor composed of the material of interest, set at some oblique angle. This is aligned such that planar impact is facilitated of an anvil target set at the same angle. On impact, the interface is immediately subjected to compression and shear deformation, the information of which is propagated through normal and shear stress waves through the anvil material - traveling at respective sound speeds. Target material is selected such that elasticity in the anvil is maintained for the duration of the test which allows one-dimensional elastic wave theory to be employed. Stress wave dynamics are inferred from particle velocities on the rear free surface measured using PDV. Figure 6-1 shows a corresponding position-time plot with useful characteristics identified.

As shown, multiple combined stress states are experienced throughout the duration of the experiment. Initially only interface compression information is observable, with complete State 1 fixed with the arrival of the lagging shear wave sometime later. States 2 then follows, representing the partial unloading of the interface in normal stress, though with sustained shear. Eventually, complete release occurs concluding the experiment. Figure 6-1 position values are indicative of dimensions used in experimentation and, as such, multiple states were expected to be measured. Recall again eqs. 2.14 and 2.15 quantify the normal and shear stress at any point in time: $\sigma = \frac{1}{2}(\rho_0 C_L)_R u_{fs}$ or $\tau = \frac{1}{2}(\rho_0 C_s)_R v_{fs}$. A Coulombic coefficient of friction, μ, is then calculable through the ratio shear to normal stress at each state (eq 2.26). This is either dynamic or static depending on the presence of slip at the impact surface, and is specific to that tribological pair. The impact interface is subject only to friction interactions, with no adhesion existing prior to, unlike the previous CPPSPI case.

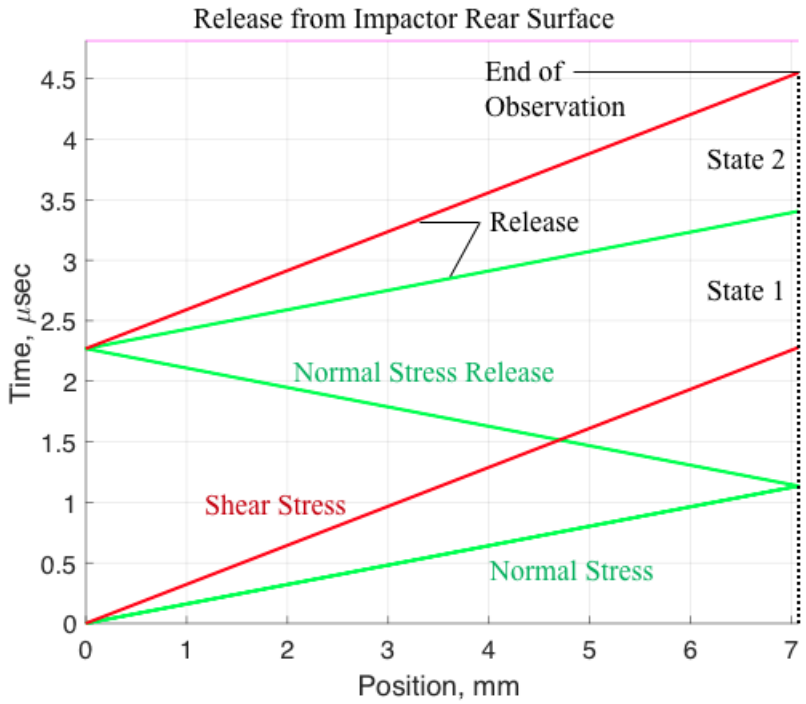

Fig. 6-1. An X-t diagram demonstrating the stress wave propagation expected in a dynamic friction oblique impact experiment. Multiple interface stress states are discernible at the rear surface including initial compression (normal stress wave arrival only), combined normal and shear stress loading (State 1), and reduced normal and shear stress loading (State 2).

Aside from friction information, the same ability to quantify stress allows this method to be utilized in the examination of potential polymer strength behaviors. Slip at the interface (i.e. dynamic friction) is indicative of material yielding in shear at the surface. This is yield of surface asperities which would otherwise interlock/mechanically-weld and transversely confine the polymer-anvil surfaces relative to each other. As in the CPPSPI experiment, the normal and shear stresses of which are quantifiable, and it is these values which have been presented already when discussing polymer yield surfaces. It has been alluded to previously that the polymer interface, in the context of DFI, is undergoing different loading conditions experiencing simultaneous pressure and shear. Strength comparisons with

CPPSPI, therefore, cannot be direct and in the most rigorous sense are only qualitative. This in mind, it is reiterated here that pressure-dependent yield surface trends using this information must be considered approximate.

6.3.1 Target Description and Setup

Polymer impactors were manufactured from the selected *Polytek* 1512 liquid plastic polyurethane and the *Atom Adhesives* F110 low viscosity epoxy. The procedure for molding was maintained including mixing, degassing, and finally molding into a negative of the impactor geometry. Curing was given the same minimum requirement of 24 hours to allow for maximum strength properties to be attained.

Anvil materials consisted of the same 7075-T6 aluminum alloy, with a density of 2.792 g/cc and sounds speeds of 6.23 and 3.10 mm/μs for the longitudinal and shear wave-types respectively. This was to correspond to the anvil materials used in the constant-pressure pressure-shear plate impact experiments. Anvil surface roughness Ra metrics were taken, and are included in Table 6-1. Figure 6-2 features a cartoon schematic of dynamic friction impact alongside an angled epoxy impactor set into a sabot, as well as an assembled aluminum target.

Alignment was achieved using the same multi-step procedure, as detailed fully in Appendix B, accounting for barrel/target concentricity, target mount-plate orthogonality, and the angular orientation of the target with respected to the angled impactor. Diagnostics included both PZT pins and normal/transverse PDV observations. PZT pins were embedded in the surfaces such that they protruded less than a millimeter, and upon impact were used to quantify tilt. Three PDV probes were again set into a bridge affixed to the back of the target. One probe was aligned to the rear surface normal while the other two were skewed at $\pm$20 deg in order to observe components of transverse velocity.

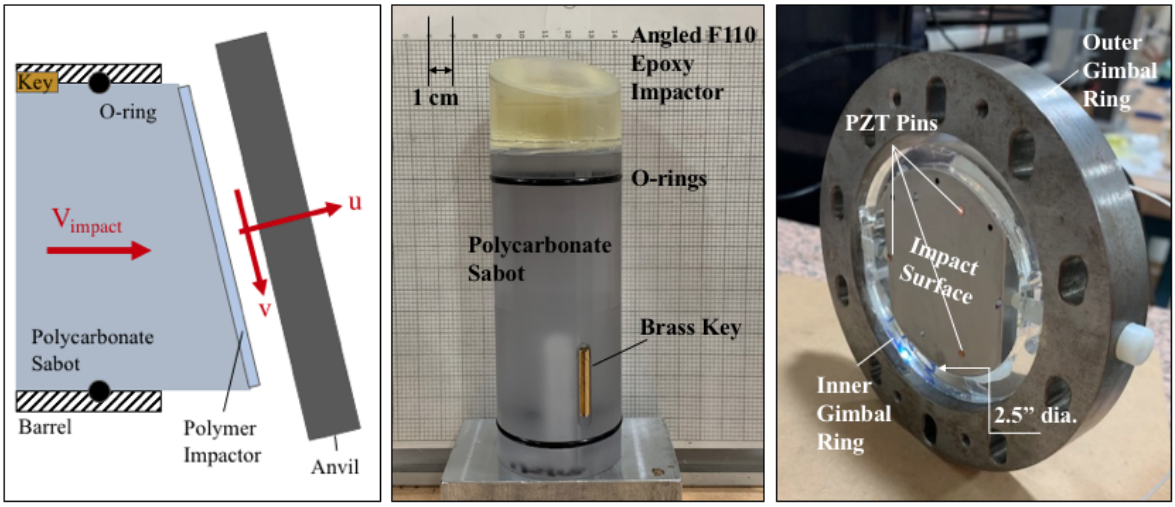

Fig. 6-2. Schematic for a dynamic friction oblique impact experiment alongside the manufactured projectile and target.

6.4 Results and Discussion

Three dynamic friction oblique impact experiments were conducted, including two with polyurethane and one with an epoxy angled-impactor. Impact conditions including velocity, angle of obliquity, roughness, tilt, and expected stress loading are provided in Table 6-1. Conducting only a few experiments was deemed sufficient to provide an estimate for coefficient of friction values for each polymer in an effort to inform other CPPSPI results. While available data is limited, which is an intended subject of future work, results provide supplemental insight to the other results detailed in this report.

6.4.1 Polyurethane

Figure 6-3 presents free surface particle velocity profiles representative of the dynamic friction results found for polyurethane. The presented experiment was conducted with an impact velocity of 122.2 m/s, a 17-degree angle of impact, and an anvil thickness of 4.4 mm. As a credibility check, observed wave structures

Table 6-1: Summary of dynamic friction experiments conducted including impact conditions, expected combined stress loading, surface roughness metrics, and impact tilt.

Impactor Material	Impact Angle ($\pm$1 deg)	Impact Vel. ($\pm$5 m/s)	Normal/ Shear Load (MPa)	Ra($\pm$0.01 μm)	Impact Tilt(mrad)
PUR	17	122.2	266/35.5	0.27	3.2
PUR	17	123.7	269/36.9	1.68	14.6
Epoxy	20	84.0	205/35.3	2.10	5.0

are similar to those seen in other dynamic friction studies [26]. The impact interface between the PUR and aluminum anvil immediately experiences both normal and shear stress loading, however the normal stress wave (traveling faster) arrives first at the rear surface which has been set, arbitrarily, to time zero. The shear wave is seen to arrive approximately 0.75 us later, at which point the combined stress state and coefficient of friction are quantifiable. Partial release propagating from the interface is apparent at approximately 1.5 us reducing the normal stress by about 60 percent, producing a rise in longitudinal particle velocity.

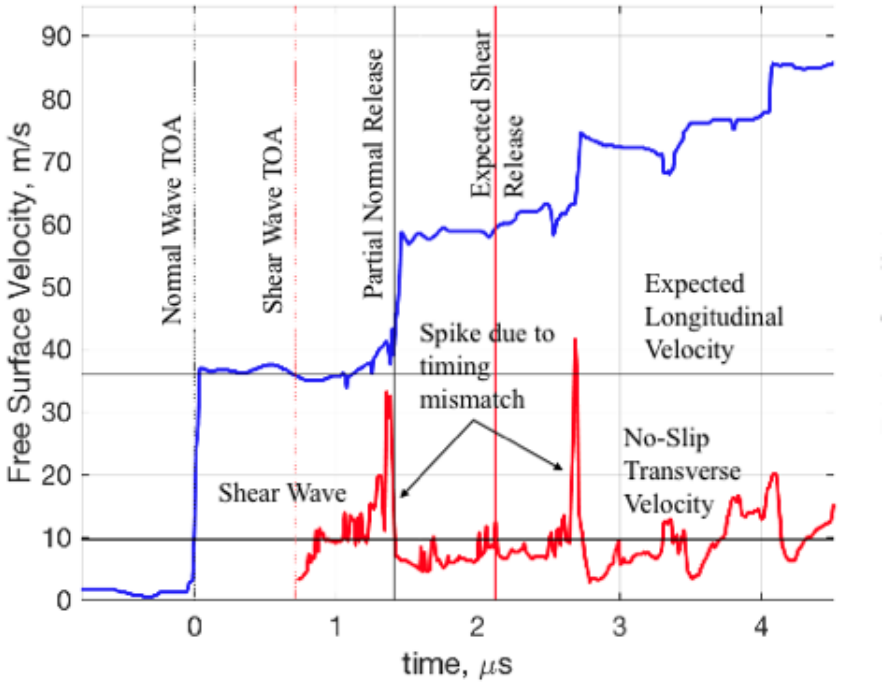
Free Surface Velocity, m/s
time, μs
Nomal Wave TOA
Shear Wave TOA
Partial Nomal Release
Expected Shear Release
Expected Longitudinal Velocity
Spike due to timing mismatch
No-Slip Transverse Velocity
Shear Wave

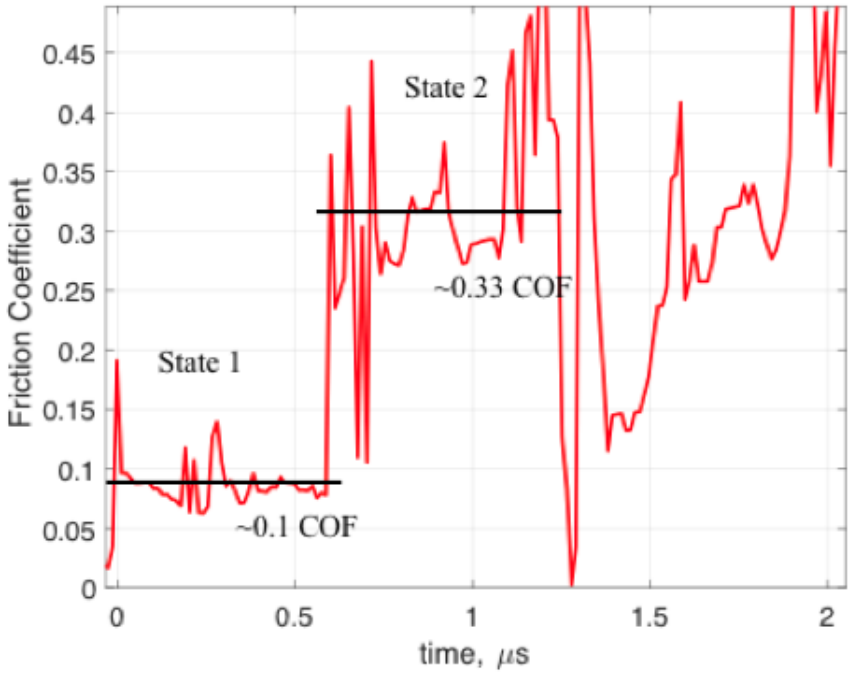
Friction Coefficient
time, μs
State 1
State 2
~0.1 COF
~0.33 COF

Fig. 6-3. (A) Longitudinal and transverse particle velocity traces representative of typical a dynamic friction experiment, results shown had initial conditions of approximately 122.2 m/s impact velocity at an angle of 17 degrees. (B) Coefficient of friction values for corresponding to each of two combined loading states.

Profiles from Figure 6-3 were converted to stress (eqs. 2.14 and 2.15) and then time shifted with respect to the delay between longitudinal and transverse sound speeds to more accurately reflect the combined loading conditions seen at the interface. This was similar to the procedure detailed in Chapter 4. The combined mechanical state (both pressure and shear stresses) are implemented into the yield surface plots previously presented. The ratio of shifted traces (Figure 6-3B) is the transient quantification of a friction coefficient for the impact interface.

Note the significant variability seen in the transverse signal (which in turn appears in the COF trace). This is caused by significantly lower signal strengths seen in transverse PDV spectrograms, which reduce the power of the sliding Fourier transforms used to convert frequency signal to velocity traces [12]. To account for this, average values were taken across each state to yield a single value. Similarly, there are large spikes in transverse velocity corresponding with the transition in compression state (labeled). Transverse signal is calculated via combining information from a normal and angled PDV collimator, very small (nanosecond) mismatches in wave rises between the two signals results result in large erroneous spikes. These have not been removed, for transparency, but were not included within velocity and stress calculations. Precursor transverse velocity due to angled wave propagation produced by slight impact tilt was present (as is almost always the case), but was clipped for clarity.

The presence of interfacial slip determined whether this was kinetic or static in nature and was found by taking the difference between expected and observed

transverse velocity. The average slip value calculated here was about 1.5 m/s over State 1. This is within the uncertainty bounds for these measurements (approximately 12 percent of imparted transverse velocity [104]), meaning it cannot be definitively concluded from data alone whether or not the no-slip condition was maintained or if a small amount of slip was occurring.

To clarify this ambiguity, impact surfaces of the polymer impactor and aluminum anvil were examined post-mortem, with a polyurethane example shown in Figure 6-4. Some significant damage is evident around the periphery most likely due to interactions within the catch tank after the experiment has occurred. The impact surface can be identified based on the imprint left by the polyurethane impactor. On both the impactor and anvil there is evidence of smearing which suggests some slip did occur.

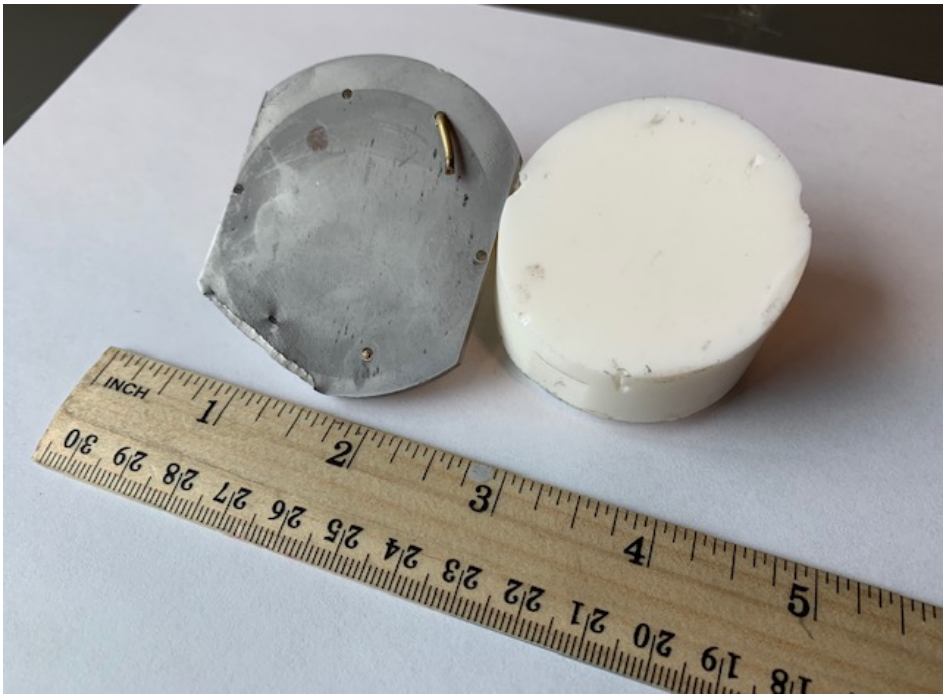

Fig. 6-4. Recovery impactor and target anvil from a polyurethane dynamic friction oblique impact experiment. Edge damage is mostly likely from secondary impacts/interactions inside the catch take experiment duration. The impact site is observable and evidence of smearing suggests slip did occur.

Taking this qualitative observation into account, it is reasonable to assume that even if the State 1 μ is static, shown in eq. 6.1, that it serves as the bound for transition from static to kinetic and so $\mu_s \approx \mu_k$. Similar rational may be used for State 2.

$$\mu_s \geq |\frac{\tau}{\sigma}| \tag{6.1}$$

For the two shots conducted on polyurethane, average μ values for States 1 and 2 were found to be 0.097 and 0.393 for an impact velocity of 122.2 m/s at 17-deg; with 0.131 and 0.289 for an impact velocity of 123.7 m/s also at 17-deg. Surface roughness (Ra) was measured at the aluminum impact interface and found to be 0.27 and 0.67 um (corresponding to the 122.2 and 123.7 m/s shots). *A prima facie* it is unapparent whether surface roughness over the tested range had any effect as values at each state were consistent between shots. The release in compression between states 1 and 2 saw an increase in μ. This trend has been seen in previous metal-metal dynamic friction testing [26].

6.4.2 Epoxy

With the implications of surface roughness being inconclusive (or simply within the "noise" of uncertainty) as well as additional logistic constraints, only one dynamic friction experiment was performed on epoxy. The same methodology was followed, and Figure 6-5 shows the normal and transverse free surface particle velocity profiles measured using PDV. Conditions included a shot velocity of 84 m/s, impact angle of 20 deg, and an anvil thickness of 6.96 mm.

On inspection, it is immediately apparent that the wave structure seen within the epoxy response is quite different than previous results in polyurethane. Instead of maintaining a flat stress state, there appears to be be immediate, but gradual stress release which is observed in both normal and transverse wave profiles.

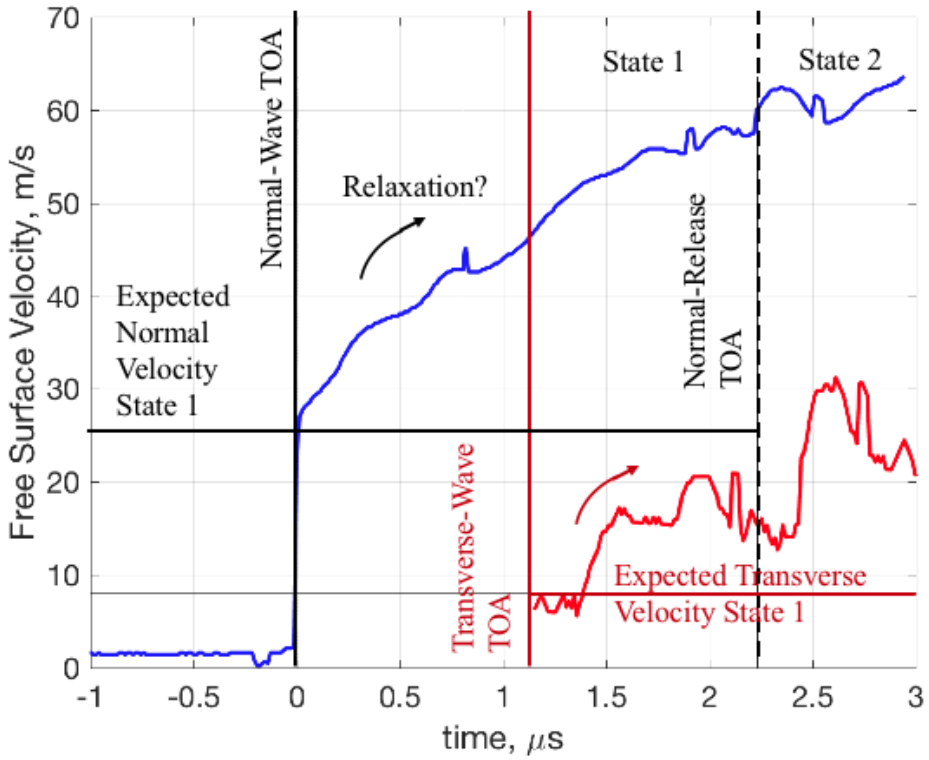

Fig. 6-5. Longitudinal and transverse particle velocity traces representative of a dynamic friction experiment on epoxy, results shown had initial conditions of approximately 84 m/s impact velocity at an angle of 20 degrees. Note the apparent release taking place within the confined state 1, reminiscent of relaxation seen in Hugoniot shots.

While unexpected, this sort of behavior has been observed before. In uniaxial impact, both Hollenbach [61] and Schuler [105] show this "rounding" during shock compression. Figure 6-6 shows a PMMA example of this from Schuler.

Before attempting to quantify friction behavior, as was the objective, the immediate question becomes first why such behavior was observed in epoxy and not in the tested polyurethane. Figure 6-7 compares the two normal profiles directly plotted in non-dimensional time to compensate for differences in anvil thicknesses.

Such a response is attributed to polymer chain interactions allowing the relaxation of an imposed stress in a constant strain-field. Therefore, cause can be

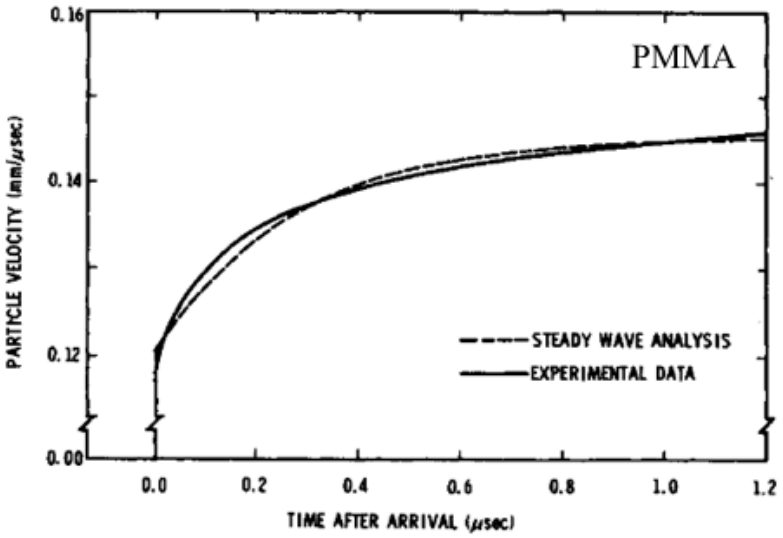

Fig. 6-6. The transient behavior of a polymers plane strain impact response showing a steep rise to an initial velocity state followed by a gradual stress relaxation (rise in velocity) to a final equilibrium state. From Schuler, this example is of PMMA.

isolated to either some fundamental difference in chemical formulation between epoxy and polyurethane (molecular weight, chain density, etc.) or to some difference in processing. While differences in formulation shouldn't be ignored, both are thermosetting polymers of high durometer made of two-part resin hardener systems. They are both show high amounts of cross-linking and are amorphous in structure. As such, it is expected that both have similar mechanical responses.

Assuming this to be true, processing must now be considered. Both epoxy and polyurethane were mixed, degassed, and molded in the same manner - leaving the only discrepancy to be cure time. Each was allowed a minimum of 24 hours to cure attaining maximum strength, however consistency was enforced in a maximum cure time. The epoxy projectile was shot shortly after the 24 hour threshold necessary for curing, while the polyurethane impactor was setting for at least 3 days (76 hours) with no exact time tracked. While accidental, if this is the cause,

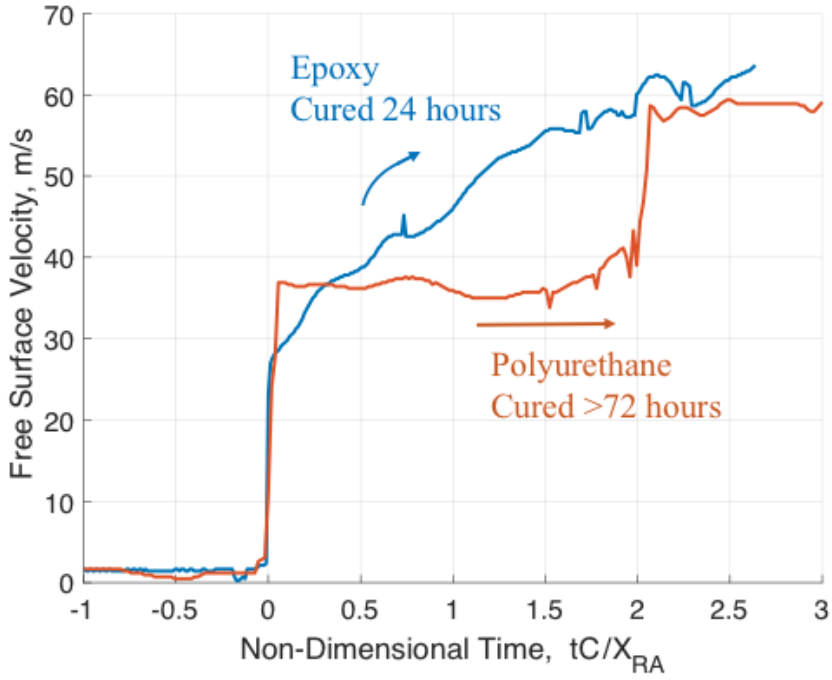

Fig. 6-7. A comparison between polyurethane and epoxy dynamic friction normal-component particle velocity profiles. Due to the difference in anvil thicknesses, time has been non-dimensionalized by the normal stress wave transit time calculated as the anvil thickness divided by longitudinal sound speed. Cure time or thermal effects are hypothesized mechanism behind the observed viscoelastic response.

the implications are significant. Of course cure time is known has implications on the mechanical response, however that viscoelastic behavior (toughness, moduli, etc.) is in flux well after cited "absolute" strength is reached.

Alternatively, the effects of temperature should not be ignored. Significant heat is known to be generated through kinetic friction as is relevant within these experiments. Both polymers are thermosetting, they have characteristically very high glass transition temperature (due to significant cross-linking) after which mechanical properties decay. Transition temperatures are specified as $90\ deg - C$ for epoxy and $122\ deg - C$ for polyurethane. The latter was approximated based on the maximum exothermic reaction temperature and may be slightly lower. Given

the relatively low stresses imparted in oblique impact tests, such a rise is not expected with the polymer material (particularly in CPPSPI experiments). However, on the scale of surface asperities in DFI tests, temperature rise could be greatly accentuated and so temperature effects cannot be eliminated. Both of the proposed phenomena discussed are pure speculation at this point. Without sufficient information to comprehensively examine the effects here, are left for future works.

Due to the transient stresses in the epoxy DFI experiment, friction is quantified using two methodologies. First, the same approach taken with polyurethane is conducted taking an average value over the duration of State 1, resulting in a measured μ of 0.26. This was an average of 0.31 and 0.17 calculated from the beginning and end stresses of State 1. For better comparison with PUR results, it is proposed that only the initial stress seen at State 1 be considered resulting in an increased value μ of 0.31, which in a sense neglects potential effects of relaxation. For similar reasons, State 2 was not considered as the effects of this rounding behavior on partial stress release were unknown. As with PUR dynamic friction data, normal and shear stress states were used to inform CPPSPI results shown in the Chapter 4.

6.5 Conclusions

Three dynamic friction oblique impact experiments were conducted, including 2 on polyurethane and 1 on epoxy. Expected initial combined stress states were attained in all cases followed by reverberations off the rear free surface incrementally releasing in stress, observable in the normal velocity. Epoxy exhibited what is believed to be prominent viscoelastic relaxation behavior(s) not seen in corresponding polyurethane results. Coefficients of friction, assumed to at least be a lower bound of kinetic regime, are calculated to be $\mu = 0.18$ for polyurethane (averaged from both shots) and $\mu = 0.50$ (initial) or $\mu = 0.42$ (average including

relaxation) for epoxy. μ values are now shown in terms of $\frac{\tau}{P}$, where as previously values have been in terms of the more directly measured ratio $\frac{\tau}{\sigma}$.

Literature provides some key insights to serve as a check. The relations proposed to govern surface friction, informed by experiment and detailed in Chapter 2, show polymer-substrate coefficients-of-friction to be very pressure dependent following $\mu = \frac{\tau_0}{P} + \alpha$ (eq. 2.31). However, as is evident in the formulation, this approaches some empirically observed asymptote, which for many polymers has been observed to be an $\alpha \approx 0.1 - 0.2$ [117]. Polyurethane μ-values are in good agreement with these previous observations, while epoxy values are notable much higher due to viscoelastic nature of the polymer stress response.

DFI μ values are now compared to shear-pressure slopes found in CPPSPI experiments, with the intention of gleaming some insight on the role of adhesion. Table 6-2 compares friction coefficients with shear/normal stress slopes found in CPPSPI experiments.

Table 6-2: Tabulated shear slope values for interface dynamic friction and thin-film polymer CPPSPI experiments. Both sets of slopes are shown with respect to pressure as to be comparable.

Material	CPPSPI $\frac{d\tau}{dP}$, a	Interface $\frac{d\tau}{dP}$, μ	Δ
PUR-AVE	0.12	0.18	0.06
Epoxy	0.17	0.42	0.25

As described in Chapter 4, if the shear behavior observed in CPPSPI testing is that of the interface, it is assumed to take the form of $\tau = \mu P + \sigma_{adh}$ (eq. 4.10). This is in contrast to bulk polymer shear strength takes the different (though similar) form $\tau = aP + \tau_0$. DFI experiments remove the role of chemical adhesion, as the polymers are not molded to aluminum anvils (substrates) *a priori*, and as such provide an value for μ. Using this, a potential value for adhesion σ_{adh} can be

calculated. If σ_{adh} is distinct from τ_0 (from low strain-rate testing) then potential implications of adhesion in oblique impact experiments may be more conclusively discussed.

Table 6-2 shows there is slight a difference between measured slopes, and so a different intercept value (σ_{adh}) is expected. However, it is at this point that uncertainty becomes critical. Uncertainty for normal and shear stress values are 1.5 and 12 percent respectively. Propagating this through the calculation of their ratio results in a uncertainty of 0.12 for both "a" slope and μ values. This being the case, while slope values would suggest an inherent difference in behavior uncertainty in the data prevents the role of adhesion from being quantified and isolated from other phenomena.

Despite this limitation, a key qualitative observation may be made. In most CPPSPI experiments (10 of 13), some adhesive bond remained and was apparent post-mortem. This was established by attempting to separate the anvils after experimentation and having to physically peel them apart. As such, it can be speculated that adhesion is present between the interfaces. If adhesion were significantly weaker than that of the bulk polymer material, the interface would yield and not the bulk material. So while not quantified, the value of adhesive strength may be constrained as near to or greater than the strength of the polymer itself.

Left for future work, this discussion could be improved by endeavoring to reduce measurement uncertainty and/or removing the effects of adhesion by testing non-molded thin polymer specimens in the same CPPSPI configuration. The latter approach would have the additional benefit of being consist in stress loading.

CHAPTER 7

SIMULATING PRESSURE-DEPENDENT YIELD OF POLYMERS

7.1 Introduction

To demonstrate the applicability of experimental results, into the CTH hydrocode to establish whether the software could accurately recreate observed behavior. For each polymer, Hugoniot information was incorporated in a Mie-gruneisen equation-of-state while yield data (mapped onto von Mises stress - pressure space) was used to fit a simple pressure-dependent constitutive model. Resulting free longitudinal and transverse free surface particle velocity profiles were compared directly to experiment, while the coalescence of shear/normal stress responses over multiple simulations were plotted against experimental yield surfaces.

While surface roughness implications were not observed (or beyond measurement precision), their theoretical effect is of interest. Specifically, it is useful to define a point at which such characteristics would be observable. Facilitating this, CTH was further utilized to perform series of mesoscale simulations which sought to resolve surface roughness and its effects on longitudinal and transverse wave dynamics.

7.2 Computational Methodology

7.2.1 Overview

The chosen computational tool implemented in this investigation was CTH, developed by Sandia National Laboratories [27]. CTH is an Eulerian hydrocode capable of second order accurate, explicit solutions specifically developed around shock-physics and related wave dynamics. While the term hydrocode implies the

modeling of only hydrodynamic material behavior, CTH employs a significant library of material constitutive models to incorporate ever-important strength contributions which dominate at lower stress/pressure regimes. While Eulerian, and as such not well suited to incorporate contact/friction models, the infrastructure for predicting wave dynamics along with material strength make CTH well suited to confront problems in treating high strain-rate combined pressure-shear load deformation.

Capable of 1D, 2D-rectangular, 2D-cylindrical, and full 3D problems, for a general geometry and imposed initial conditions, a finite volume mesh approximates behavior based on the descretization of the conservation equations for mass, momentum and energy - whose three-dimensional differential forms are presented in eqs. 7.1 - 7.3 **??**.

$$\frac{\partial \rho}{\partial t} = -\rho \nabla \cdot \vec{v} \tag{7.1}$$

$$\rho \frac{\partial \vec{v}}{\partial t} = -\nabla P - \nabla \cdot [\vec{\vec{\sigma}} + \vec{\vec{Q}}] \tag{7.2}$$

$$\rho \frac{\partial E}{\partial t} = -P \nabla \cdot \vec{v} - [\vec{\vec{\sigma}} + \vec{\vec{Q}}] : \nabla \vec{v} \tag{7.3}$$

where ρ is again density, t is time, $\vec{v}$ is the generalized velocity vector, P is thermomechanical pressure, $\vec{\vec{\sigma}}$ is the second order deviatoric stress tensor, E is internal energy, and $\vec{\vec{Q}}$ is an artificial viscosity term. $\vec{\vec{Q}}$ is a specific numerical smoothing treatment for discontinuous gradients in material properties, such as shock waves, which would otherwise produce instabilities. While CTH is fundamentally Eulerian in nature, each solution iteration has a Lagrangian half-step in which the mesh is allowed to deform - after which it is *re-mapped* onto the original mesh. This is useful as it increases CTH's ability to track surfaces and mass advection over other

more traditional approaches often seen in computational fluid dynamics applications.

A key advantage, not to be overlooked, is the ability to run CTH in parallel. As such large scale problems may be solved relatively quickly, limited of course to the users own available computational power. The processor demand for any problem is readily calculable based only on mesh resolution, as shown for a two-dimensional problem in eqs. 7.4 - 7.6.

$$N_x = \frac{L_x}{\Delta x} \tag{7.4}$$

$$N_y = \frac{L_y}{\Delta y} \tag{7.5}$$

$$N_{processors} = \frac{N_x N_y [cells]}{35,000[\frac{cells}{processor}]} \tag{7.6}$$

N_x or $N_y$is number of cells in a given dimension based the total domain length L_{xory} and the specified mesh cell size $\Delta x or \Delta y$. The most efficient number of processors for a parallel operation,$N_{processors}$, is then simply the total number of cells in the domain, $N_x \cdot N_y$, divided a suggested (rule-of-thumb) maximum of around 35,000 cells per processor [118].

7.2.2 CTH Input for CPPSPI

To setup the computational investigation, a two dimensional representation of the experimental geometry was implemented into CTH. Two-dimensions was deemed sufficient given impact imposes only an longitudinal and transverse velocity condition on the impact face with negligible skew observed. More so, polymers were mixed and molded with no preference given to orientation and so both

epoxy and polyurethane are assumed to behave isotopically with any crosslinking and viscoelastic effects being spatially homogeneous.

Geometry thicknesses were nominally 1.0, 0.4, 0.045, and 0.7 cm for the impactor, front anvil, polymer specimen, and rear anvil respectively - presented with the ”x” direction set as orthogonal to the target surfaces. These are specified as nominal given thickness were varied slightly to match experiment values measured to greater precision. The impactor was given velocity initial condition in both the x and y axis to simulate transverse velocity - with components dictated by shot velocity and oblique angle. For example, a 96.7 m/s shot velocity experiment at 20 deg would have imposed impactor velocity components of 90.9 and 33.1 m/s. It is worth noting that CTH is formulated in terms of a set unit system based on grams, seconds, cm, and dynes (for force). To ensure fidelity with regard to edge effects, lateral diameters were also reflective of experiment with and impactor diameter of 5 cm and a consistent target diameter of 7 cm - set concentric to one another. Spacers are places on the outer lateral edges of the polymer specimen to mimic a gasket, as was used for containment/spacing in practice. A representative CTH domain is shown in Figure 7-1 including imposed initial velocity in both the x and y direction.

A resolution study was not performed on the provided setup. Instead, mesh size was constrained to place at least 30 cells through the thickness of the specimen - a number generally accepted to provide ”good” resolution. With a maximum target thickness of 0.05 cm, a flat mesh of 0.0015 cm/cell was implemented.

Each material within the geometry requires parameters to inform both thermodynamic and material strength behavior. These can be selected from a material library of various constitutive and equation-of-state models. Herein, impactor, front anvil, and rear anvil materials are modeled as 7075-T6 aluminum with an elastic perfectly-plastic von-Mises (EPPVM) strength and Mie-Gruneisen

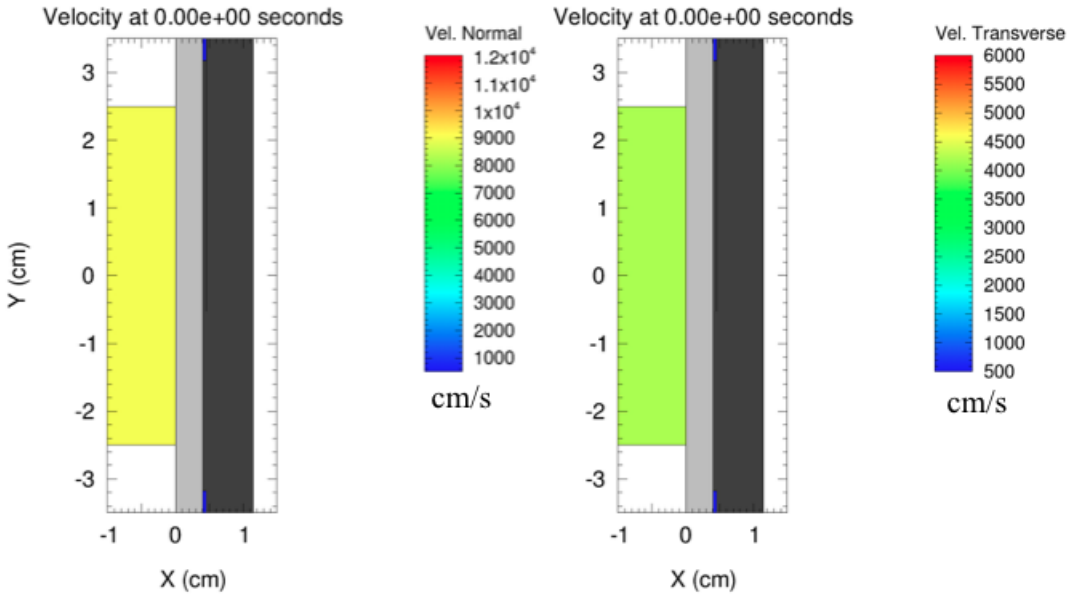

Fig. 7-1. The domain and relevant geometries for a simulated CPPSPI experiment, shown in with longitudinal and transverse velocity contours which show imposed initial conditions.

equations-of-state both readily available in the CTH libraries in conjunction with some user input. The gasket material was simulated to be PMMA with a Johnson-Cook constitutive model and also a Mie-Gruneisen EOS.

Of primary interest was the implementation of empirical data observed in the aforementioned experimental investigation into the polymers simulated here. Hugoniot parameters for polyurethane and epoxy respectively, discussed in Chapter 3, were inserted into a user-based linear Mie Gruneisen EOS. Polymer yield was mimicked using the pressure-dependent *Geo-Yield* formulation, shown in eq. 7.7.

$$Y(P) = Y_{max} + (Y_0 - Y_{max})exp(\frac{dY}{dP} * \frac{P}{Y_0 - Y_{max}}) \tag{7.7}$$

As the name implies, this was originally developed for earth materials like sand and soils which exhibit similar behave (though notably due to different mechanisms). This requires the von-Mises yield strength versus pressure slope $\frac{dY}{dP}$ ex-

trapolated between a minimum strength Y_0 and maximum threshold Y_{max} - all of which were taken from Chapter 4.

With materials fully defined in terms of geometry and governing thermo-mechanical response, the only remaining simulation constraint to define is that of the spatial boundaries. Termed "condition 1" in CTH, a sound speed based transmitting condition is set in all conditions which simulates an infinite medium. As such, the anvil/spacer edges are assumed to continue indefinitely, the impactor acts as infinitely thick, and the void seen after the free surface is likewise endless. The only apparent sacrifice in this assumption is that no longitudinal wave release will be seen coming from the rear of the impactor. However, edge release originating from the diameter of the impact site is known (through experimental observation) to occur prior to this being a concern, and so this was deemed acceptable. The end result of these collective inputs is an oblique impact imparting both longitudinal and shear stress waves into the target. This can be seen as spatial velocity profiles shown in Figure 7-2.

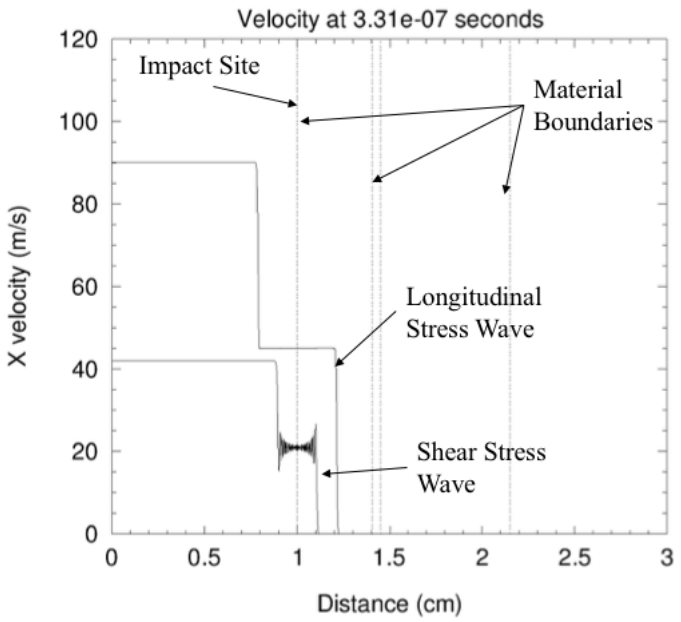

Fig. 7-2. One-dimensional spatial velocities showing initial propagation of longitudinal and shear stress waves into the target and back into the impactor.

7.3 Results and Discussion

Given the discussed computational input a series of CTH simulations were conducted for both polyurethane and epoxy of impact velocities ranging from 30 to 150 m/s. Resulting free surface particle velocity profiles in both normal and transverse directions are akin the PDV measurements taken from experiment. These were measured using a Lagrangian tracer point placed at the concentric center for the rear anvil free surface, corresponding to where PDV measurements are made experimentally. A series of profiles are presented in Figure 7-3

Profiles show the characteristic reverberation behavior expected of a low impedance specimen confined by high impedance mediums. All stress waves are seen to arrive at the free surface at the same time. This provides confirmation that loading is indeed remaining elastic within the simulated anvil materials. To calibrate these results, CTH inputs are adjusted to more precisely match experimental

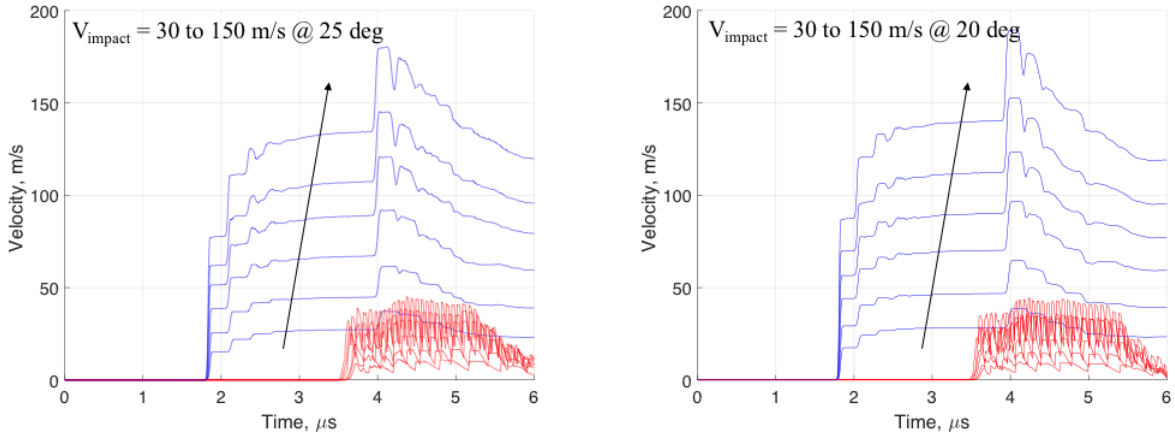

Fig. 7-3. Simulated free surface velocity profiles shown spatially for both (left) polyurethane and (right) epoxy.

specifications and then compared directly against PDV histories - as displayed in Figures 7-4 and 7-5.

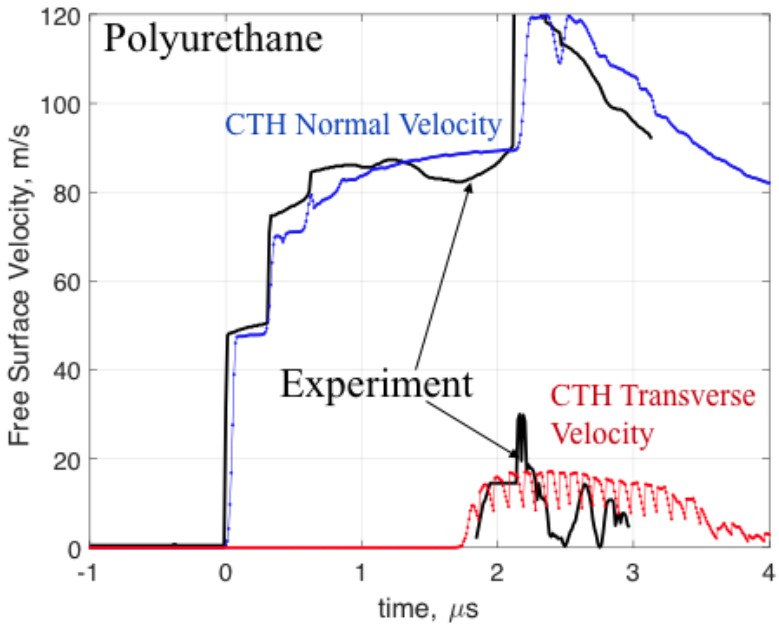

Fig. 7-4. A comparison of experimental and simulated rear free surface velocities for a CPPSPI test conducted on polyurethane - impact velocity of 99.5 m/s at a 25 deg angle of obliquity.

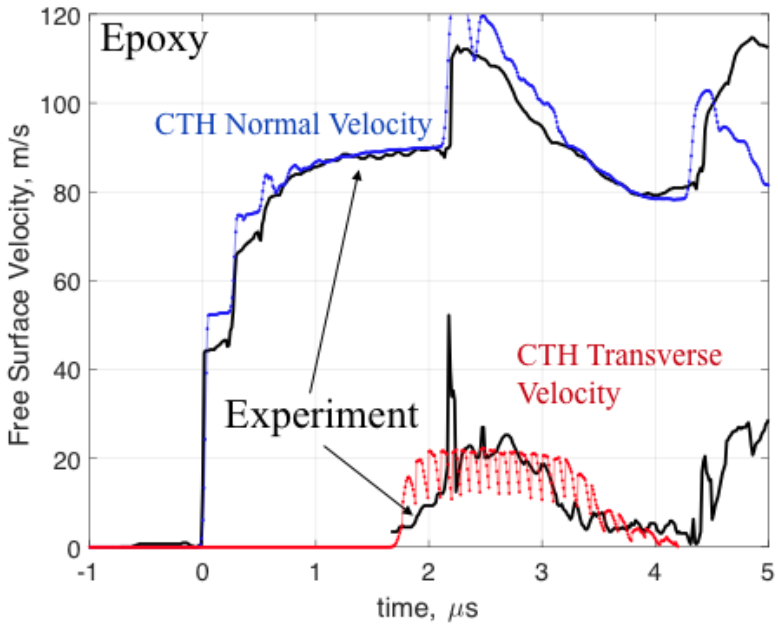

Fig. 7-5. A comparison of experimental and simulated rear free surface velocities for a CPPSPI test conducted on epoxy - impact velocity of 96.7 m/s at a 20 deg angle of obliquity.

In both cases, simulation is in good agreement with experimental observations. Considering first the longitudinal histories, polyurethane is well approximated with a noticeable deviation after around 1.5 μs at the equilibrium state, at which point the test profile "dips". Epoxy is similarly over-estimated by simulation, except primarily within the context of reverberation states. It is hypothesized that this is due to the simplicity of employed models not taking into account the transient mechanisms of visco-elasticity/plasticity (relaxation, creep, etc.). Given such phenomena cannot be isolated from other possible contributors, such as spatial heterogeneity in the polymer micro-structure, this is far from conclusive.

Debateably the most apparent mismatch between experiment and CTH is the high frequency oscillation seen in simulated transverse velocity profiles. This is numerical in nature and caused by two related issues; Gibb's phenomena and the robustness of artificial viscosity. Gibb's phenomena is the formal term for nu-

merical instability which occurs when approximating a discontinuous property . The more terms used in approximation, the more this type of error is reduced (asymptotically approaching zero). As such, it is mesh dependent and higher resolution would reduce (but not eliminate its presence). While Gibb's phenomena specifically refers to this issue in the context of Fourier series approximations, the behavior persists anywhere numerics treats a discontinuity [119]. von-Neumann mathematically derived an *artificial viscosity* term to implement into conservation equations (mentioned previously) which in concept smooths out this behavior by introducing non-physical dissipative "friction", denoted $\vec{\vec{Q}}$ in eqs. 7.1 - 7.3 **??**. $\vec{\vec{Q}}$ is a second order tensor and as such has differing elements associated with the longitudinal versus transverse directions. With these concepts considered, it is hypothesized further tuning of artificial viscosity with respect to the transverse stress waves would greatly reduce observed oscillations. Despite this, the overall average of the simulated shear state is still reasonable and in good agreement with data.

With some confidence in computational results, given initial benchmarking, a computational yield surface can be calculated using an accumulation of all simulated combined stress states. Figure 7-6 presents a final comparison of CTH generated yield behavior against experimental data. The slopes of shear stress dependence on confinement are in good agreement, which implicitly demonstrates the usefulness of such results.

A specific caveat arises when considering the possible failure cap found in polyurethane. This is not captured in the geo-yield constitutive model and instead CTH allows for ever increasing strength. Maximums in von-Mises yield strength were included as 450 (PUR) and 650 MPa (epoxy), for which CTH imposes an asymptotic approach, taken from the possible cap threshold for PUR (in $\sigma_{12} - \sigma_{11}$ space) and arbitrary value for epoxy outside the probed experimental range. Based

on simulated results these were not exceeded over the range of simulated impact conditions and so not strength ”flat-line” or drop was observed. A logical next step for modeling, considered for future work, then becomes the implementation of failure cap like behavior within a constitutive model.

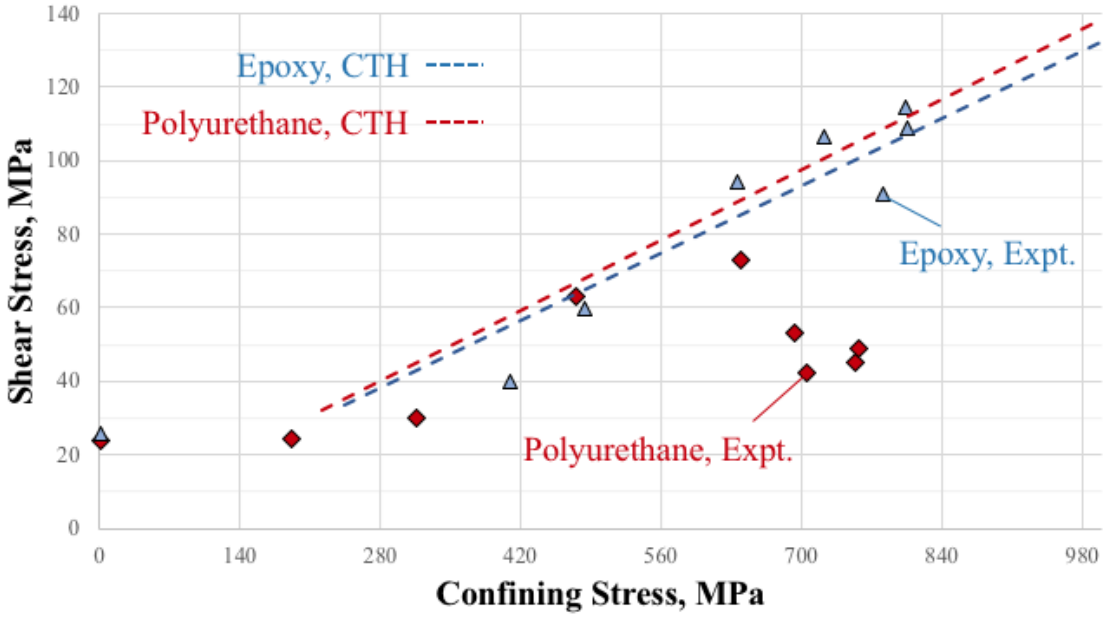

Fig. 7-6. Computationally generated yield surfaces for both polyurethane and epoxy plotted against experiment values.

7.3.1 Mesoscale Simulations of Roughness

As an additional supplement to experimental results, further simulations were conducted in an effort to resolve micron-scale surface roughness features and their theoretical implications on pressure-shear wave propagation. Experiments saw no observable trend with respect of the bulk response, and simulations were intended to corroborate this numerically. Given the scale of surface roughness asperities, mesoscale simulations were conducted, isolating a small portion of the previously presented bulk domain, ensuring asperities were resolved and the problem remained numerically tractable. Figure 7-7 shows the computational domain proposed for mesoscale simulations.

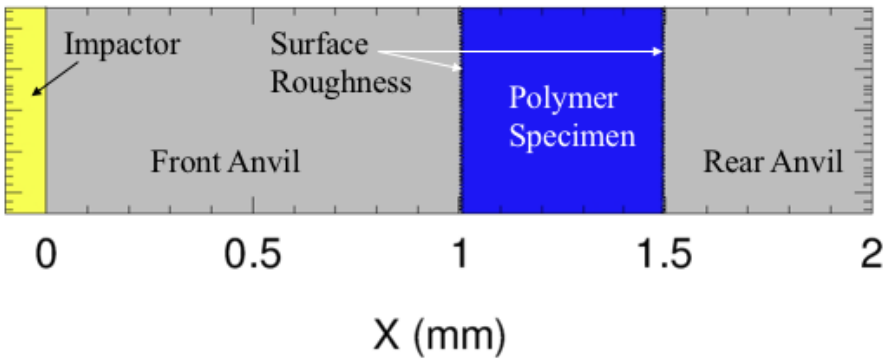

Fig. 7-7. The CTH domain utilized for mesoscale simulations used to resolve the effect of surface roughness on pressure-shear wave propagation. Only a portion of the domain is shown in the x-direction.

The total domain had dimensions of 8.7 x 0.5 mm, only a portion of the x-direction is shown Figure 7-7 to better present near-polymer features. The complete thickness of the rear anvil was simulated as to allow proper spacing of wave arrivals on the rear free surface. To reduce computation time, the front anvil was made artificially thinner (1 mm instead of 4 mm). To keep in agreement with ex-

periment, this required the transverse velocity initial condition be delayed so that proper separation between normal and shear stress waves were maintained. This delay was calculated using eq. 7.8.

$$t_{delay} = ({x^{sim}}_{FA} - {x^{expt}}_{FA})(\frac{1}{C_S} - \frac{1}{C_L}) \tag{7.8}$$

where ${x^{sim}}_{FA}$ is the computational front anvil thickness (1 mm), ${x^{expt}}_{FA}$ is the experimental front anvil thickness (nominally 4 mm), and C_L or C_S are the front anvil elastic sound speeds.

To mimic surface roughness, periodic triangle ridges were implemented along either anvil in contact with the polymer specimen. These are shown in Figure 7-8. Roughness was characterized by a single length value which was equal to both the spatial period between repetition (wavelength) and asperity size. To investigate the effect of this idealized roughness, the characteristic length was set to values of 0 (no roughness), 10, 50, and 100 μm. These were the smallest feature necessary to resolve, and so a mesh size of 1 μm/cell was used to ensure at least 10 cells through the thickness of every asperity. This was a flat mesh maintained throughout the entire domain.

Boundary conditions included a "condition 1" semi-infinite medium assumption for the impactor (x-left boundary), as well as for the void on the x-right boundary. The domain is representative of only a small vertical (y) slice of the bulk target. As such, surface roughness geometry was set to continue infinitely in either y-direction, simulated using a periodic "condition 6" assumption. Implemented EOS and strength models were consistent with those used in bulk-scale simulations, detailed in the previous section.

A key aspect in these simulations is mixture model. Given the Eulerian basis for CTH, contact is not directly simulated. Instead material interfaces will

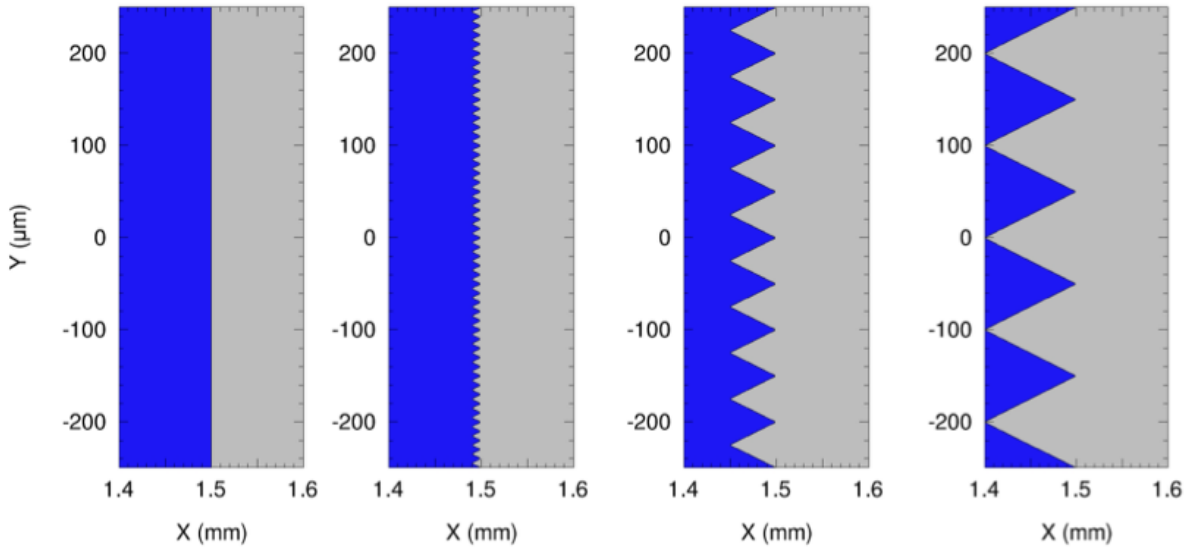

Fig. 7-8. A view of the idealized mesoscale surface roughness asperities implemented on the front and rear anvil surfaces in contact with the polymer specimen. These were set to characteristic length values of 0 (no roughness), 10, 50, and 100 μm.

lie within a single mesh cell, and material interactions (cell strength) are approximated based a library of possible mixture rules. Three primary formulations are utilized; volume fraction weighted material strength (Mix 1), normalized volume fraction weighted material strength (Mix 3), and zero strength in mixed cells (Mix 5) [118]. These are presented mathematically in eqs. 7.9 7.10 and 7.11;

$$Y = \sum_{n=1}^{i} \Phi_i Y_i \tag{7.9}$$

$$Y = \frac{\sum_{n=1}^{i} \Phi_i Y_i}{\sum_{n=1}^{i} \Phi_i} \tag{7.10}$$

$$Y = 0 \tag{7.11}$$

where Y is the calculated total strength of a mesh cell, Φ_i is the volume fraction for a material "i" within a cell, and Y_i is the strength the same material "i" within the

cell. Mixes 1 and 3 (eqs. 7.9 and 7.10) imply some interface strength exists (adhesion). In contrast, Mix 5 assumes no inherent interface shear strength. A series of simulations were run with each rule in place for a more comprehensive comparison of results. Mix 3 is generally cited as yielding the best results [118], at least on a bulk scale, and notably was the mix rule implemented for bulk simulations presented previously.

With the computational setup now defined, simulations may be conducted and free surface velocity profiles may be produced and evaluated for any changes due to roughness. Traces were taken from an average of Lagrangian tracer points place on the rear anvil free surface. Figures 7-9, 7-10, and 7-11 compare simulated normal and transverse velocity profiles containing surface roughness of increasing. Each figure represents simulations conducted using a different mixture rule, and profiles have been arbitrarily spaced in time to allow for better comparison. Simulations shown were conducted with epoxy, though results are consistent in the case of polyurethane.

First consider only normal velocity profiles. The ”no roughness” cases for each figure are identical to bulk simulations preformed previously. This serves as good check that, despite the smaller-scale domain, the same results are reproducible given the same interface conditions (mixture rule). Now increasing in surface roughness size, a qualitative trend arises as the reverberation states become more distorted, and even attain higher plateaus prior to equilibrium. This is not unexpected. Pressure wave propagation through asperities causes wavelets to interact and superimpose which would distort wave magnitudes at the free surface. The final equilibrium value, however, does remain consistent as the wavelets would average out over time and the final state is left, governed by the conservation of momentum.

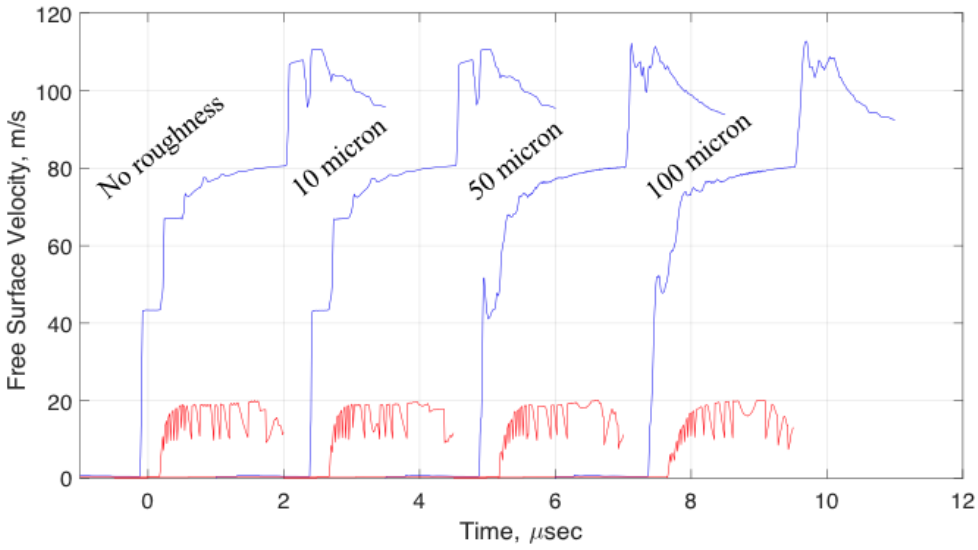

Fig. 7-9. CTH simulated normal and transverse velocity profiles representative of the conducted CPPSPI experiments. Idealized surface roughness has been implemented with asperity thicknesses of 0, 10, 50, and 100 μm. Results utilized a Mix 1 rule for material interfaces.

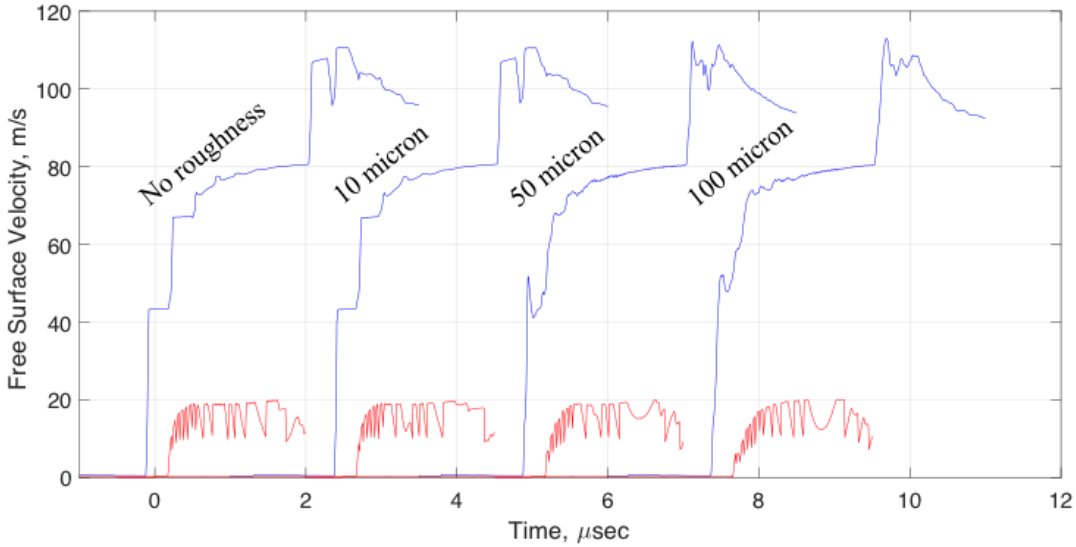

Fig. 7-10. CTH simulated normal and transverse velocity profiles representative of the conducted CPPSPI experiments. Idealized surface roughness has been implemented with asperity thicknesses of 0, 10, 50, and 100 μm. Results utilized a Mix 3 rule for material interfaces.

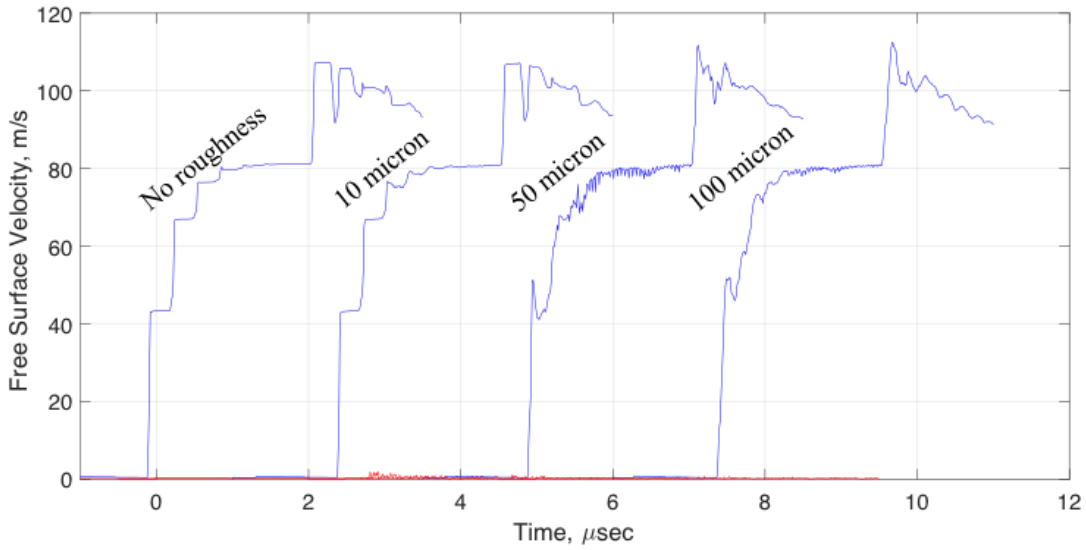

Fig. 7-11. CTH simulated normal and transverse velocity profiles representative of the conducted CPPSPI experiments. Idealized surface roughness has been implemented with asperity thicknesses of 0, 10, 50, and 100 μm. Results utilized a Mix 5 rule for material interfaces.

Few discrepancies are identifiable within transverse velocity profiles. Considering only Mix 1 and 3 cases, "no roughness" cases are again in good agreement with bulk simulation. No change is apparent in transverse equilibrium states regardless of roughness, and the only real trend would appear to be a overall increase in wave rise time. This is only slight, but suggests shear waves are being "smeared out" (dissipated slightly) throughout their propagation through the rear anvil. This too could be attributed to small wavelet interactions, in this case destructively interfering.

The Mix 5 case for transverse velocities is the most apparent outlier. No transverse velocity is seen at the rear surface, inferring shear stress could not propagate across the specimen. This is not unexpected as Mix 5 enforces no shear transmission across the interface. Despite being unrealistic when compared to experiment, this result does lend itself to the discussion of adhesion presented in previous chapters. If adhesion were less than polymer strength, or non-existent,

experimental transverse velocity profiles would be less in magnitude. Simulations best matching experimental profiles are those implemented with polymer strength as the weakest feature, suggesting that experiments are indeed measuring polymer yield and not that of the interface.

7.4 Conclusions

In review, bulk and mesoscale simulations were conducted in CTH in an attempt to reproduce experiment normal and transverse velocity profiles. This was done to both demonstrate the applicability of experimental results and to supplement experiments with potential insights from the contrast of numerical against empirical observations. Both strength and EOS information into CTH, and the resulting velocity profiles were in good agreement with experiment - despite the approximate nature of the proposed yield surfaces. This is particularly useful given the simplicity the model as strength only considers pressure dependence and no other viscoelastic effects. However, as a cautionary note, it is believed that such agreement would not extend to modeling the same polymers if sufficiently different operating conditions are expected. If the polymers are processed differently or are exposed to drastically higher temperatures (¿90 deg-C), the viscoelastic reponse and would not be reproducible.

Mesoscale simulations were able to resolve idealized surface roughness features placed on the anvil walls in contact with the polymer specimen. Based on simulation results, no observed changes would be identifiable in bulk velocity profiles based on surface roughness between 0 and 10 μm (the allowed variation in experiment). However, at higher roughnesses, surface asperities do result in the distortion of the normal velocity reverberation states and a slight increase in rise time of the transverse wave. Comparing the effect of material mixture rules for cell strength shows simulations are in good agreement with experiment when in-

terface strength is included (polymer-anvil). In contrast, if no interface strength (no adhesion) is present then no shear transmission would occur across the polymer specimen, regardless of roughness characteristics. This lends to previous ideas that adhesion is present and is at least as strong (or stronger) than the polymer itself - as in simulations the polymer strength is the weakest feature.

CHAPTER 8

CONCLUDING REMARKS

An experimental and computational investigation was conducted to characterize the response of two thermosetting polymers, fully dense polyurethane and epoxy, at high strain-rate undergoing combined normal and shear stress loading. A series constant-pressure pressure-shear plate impact (CPPSPI) experiments were conducted, inducing normal and shear stresses up to 800 and 120 MPa respectively at strain-rates of $10^5 s^{-1}$. In conjunction with dynamic friction oblique impact tests and low strain-rate shear testing, yield surfaces were mapped for each polymer demonstrating at noticeable shear strength dependence on confinement conditions. Not withstanding for epoxy, polyurethane showed evidence of a failure cap after after confinement stresses in excess of $\sim$650 MPa. Given the varied loading conditions subjected by the different constant-pressure pressure-shear plate impact, dynamic friction impact, and low strain-rate tests, resulting yield surfaces were considered approximate. Strength behavior across loading strain-rate regimes was compared, and while each polymer demonstrated some strengthening with increased strain-rate it was observed that pressure-dependence had a much more dominate role.

Dynamic friction impact experiments were performed which facilitated the quantification of coefficients of friction between polyurethane or epoxy and a 7075-T6 aluminum tribological pair. Polyurethane and epoxy were found to have μ-values of 0.18 and 0.42 respectively, where $\mu = \frac{\tau}{P}$. The value for epoxy was substantially higher due to viscoelastic relaxation in stress activated by some unknown mechanism, speculated to be either incomplete polymer curing or thermal transition in the epoxy moduli. Dynamic friction experiments also removed the role of adhesion as a strength contributor, unlike CPPSPI experiments in which

polymers were molded (adhered) to aluminum anvils. As such comparing dynamic friction results to those of CPPSPI was presented as a methodology by which to evaluate the adhesion strength. However, uncertainty in stress magnitude measurements were to high to allow for any conclusive quantification. Despite this, based on the qualitative survival of adhesive bonding after experimentation, interface strength was constrained in value to be close in magnitude to that of bulk polymer strength if not greater.

Strength and Hugoniot behavior, acquired in preliminary uniaxial impact testing, were implemented into CTH through Mie Gruneisen equation-of-state and Geo-yield constitutive parameters. Simulations representative of conducted experiments showed good agreement with data, and demonstrate the usefulness of performed mechanical characterization with respective to improved predictive capability. Mesoscale simulations, resolving idealized surface roughness of varying magnitude, suggest no difference would be observable on the bulk scale. More so, mesoscale simulations in which polymer strength was the weakest feature is in best agreement with experiment results which corroborates the previous constraint that adhesion is as strong or stronger than the bulk polymer itself - as such the measured yield strength quantified in the experimental yield surfaces is expected to be that of the polymer materials.

REFERENCES

[1] "Polyurethane - wikipedia," https://en.wikipedia.org/wiki/Polyurethane, (Accessed on 01/30/2019).

[2] "Epoxy - wikipedia," https://wikivisually.com/wiki/Epoxyprepolymerchemicalstructure (Accessed on 01/31/2019).

[3] N. P. Cheremisinoff, *Condensed encyclopedia of polymer engineering terms*. Butterworth-Heinemann, 2001.

[4] A. D. Mulliken and M. C. Boyce, "Mechanics of the rate-dependent elastic-plastic deformation of glassy polymers from low to high strain rates," *International Journal of Solids and Structures*, vol. 43, no. 5, pp. 1331–1356, 2006.

[5] J. Roetling, "Yield stress behaviour of polymethylmethacrylate," *Polymer*, vol. 6, no. 6, pp. 311–317, 1965.

[6] Jacob, *Intermolecular and Surface Forces, 2nd ed.;Academic Press: London, 1992*, 1098-6596.

[7] "Shockcompressionmoleculardynamics.ppt," https://reedgroup.stanford.edu/references (Accessed on 02/04/2019).

[8] "(12) (pdf) mixed stabilized finite element methods in nonlinear solid mechanics. part iii: Compressible and incompressible plasticity," https://www.researchgate.net/publication/270163624, (Accessed on 02/05/2019).

[9] B. Bhushan, *INTRODUCTION TO TRIBOLOGY*. Wiley, 2013.

[10] S.-w. Measurements and L. M. Barker, "Shock-wave studies of pmma, fused silica, and sapphire," *Journal of Applied Physics*, vol. 41, no. 10, p. 4208, 1970.

[11] "Photon doppler velocimetry (pdv) — impulse manufacturing laboratory," https://iml.osu.edu/capabilities/photon-doppler-velocimetry-pdv, (Accessed on 04/24/2019).

[12] O. T. Strand, D. R. Goosman, C. Martinez, T. L. Whitworth, and W. W. Kuhlow, "Compact system for high-speed velocimetry using heterodyne techniques," *Review of Scientific Instruments*, vol. 77, no. 8, 2006.

[13] G. Swallowe, "Mechanical Properties and Testing of Polymers: An A-Z Reference," vol. 3, 1999.

[14] D. Van Krevelen, "Properties of Polymers," *Physical Sciences and Engineering Division*, 1990.

[15] A. Mix and A. Giacomin, "Standardized polymer durometry," *Journal of Testing and evaluation*, vol. 39, no. 4, pp. 696–705, 2011.

[16] M. T. Shaw and W. J. MacKnight, "Introduction to Polymer Viscoelasticity," 2005.

[17] T. A. Osswald and G. Menges, "Materials Science of Polymers for Engineering," 1996.

[18] J. C. Millett, N. K. Bourne, and G. T. Gray, "The response of polyether ether ketone to one-dimensional shock loading," *Journal of Physics D: Applied Physics*, vol. 37, no. 6, pp. 942–947, 2004.

[19] V. Kargin, G. Andrianova, I. Y. Tsarevskaya, V. Goldanskii, and P. Yampolskii, "Structural phenomena in polymers arising at low temperatures and by the action of high forces," *Journal of Polymer Science Part A-2: Polymer Physics*, vol. 9, no. 6, pp. 1061–1081, 1971.

[20] P. Kelly, "Yield criteria in three dimensional plasticity," *Solid Mechanics Part II*, pp. 259–279, 2008.

[21] Z. Rosenberg and Y. Partom, "Accounting for the hugoniot elastic limits of polymers by using pressure-dependent yield criterion," *Journal of Applied Physics*, vol. 76, no. 3, pp. 1935–1936, 1994.

[22] A. S. Abou-Sayed and R. J. Clifton, "The oblique-plate impact experiment," *Experimental Mechanics*, vol. 16, no. 4, pp. 127–132, 1976.

[23] T. Jiao, R. J. Clifton, and S. E. Grunschel, "Pressure-sensitivity and tensile strength of an elastomer at high strain rates," *AIP Conference Proceedings*, vol. 955, pp. 707–710, 2007.

[24] ——, "Pressure-sensitivity and constitutive modeling of an elastomer at high strain rates," *AIP Conference Proceedings*, vol. 1195, pp. 1229–1232, 2009.

[25] V. Prakash and N. Mehta, "Uniaxial compression and combined compression-and-shear response of amorphous polycarbonate at high loading rates," *Polymer Engineering and Science*, vol. 52, no. 6, pp. 1217–1231, 2012.

[26] M. A. Irfan and V. Prakash, "Time resolved friction during dry sliding of metal on metal," *International Journal of Solids and Structures*, vol. 37, no. 20, pp. 2859–2882, 2000.

[27] J. M. McGlaun, S. L. Thompson, and M. G. Elrick, "Cth: A three-dimensional shock wave physics code," *International Journal of Impact Engineering*, vol. 10, no. 1-4, pp. 351–360, 1990.

[28] H. L. Fisher, "Vulcanization of rubber vulcanization of rubber," *Industrial & Engineering Chemistry*, vol. 31, no. 11, pp. 1381–1389, 1939.

[29] H. Staudinger, "Über die konstitution des kautschuks (6. mitteilung)," *Berichte der deutschen chemischen Gesellschaft (A and B Series)*, vol. 57, no. 7, pp. 1203–1208, 1924.

[30] W. Wake, "Theories of adhesion and uses of adhesives: a review," *Polymer*, vol. 19, no. 3, pp. 291–308, 1978.

[31] M. A. Daniel 1980-, "Polyurethane binder systems for polymer bonded explosives [electronic resource] / merran a. daniel," 2006.

[32] T. J. Horn and O. L. Harrysson, "Overview of current additive manufacturing technologies and selected applications," *Science progress*, vol. 95, no. 3, pp. 255–282, 2012.

[33] A. Renner and K. P. Michaelis, "Thermoplastic resins, polyquats, and membranes based on epoxies," *Journal of Polymer Science: Polymer Chemistry Edition*, vol. 22, no. 1, pp. 249–262, 1984.

[34] M. Szycher, *Szycher's handbook of polyurethanes*. CRC press, 2012.

[35] "Pma :: Consumer information," http://www.pmahome.org/main/polyurethane101/cor
information/, (Accessed on 01/30/2019).

[36] E. Sharmin and F. Zafar, "Polyurethane: an introduction," in *Polyurethane*. InTech, 2012.

[37] F.-U. Rehman, "Synthesis and characterization of speciality polyurethane elastomers," Ph.D. dissertation, UNIVERSITY OF AGRICULTURE, FAISALABAD PAKISTAN, 2010.

[38] "Polyurethanes," http://www.essentialchemicalindustry.org/polymers/polyurethane.ht
(Accessed on 01/30/2019).

[39] C. Craver and C. Carraher, *Applied polymer science: 21st century*. Elsevier, 2000.

[40] H. Lee and K. Neville, "" book review-handbook of epoxy resins"," *Industrial & Engineering Chemistry*, vol. 59, no. 9, pp. 16–17, 1967.

[41] F.-L. Jin, X. Li, and S.-J. Park, "Synthesis and application of epoxy resins: A review," *Journal of Industrial and Engineering Chemistry*, vol. 29, pp. 1–11, 2015.

[42] R. B. Seymour and C. E. Carraher, "Structure-Property Relationships in Polymers," 1984.

[43] R. Christensen, *Theory of viscoelasticity: an introduction*. Elsevier, 2012.

[44] D. Kaelble, "Dynamic and tensile properties of epoxy resins," *Journal of Applied Polymer Science*, vol. 9, no. 4, pp. 1213–1225, 1965.

[45] S. Turner, *Mechanical testing of plastics*. Godwin, 1983.

[46] F. Ramsteiner and T. Armbrust, "Fatigue crack growth in polymers," *Polymer Testing*, vol. 20, no. 3, pp. 321–327, 2001.

[47] D. Thomas and S. Turner, "Experimental technique in uniaxial tensile creep testing, in" testing of polymers"," *InstersCTence, New York*, 1969.

[48] M. L. Williams, R. F. Landel, and J. D. Ferry, "The temperature dependence of relaxation mechanisms in amorphous polymers and other glass-forming liquids," *Journal of the American Chemical society*, vol. 77, no. 14, pp. 3701–3707, 1955.

[49] W. D. Callister, D. G. Rethwisch *et al.*, *Materials science and engineering: an introduction*. John wiley & sons New York, 2007, vol. 7.

[50] G. Pertici, "The effect of molecular structure on the properties of biomedical polymers," in *Durability and Reliability of Medical Polymers*. Elsevier, 2012, pp. 30–48.

[51] M. Mullins, D. Liu, and H.-J. Sue, "Mechanical properties of thermosets," in *Thermosets*. Elsevier, 2018, pp. 35–68.

[52] M. C. Boyce, D. M. Parks, and A. S. Argon, "Large inelastic deformation of glassy polymers. part i: rate dependent constitutive model," *Mechanics of Materials*, vol. 7, no. 1, pp. 15–33, 1988.

[53] G. Gray and W. R. Blumenthal, "Split-hopkinson pressure bar testing of soft materials." *Materials Park, OH: ASM International, 2000.*, pp. 488–496, 2000.

[54] P. Follansbee, P. Armstrong, J. Hockett, G. Dudder, and D. Erlich, "High strain rate compression testing," *ASM Handbook.*, vol. 8, pp. 190–207, 1985.

[55] P. Follansbee and C. Frantz, "Wave propagation in the split hopkinson pressure bar," *Journal of Engineering Materials and Technology*, vol. 105, no. 1, pp. 61–66, 1983.

[56] E. Davies and S. Hunter, "The dynamic compression testing of solids by the method of the split hopkinson pressure bar," *Journal of the Mechanics and Physics of Solids*, vol. 11, no. 3, pp. 155–179, 1963.

[57] D. L. Holt, "The modulus and yield stress of glassy poly (methyl methacrylate) at strain rates up to 103 inch/inch/second," *Journal of Applied Polymer Science*, vol. 12, no. 7, pp. 1653–1659, 1968.

[58] D. Rittel and A. Brill, "Dynamic flow and failure of confined polymethylmethacrylate," *Journal of the Mechanics and Physics of Solids*, vol. 56, no. 4, pp. 1401–1416, 2008.

[59] S. Abrate, "Criteria for yielding or failure of cellular materials," *Journal of Sandwich Structures and Materials*, vol. 10, no. 1, pp. 5–51, 2008.

[60] J. E. Field, S. M. Walley, W. G. Proud, H. T. Goldrein, and C. R. Siviour, *Review of experimental techniques for high rate deformation and shock studies*, 2004, vol. 30, no. 7.

[61] L. M. Barker and R. E. Hollenbach, "Shock-wave studies of pmma, fused silica, and sapphire," *Journal of Applied Physics*, vol. 41, no. 10, pp. 4208–4226, 1970.

[62] J. N. Johnson, J. J. Dick, and R. S. Hixson, "Transient impact response of three polymers," *Journal of Applied Physics*, vol. 84, no. 5, pp. 2520–2529, 1998.

[63] J. C. Millett and N. K. Bourne, "The shock induced equation of state of three simple polymers," *Journal of Physics D: Applied Physics*, vol. 37, no. 20, pp. 2901–2907, 2004.

[64] C. H. Neel, "Shock compression of a heterogeneous , porous polymer composite shock compression of a heterogeneous , porous," no. August, 2010.

[65] W. J. Carter and S. P. Marsh, "Hugoniot polymer data.pdf," pp. 1–25, 1995.

[66] C. R. Siviour and J. L. Jordan, "High strain rate mechanics of polymers: A review," *Journal of Dynamic Behavior of Materials*, vol. 2, no. 1, pp. 15–32, 2016.

[67] N. K. Bourne, "On the shock response of polymers to extreme loading," *Journal of Dynamic Behavior of Materials*, vol. 2, no. 1, pp. 33–42, 2016.

[68] P. J. Rae and D. M. Dattelbaum, "The properties of poly(tetrafluoroethylene) (ptfe) in compression," *Polymer*, vol. 45, no. 22, pp. 7615–7625, 2004.

[69] N. K. Bourne and J. C. Millett, "The high-rate response of an elastomer," *Proceedings of the Royal Society A: Mathematical, Physical and Engineering Sciences*, vol. 459, no. 2031, pp. 567–576, 2003.

[70] S. Vol, G. Britain, and C. Division, "Pressure-shear waves in 6061-t6 aluminum," vol. 33, no. 3, pp. 263–284, 1985.

[71] S. E. Grunschel, "Pressure-shear plate impact experiments on high-purity aluminum at temperatures approaching melt," no. May, 2009.

[72] W. D. Reinhart, I. Thornhill, Tom Finley, T. J. Vogler, and C. S. Alexander, "Pressure-shear experiments on granular materials." *Sandia National Laboratories Report*, vol. SAND2011-6, no. October, 2011.

[73] W. Tong, R. J. Clifton, and S. Huang, "Pressure-shear impact investigation of strain rate history effects in oxygen-free high-conductivity copper," *Journal of the Mechanics and Physics of Solids*, vol. 40, no. 6, pp. 1251–1294, 1992.

[74] J. W. Lajeunesse, "Dynamic behavior of granular earth materials subjected to pressure-shear loading," 2018.

[75] K. T. Ramesh and R. J. Clifton, "A pressure-shear plate impact experiment for studying the rheology of lubricants at high pressures and high shearing rates," *Journal of Tribology*, vol. 109, no. 2, pp. 215–222, 1987.

[76] ——, "Finite deformation analysis of pressure-shear plate impact experiments on an elastohydrodynamic lubricant," vol. 59, no. 92, 2015.

[77] R. Feng and K. Ramesh, "On the compressibility of elastohydrodynamic lubricants," *Journal of Tribology*, vol. 115, no. 3, 1993.

[78] Y. Gupta, "Shear measurements in shock-loaded solids," *Applied Physics Letters*, vol. 29, no. 11, pp. 694–697, 1976.

[79] ——, "High strain-rate shear deformation of a polyurethane elastomer subjected to impact loading," *Polymer Engineering & Science*, vol. 24, no. 11, pp. 851–861, 1984.

[80] F. Yuan, N. S. Liou, and V. Prakash, "High-speed frictional slip at metal-on-metal interfaces," *International Journal of Plasticity*, vol. 25, no. 4, pp. 612–634, 2009.

[81] N. K. Myshkin, M. I. Petrokovets, and A. V. Kovalev, "Tribology of polymers: Adhesion, friction, wear, and mass-transfer," *Tribology International*, vol. 38, no. 11-12 SPEC. ISS., pp. 910–921, 2005.

[82] D. E. Packham, "Surface energy, surface topography and adhesion," *International Journal of Adhesion and Adhesives*, vol. 23, no. 6, pp. 437–448, 2003.

[83] P. L. Menezes, Kishore, S. V. Kailas, and M. R. Lovell, "Friction and transfer layer formation in polymer-steel tribo-system: Role of surface texture and roughness parameters," *Wear*, vol. 271, no. 9-10, pp. 2213–2221, 2011.

[84] P. Molitor, V. Barron, and T. Young, "Surface treatment of titanium for adhesive bonding to polymer composites: A review," *International Journal of Adhesion and Adhesives*, vol. 21, no. 2, pp. 129–136, 2001.

[85] M. M. Koura and M. A. Omar, "The effect of surface parameters on friction," *Wear*, vol. 73, no. 2, pp. 235–246, 1981.

[86] B. J. Briscoe and D. Tabor, "Shear properties of thin polymeric films," *The Journal of Adhesion*, vol. 9, no. 2, pp. 145–155, 1978.

[87] K. V. Shooter and D. Tabor, "The frictional properties of plastics," *Proceedings of the Physical Society. Section B*, vol. 65, no. 9, pp. 661–671, 1952.

[88] D. Tabor, "Friction—the present state of our understanding," *Journal of Tribology*, vol. 103, no. 2, p. 169, 1981.

[89] R. C. Bowers and W. A. Zisman, "Pressure effects on the friction coefficient of thin-film solid lubricants," *Journal of Applied Physics*, vol. 39, no. 12, pp. 5385–5395, 1968.

[90] L. C. Towle, "Shear-strength and friction measurement on thin layers under high pressure," *Journal of Applied Physics*, vol. 42, no. 6, pp. 2368–2376, 1971.

[91] J. R. Foley, J. L. Jordan, E. Afb, C. R. Siviour, C. B. Ohe, M. April, E. Air, and F. Base, "Constitutive modeling of epoxy using the mulliken-boyce model

for glassy polymers munitions directorate university of cambridge this paper was presented at the mechanics of time-dependent materials u . s . government is joint owner of the work . when publ," *Engineering*, 2008.

[92] J. Yi, M. C. Boyce, G. F. Lee, and E. Balizer, "Large deformation rate-dependent stress-strain behavior of polyurea and polyurethanes," *Polymer*, vol. 47, no. 1, pp. 319–329, 2006.

[93] S. G. Bardenhagen, M. G. Stout, and G. T. Gray, "Three-dimensional, finite deformation, viscoplastic constitutive models for polymeric materials," *Mechanics of Materials*, vol. 25, no. 4, pp. 235–253, 1997.

[94] L. A. Merzhievskii and M. S. Voronin, "Modeling of shock-wave deformation of polymethyl metacrylate," *Combustion, Explosion, and Shock Waves*, vol. 48, no. 2, pp. 226–235, 2012.

[95] P. W. Cooper, *Explosives engineering*. John Wiley & Sons, 2018.

[96] M. A. Meyers, *Dynamic behavior of materials*. John wiley & sons, 1994.

[97] M. L. Wilkins, *Computer simulation of dynamic phenomena*. Springer Science & Business Media, 2013.

[98] K. Brugger, "Generalized grüneisen parameters in the anisotropic debye model," *Physical Review*, vol. 137, no. 6A, p. A1826, 1965.

[99] L. Davison, *Fundamentals of shock wave propagation in solids*. Springer Science & Business Media, 2008.

[100] J. W. Forbes, *Shock wave compression of condensed matter: a primer*. Springer Science & Business Media, 2013.

[101] D. Bancroft, E. L. Peterson, and S. Minshall, "Polymorphism of iron at high pressure," *Journal of Applied Physics*, vol. 27, no. 3, pp. 291–298, 1956.

[102] H. Kolsky, *Stress waves in solids*. Courier Corporation, 1963, vol. 1098.

[103] K. J. Frutschy and R. J. Clifton, "High-temperature pressure-shear plate impact experiments using pure tungsten carbide impactors," *Experimental Mechanics*, vol. 38, no. 2, pp. 116–125, 1998.

[104] C. R. Johnson, P. A. Sable, J. W. Lajeunesse, A. Dawson, A. Hatzenbihler, and J. P. Borg, "Photon doppler velocimetry measurements of transverse surface velocities," *AIP Conference Proceedings*, vol. 1979, 2018.

[105] K. W. Schuler, J. W. Nunziato, and E. K. Walsh, "Recent results in nonlinear viscoelastic wave propagation," *International Journal of Solids and Structures*, vol. 9, no. 10, pp. 1237–1281, 1973.

[106] F. J. Zerilli and R. W. Armstrong, "Dislocation-mechanics-based constitutive relations for material dynamics calculations," *Journal of Applied Physics*, vol. 61, no. 5, pp. 1816–1825, 1987.

[107] Y. Zhang, J. C. Outeiro, and T. Mabrouki, "On the selection of johnson-cook constitutive model parameters for ti-6al-4v using three types of numerical models of orthogonal cutting," *Procedia CIRP*, vol. 31, pp. 112–117, 2015.

[108] ASTM, "American society for testing and materials- astm. d143-94: Standard methods of testing small clear samples of timber," *American Society for Testing and Materials - ASTM. Annual Book of ASTM*, vol. 94, no. Reapproved, p. 31, 1994.

[109] S. S. Sarva, S. Deschanel, M. C. Boyce, and W. Chen, "Stress-strain behavior of a polyurea and a polyurethane from low to high strain rates," *Polymer*, vol. 48, no. 8, pp. 2208–2213, 2007.

[110] C. Prisacariu, C. P. Buckley, and A. A. Caraculacu, "Mechanical response of dibenzyl-based polyurethanes with diol chain extension," *Polymer*, vol. 46, no. 11, pp. 3884–3894, 2005.

[111] S. P. Marsh, *LASL shock Hugoniot data*. Univ of California Press, 1980, vol. 5.

[112] G. J. Appleby-Thomas, P. J. Hazell, C. Stennett, G. Cooper, and R. Cleave, "The dynamic behaviour of a modified polyurethane resin," *DYMAT 2009 - 9th International Conferences on the Mechanical and Physical Behaviour of Materials under Dynamic Loading*, vol. 2, pp. 1081–1087, 2009.

[113] D. Munson and R. May, "Dynamically determined high-pressure compressibilities of three epoxy resin systems," *Journal of Applied Physics*, vol. 43, no. 3, pp. 962–971, 1972.

[114] D. C. Wood, P. J. Hazell, G. J. Appleby-Thomas, and N. R. Barnes, "Shock behaviour of a phenolic resin," *Journal of materials science*, vol. 46, no. 18, pp. 5991–5999, 2011.

[115] R. W. Klopp and R. J. Clifton, "Analysis of tilt in the high-strain-rate pressure-shear plate impact experiment," *Journal of Applied Physics*, vol. 67, no. 11, pp. 7171–7173, 1990.

[116] T. J. Vogler, J. P. Borg, and D. E. Grady, "On the scaling of steady structured waves in heterogeneous materials," *Journal of Applied Physics*, vol. 112, no. 12, 2012.

[117] R. C. Bowers, "Coefficient of friction of high polymers as a function of pressure," *Journal of Applied Physics*, vol. 42, no. 12, pp. 4961–4970, 1971.

[118] D. Crawford, A. Brundage, E. Harstad, K. Ruggirello, R. Schmitt, S. Schumacher, and J. Simmons, "Cth user's manual and input instructions," *Version*, vol. 8, pp. 115–118, 2007.

[119] L. R. Rabiner and B. Gold, "Theory and application of digital signal processing," *Englewood Cliffs, NJ, Prentice-Hall, Inc., 1975. 777 p.*, 1975.

[120] D. Dolan, "Accuracy and precision in photonic doppler velocimetry," *Review of Scientific Instruments*, vol. 81, no. 5, p. 053905, 2010.

APPENDIX A

OBLIQUE IMPACT TARGET DESIGN

The design of oblique impact experiments, specifically the CPPSPI configuration, centers around three key constraints; keeping the anvil/impactor materials elastic, ensuring stress wave separation, and minimizing stress release behaviors. Considering the first constraint alone, for an anvil to remain elastic during impact typically its yield strength must not be exceeding throughout loading. Most metals following a yield criteria sufficiently predicted by the von-Mises yield conditions. This is presented in eq. A.1, where yield occurs when loading conditions exceed the anvil shear strength.

$$\tau^2{}_y \leq [(\frac{1-2\nu}{1-\nu})^2(\frac{\rho C_L}{2\sqrt{3}})^2 cos^2\theta + (\frac{\rho C_S}{2})^2 sin^2\theta] V^2{}_p \tag{A.1}$$

As shown, τ_y is shear strength, ν is the Poisson's ratio, C_L and C_S are elastic sound speeds, ρ is initial density, θ is oblique angle of impact, and V_p is impact velocity. All properties, aside from impact conditions, are with respect to the anvil material in question.

Using this formulation, the point at which yielding occurs may be found for any given combination of impact velocity and angle. Figure A-1 plots the threshold values at which point given impact conditions results in anvil yield. Specifically presented is the threshold values for the 7075-T6 aluminum anvils used in this work. As an example, for a given impact angle of 20 deg, impact should not exceed approximately 113 m/s otherwise the anvil materials may yield.

With this information, typically comparing multiple materials, an anvil material is selected and impact conditions are given a limit in both speed and angle. The next design problem becomes stress wave separation/arrival at the polymer

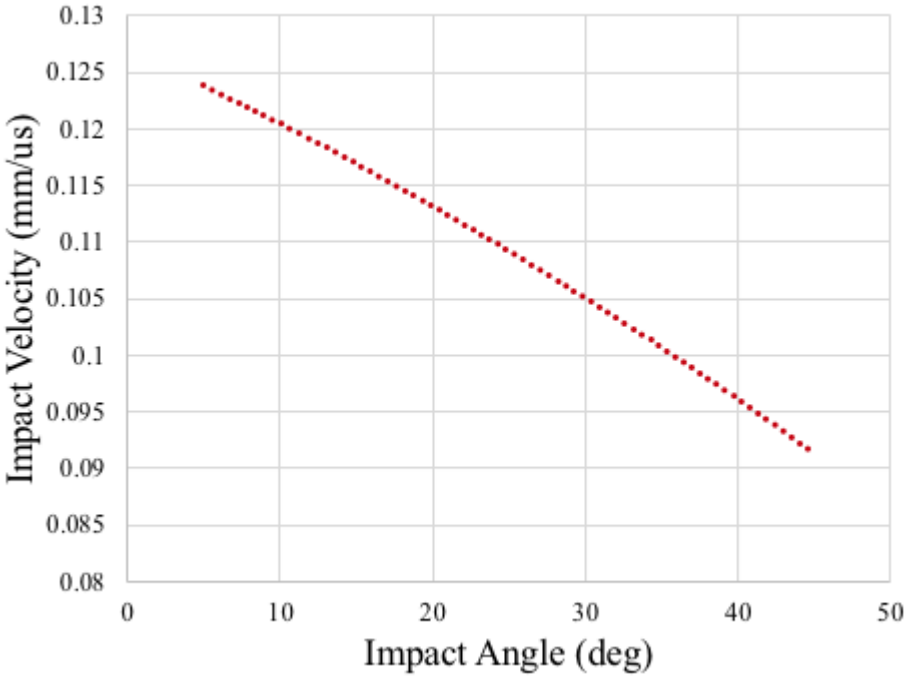

Fig. A-1. Threshold values constraining the various impact velocities and angles acceptable when using 7075-T6 aluminum as an anvil material in oblique impact experiments.

specimen. In CPPSPI experiments, the intention is to subject the specimen (confined between two anvils) to pressure *then* shear stress loading. To facilitate this, the pressure (normal stress) wave must arrive at the specimen, through the front anvil, and ring up between anvils to pressure equilibrium - prior to the shear wave arriving. Mathematically this can be stated as eq. A.2,

$$t_s > t_L + t_{reverb} \tag{A.2}$$

where t_L and t_s are the wave transit times for the elastic longitudinal and shear stress waves to propagate through the rear anvil, and t_{reverb} is the reverberation time necessary for the sample to come to pressure equilibrium with the confining anvils. The variable t_{reverb} is dependent on specimen thickness, stress impedance,

and the impedance of the surrounding anvils and is approximated based on simulations or analytic impedance matching.

Transit times may be formulated in terms of front anvil thickness and elastic sound speeds stated generally as $t = \frac{X}{C}$ where X is the transit distance and C is wave speed. Implementing the corresponding elastic sound speeds and anvil thickness eq. A.2 may be reformulated and solved for the necessary anvil thickness to provide such conditions, eq. A.3, where x_{FA} is the minimum front anvil thickness, and C_L / C_S are the longitudinal and transverse elastic sound speeds.

$$x_{FA} = t_{reverb}\frac{C_L C_S}{C_L - C_S} \tag{A.3}$$

Following these procedures, experimentally both anvil elasticity is maintained and the specimen of interest should be subjected to the desired pressure-then-shear conditions. The final phenomena to consider is then limited to only release wave behavior. These interrupt (releasing in stress) the loading conditions induced and limit the time frame during which a stress wave experiment may be valid. They originate from two sources, the edges of the target diameter (within which lies only the target-of-interest) or free surfaces at either the target rear or impactor back-surface.

Edge release waves form because of impedance mismatches between the target-of-interest and the material it is radially bound within (such as mounting fixtures). As desired stress waves propagate into the target, these release waves have an angled propagation both down toward the target center and into the target thickness. A reasonable rule of thumb for this angle is 45-degrees **??**. For every 1 mm desired waves have traveled into the target thickness, the release waves have traveled 2 mm radially inward toward the target center. With this in mind, targets

must be kept relatively thin so that waves measured (traditionally near the target center) are undisturbed.

Better detailed by Meyers [96], when stress waves produced by experiment propagate into a material of higher impedance they increase in stress magnitude while interaction with a lower impedance results in a reduction of stress. It is unsurprisingly that when waves meets free surface, the surface is allowed to expand a release stress to a zero state (incrementally). The stress release then propagates into the material, changing the experiment. Figure A-2 schematically shows these release waves in the case of a uniaxial plane-strain impact experiment (which is more straightforward to visualize).

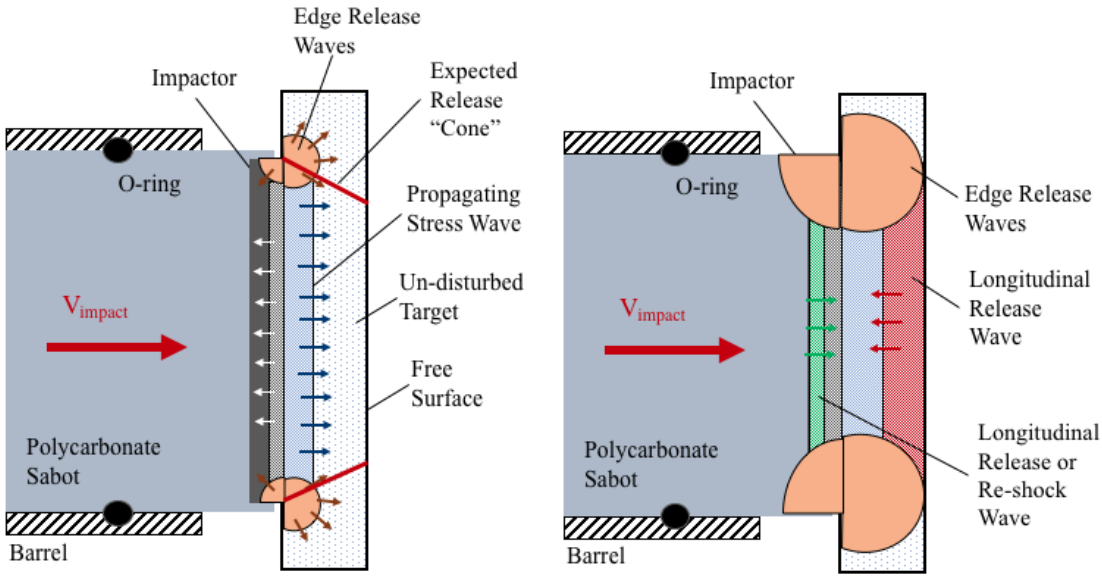

Fig. A-2. Wave dynamics within a unaxial plane-strain impact experiment, including release wave mechanisms. This demonstrates the potential design constraints enforced by release behavior such as maximizing the target diameter to thickness ratio.

With release phenomena now detailed, it can be seen upon inspection of Figure A-2 that it is preferable to have a thin target thickness with a large diameter. Typically, diameter is limited by the gun bore being used and so thickness is the usually the only feature which may be varied.

Returning to the consideration of CPPSPI experiments, recall that the front anvil thickness is set, as is the specimen thickness (from reverberation time approximations). This leaves only the rear anvil thickness to vary, which qualitatively must be thin enough remove edge release concerns, but thick enough such that the polymer specimen is not released too early via longitudinal interactions. With elasticity and wave separation already considered, all three constraints may be implemented together via the use of X-t diagrams used to track wave propagation. Figure A-3 shows a CPPSPI schematic alongside an X-t diagram which was used as the final step in CPPSPI target design. Dimensions are consistent with those implemented in experiment.

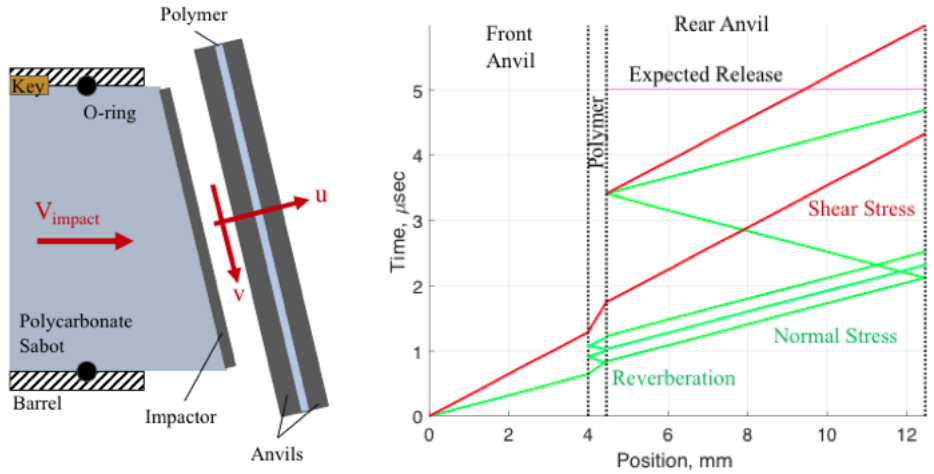

Fig. A-3. A schematic diagram and X-t plot demonstrating the wave propagation expected within a constant-pressure pressure-shear plate impact experiment. Overall thickness is chosen such that edge release is not a concern over the duration of the experiment, and expected longitudinal release time is shown.

Final target design geometries were modeled in *SolidWorks* and then manufactured in house at Marquette University. Figure A-4 and A-5 show CAD rendering of the target both free and within the gimbal setup, alongside manufactured components.

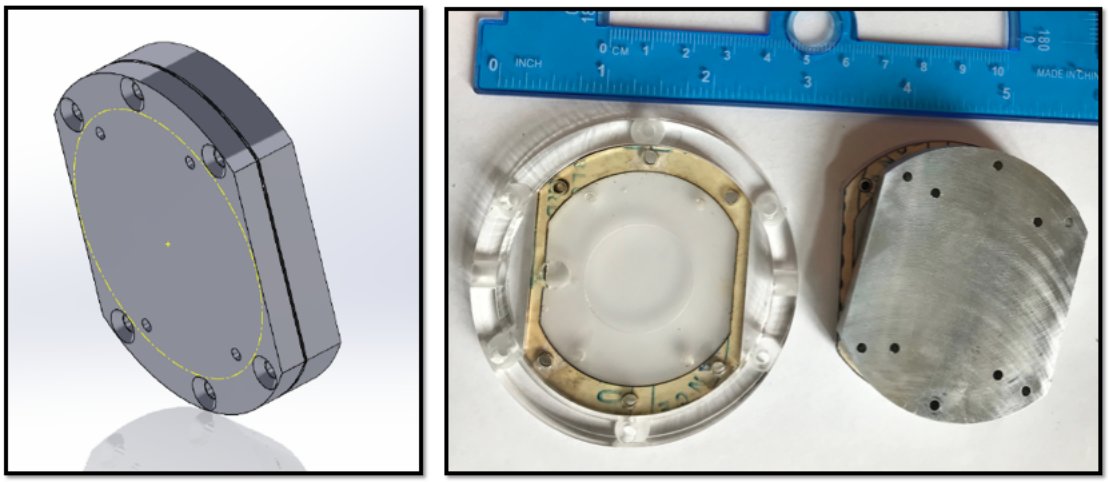

Fig. A-4. CPPSPI experiment target rendered in CAD alongside a final manufactured part.

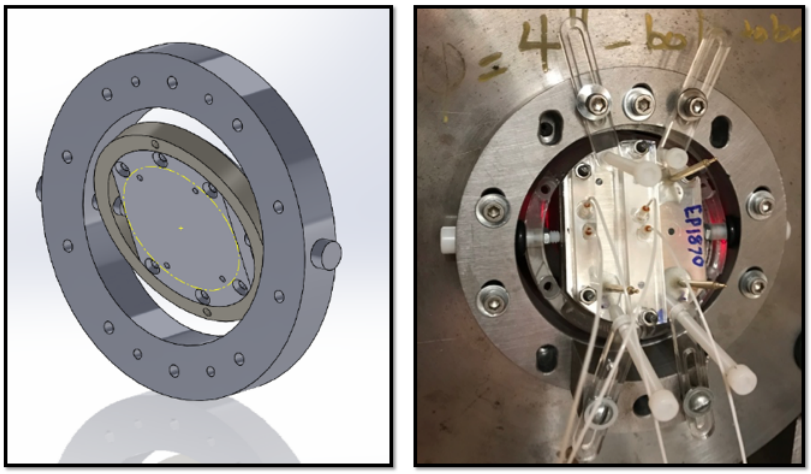

Fig. A-5. Final experiment assembly rendered in CAD compared to a final experiment mounted and ready for impact in a CPPSPI experiment.

APPENDIX B

ALIGNMENT PROCEDURES FOR OBLIQUE IMPACT

Alignment is particularly critical in the context of oblique impact experiments given the implications of angled wave propagation discussed in Ch. 4 as well the need to minimize uncertainty and ensure combined stress loading conditions are reproducible. The procedure for alignment at the Marquette University Shock Physics Laboratory (MUSPL) is provided herein, and are ordered in terms of barrel/target concentricty, mount-plate/barrel orthogonality, projectile skew, and finally angle of impact obliquity.

First, it was required the barrel center be concentric with the target mount-plate. A barrel plug was set into the muzzle, with a center-post protruding toward the plane of the would-be target. This is fed through a mounted faux-target with an inlaid through hole matching the diameter of the post. With no interference between the post and through hole, the target mount is considered concentric to the barrel. A depth gauge was then mounted to the same post and the relative position of the mount plate to the barrel is measured at 12 points spaced around the periphery. Twice the standard deviation of this value was taken as the max deviation and an angle is calculated with respect to the diameter of measured points. This angle is a conservative metric for orthogonality of the shotline with respect to the target plane, with 0 mrad being the ideal. Values less than 1 mrad were typical and deemed acceptable.

The previous steps, in concept, are standard to any gas gun experiment. In contrast the latter two, checking skew and obliquity, are unique to oblique shots. Defined as angular deviation with respect to the shot direction, skew is checked by placing the to-be projectile in the muzzle with the key fixing its orientation. A level is then set on a flat milled onto the impactor, and the barrel is rotated until leveled,

further checked by an angle-finder to be zero (within an uncertainty of 0.5-deg). Lastly, the fully assembled target is mounted, set within an outer ring serving as a gimbal. The projectile is then pushed down the barrel, affixed to a rope for later retrieval, where it was mechanical mated to the target. Small (0.084 inch) through were placed around the target and impact surfaces were ensured flush through depth measurements taken at the back surface. The oblique angle was then fixed with set screws mounted to the outer ring. Portions of the alignment process are shown in Figure B-1.

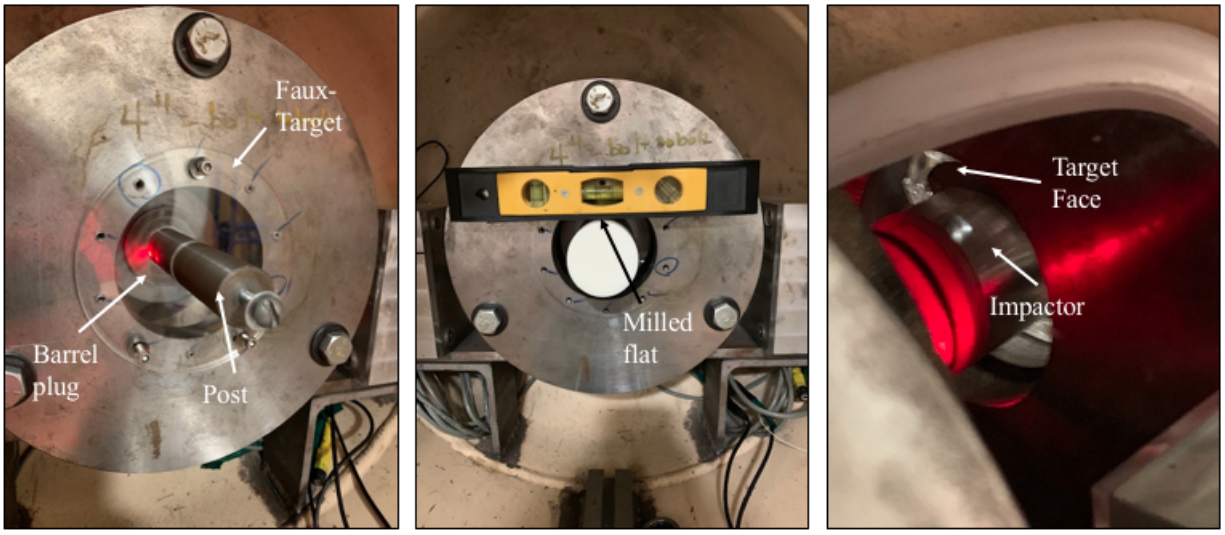

Fig. B-1. Images demonstrating the alignment steps needed to minimize tilt for oblique impact experiments, left to right including the concentricity check, skew alignment, and mechanical mating to match the angle of obliquity.

After pulling the projectile out of the barrel, alignment was considered achieved. However, impact tilt to some degree is inevitable, and is only minimized through the aforementioned precautions. This is measured through pins embedded with piezoelectric crystals on the tips, inset on the periphery of the target (PZT pins). Shown back in Figure 6-2, impact produces a measured voltage spike in each

of these, and together with spatial location and surface protrusion measurements enables the calculation of tilt. Measurements between 1 and 15 mrad have been observed and are reported throughout.

APPENDIX C

PRINCIPLES OF PHOTON DOPPLER VELOCIMETRY

The primary diagnostic used throughout all gas gun experiments described in this work is Photon Doppler Velocimetry (PDV), as such an overview of foundational principles are provided here. Developed in 2006 by Strand and colleagues [12], PDV is compact fiber-laser based velocimeter system that functions similarly to a Michelson interferometer. As the name implies, it relies on the Doppler shift of laser light frequency to quantify a surface velocity. Figure C-1 presents a schematic created by Ohio State Impulse Manufacturing laboratory which excellently conveys the relevant physics [11].

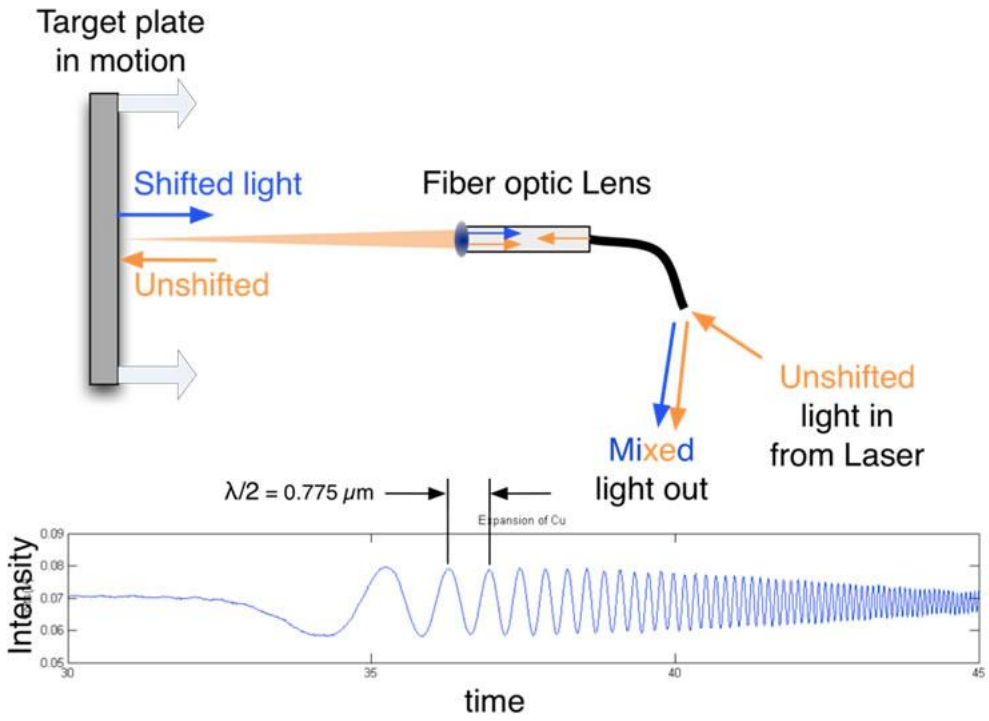

Fig. C-1. PDV emits light onto a target surface of interest and collects the reflection. When in motion, the frequency of emitted light is Doppler shifted such that the reflected such that is possesses a greater or lower wavelength. From this velocity information may quantified. Image from [11]

For the most basic of configurations, 1550 nm light is emitted from a laser source into a fiber optic cable. This leads to a three port circulator, where light entering from port-1 is emitted from port-2 through a collimating probe. The collimator is aligned to some surface of interest such that the 1550 nm light is projected toward the surface and is immediately reflected back into the collimator. When the surface is in motion the reflected light is Doppler-shifted in frequency. Reflected light then propagates from the collimator back into port-2 of the circulator and out port-3. The signal is then coupled with unshifted light, converted to voltage via optical detector, and measured using an oscilloscope. This combination of shifted with unshifted light produces a beat frequency directly related to the surface velocity responsible for the Doppler shift, via eq. C.1,

$$f_b = \frac{2v}{\lambda_T} \tag{C.1}$$

where f_b is the measured signal beat frequency, v is the surface velocity, and λ_T is the wavelength of unshifted light. The measurement of the beat frequency is key to the operation of PDV. A 1550 nm wavelength corresponds to a signal frequency of approximately $1.9x10^5 GHz$, which far exceeds the bandwidth capabilities of any modern measurement system. The beat frequency, however, is on the order of 100 MHz and is readily resolvable. Resulting data comes in the form of fringes, oscillating waveforms whose frequencies correspond to the beat of superimposed signals. Short-time discrete Fourier transforms (STFT) may then be applied to the signal incrementally over time, and a time dependent velocity profile may be calculated using eq. C.1.

The specific wavelength is due to the wide availability of fiber optic components which operate at 1550 nm, driven by the telecommunications industry. This availability makes PDV a compact (non open-beam laser) and relatively inexpen-

sive solution to measurement high speed velocity behavior. More so, it is known be highly accurate with nanosecond time resolution and velocity uncertainties as low as one percent [120].

A schematic of the MUSPL PDV system is presented in FigureC-2. As with many systems, the Marquette system has multiple channels (qty 4) operating in parallel so multiple measurements may be made simultaneously. This figure was published by Johnson at colleagues from Marquette **??**.

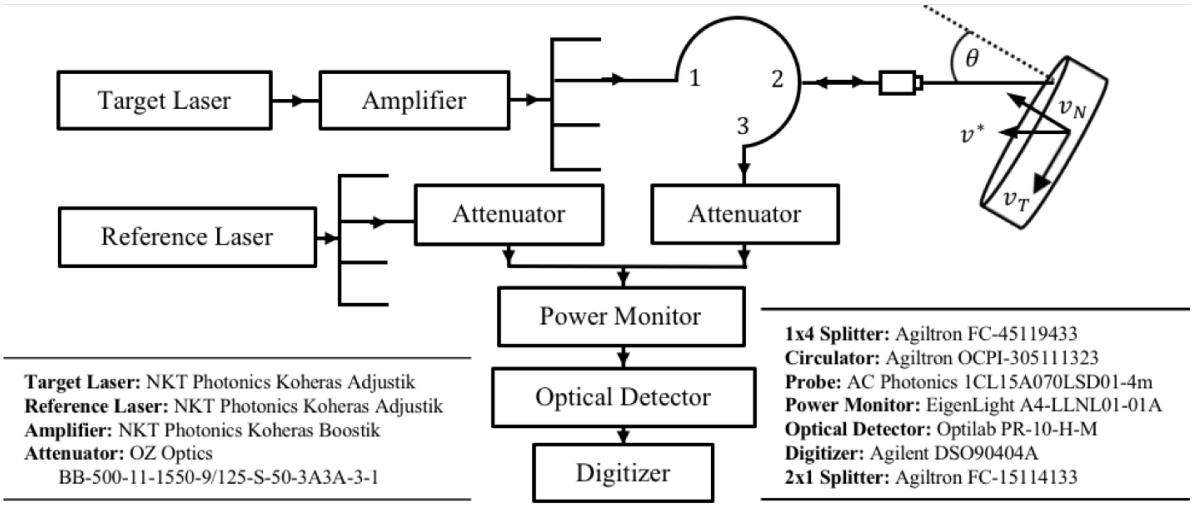

Fig. C-2. Schematic diagram of the Marquette University Shock Physics Laboratory 4-channel heterodyne photon Doppler velocimeter, including a component list.

The most noteworthy discrepancy between the presented figure and the discussed operation is the inclusion of a reference laser. As mentioned, the collected frequency-shifted light is coupled with unshifted light to provide a measurable beat. In a traditional, or homodyne, configuration this unshifted light originates from the same laser source as what was reflected of the target. Alternatively, for a heterodynae configuration, a separate ”reference” laser source is utilized. This laser may be independently tuned in frequency which allows the user to control

the the location of beat in frequency space, termed upshifting. This changes the math slightly, giving the form, eq. C.2

$$f_s - (f_R - f_T) = \frac{2v}{\lambda_T} \tag{C.2}$$

where f_s is the collected Doppler-shifted light, f_R is the reference laser frequency, and f_T is the "target" laser frequency corresponding to the unshifted light emitted at the moving target. Upshifting is particularly beneficial when attempting to observe low velocities ($\leq$ 100 m/s). Upshifting artificially increases frequency, forcing more fringes into a discrete time window and improving resolution. This is perhaps more easily conveyed visually attempted in Figure C-3.

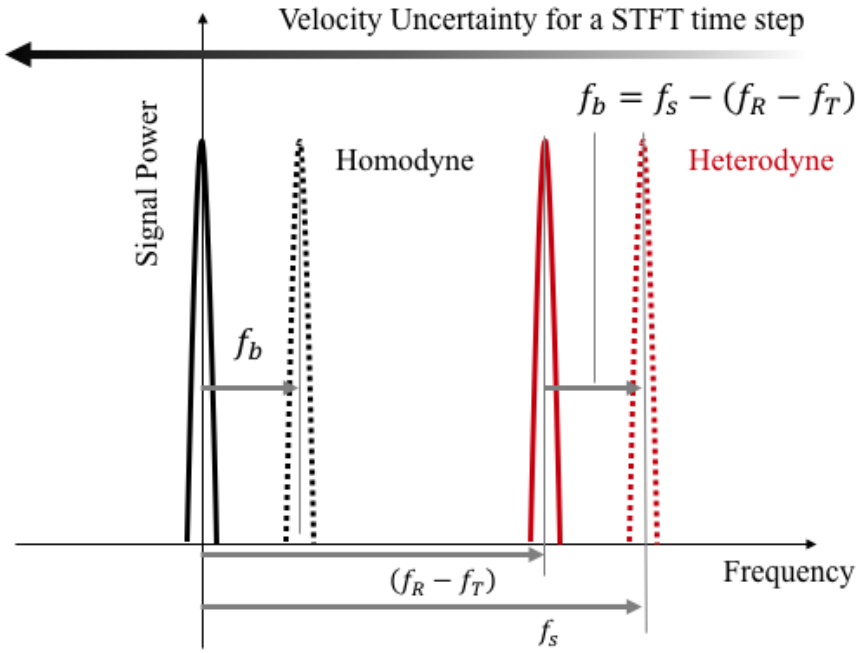

Fig. C-3. A comparison of homodyne and heterodyne PDV configurations with respect to how they effect the signal in frequency space.

As mentioned, the end result within an experiment using PDV is a waveform consisting of oscillating fringes containing useful frequency information. This

is consistent regardless of whether the configuration is heterodyne or homodyne. With only this brief background, it is now possible to take any of these waveforms and (via STFT) convert them to the velocity profiles similar to those seen throughout this work. This additionally provides a springboard for the transverse measurement techniques discussed throughout experimental results. As a summarized takeaway, Figure C-4 shows a general flow of data processing to be followed, which incorporates some of Strand's original traces used to publicize PDV [12].

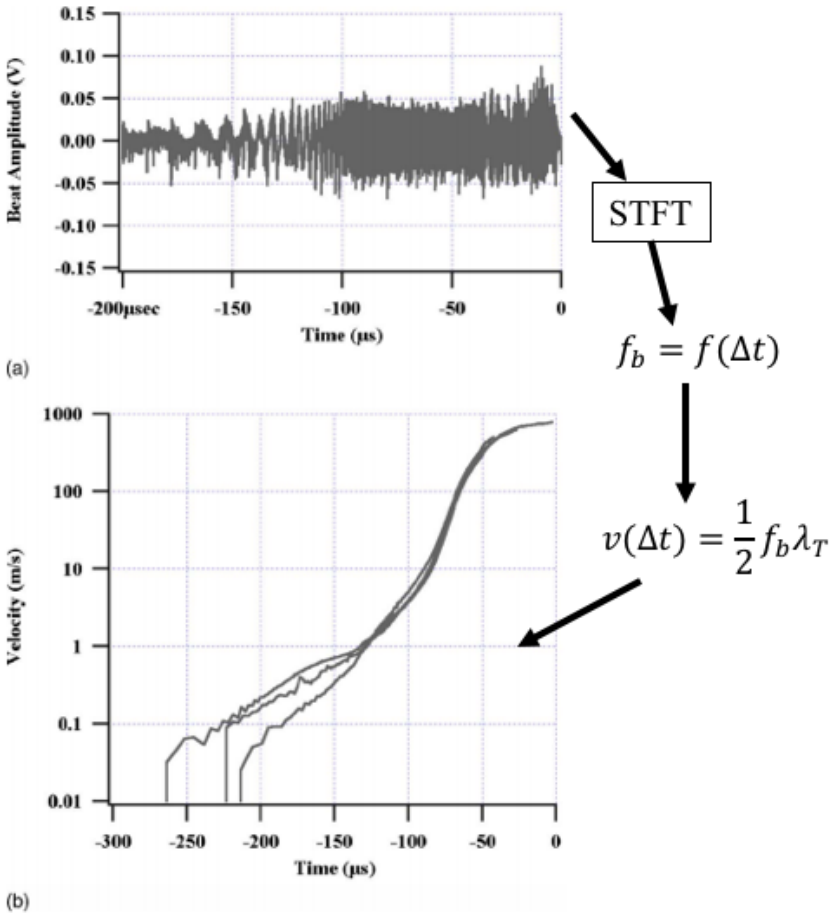

Fig. C-4. A flow chart for processing PDV data with original data from Strand [12] used as example input and output.